Thesis for a Ph.D. Degree

Microphysical properties of Arctic mixed-phase clouds and their influence on radiation balance: Observation vs. modeling

관측과 모델 비교를 통한 북극 혼합 구름의
미세물리 특성 및 복사효과 연구

August 2023

School of Earth and Environmental Sciences
Graduate School
Seoul National University

Jihyun Nam

Microphysical properties of Arctic mixed-phase clouds and their influence on radiation balance: Observation vs. modeling

By
Jihyun Nam

A Dissertation Submitted to the Faculty of the Graduate School of the Seoul National University in Partial Fulfillment of the Requirement for the Degree of Doctor of Philosophy

Degree Awarded:
August 2023

Advisory committee:

Professor Chang-Hoi Ho

Professor Sang-Woo Kim

Professor Baek-Min Kim

Professor Jin-Ho Yoon

Professor Kyo-Sun S. Lim

이학박사 학위논문

관측과 모델 비교를 통한 북극 혼합 구름의 미세물리 특성 및 복사효과 연구

Microphysical properties of Arctic mixed-phase clouds and their influence on radiation balance: Observation vs. modeling

2023년 8월

서울대학교 대학원

지구환경과학부

남 지 현

Microphysical properties of Arctic mixed-phase clouds and their influence on radiation balance: Observation vs. modeling

지도 교수 김 상 우

이 논문을 이학박사 학위논문으로 제출함
2023 년 5 월

서울대학교 대학원
지구환경과학부
남 지 현

남지현의 이학박사 학위논문을 인준함
2023 년 7 월

위 원 장 _____허 창 회_____ (인)

부위원장 _____김 상 우_____ (인)

위   원 _____김 백 민_____ (인)

위   원 _____윤 진 호_____ (인)

위   원 _____임 교 선_____ (인)

Abstract

Clouds have a major impact on the Earth's radiative budget and climate change, yet little microphysical data has been collected on clouds in the polar regions. This lack of microphysics data is related to the challenges of deploying and operating instruments in some of the world's most challenging and remote atmospheric environments. This thesis investigates the macro- and microphysical properties of clouds based on observations over Ny-Ålesund, Svalbard, in order to better understand the role of clouds in the Arctic. The total cloud occurrence was found to be ~77.6% from February 2017 to February 2023. The most predominant cloud type is multilayer clouds with a frequency of occurrence of 39.1%, and single-layer clouds with ~37.2%. The total occurrences of single-layer ice, liquid, and mixed-phase clouds are 19%, 4.4%, and 14.9%, respectively. In addition, surface measurements of upward and downward shortwave and longwave radiation from the Baseline Surface Radiation Network (BSRN) at Ny-Ålesund station were examined. Relatively lower values of upward and downward longwave fluxes for ice and mixed-phase clouds were highly correlated with cloud top temperature by phase.

The database of cloud properties and the classification method obtained in this work are used to evaluate weather prediction models. We evaluated the microphysical properties of Arctic low-level clouds simulated by four cloud microphysics parameterization schemes (Morrison, WDM6, NSSL, and P3) implemented in the Polar-optimized Weather Research and Forecasting (PWRF) model. The evaluation is based on a comparison with data from the Arctic Cloud Observations Using Airborne Measurements during the Polar Day (ACLOUD) experiment, which took place near Svalbard in May-June 2017. A significant number of clouds were observed during the campaign, mainly due to adiabatic motions and sensible/latent heat fluxes that caused air masses to warm (by 4°C) as they were transported over the sea ice and ocean transition zone. The Morrison and WDM6 schemes performed best overall, with frequency bias (FB) values close to 1 (1.07, 1.13) and high log-odds ratios (0.50, 0.48) in predicting cloud occurrence, indicating good agreement with observed cloud occurrence. On the other hand, the NSSL and P3 schemes showed a high FB value (1.30, 1.56) with a low log-odds ratio (0.17, 0.16), indicating a high overestimation of cloud occurrence.

Conversely, the WDM6 scheme produced higher ice-mixing ratios than the Morrison and NSSL schemes, while the latter two tended to produce more snow and graupel. However, all schemes generally underestimated both liquid and ice water content. Longwave downward (LWD) flux depends on atmospheric temperature and humidity, which are simulated differently by each cloud microphysics scheme. The model underestimated LWD flux is highly correlated with the LWC bias of each scheme.

This study highlights the critical need for observational development of cloud parameterization in the Arctic to better estimate the impact of clouds on the Arctic climate under conditions of rapid Arctic warming.

Keywords: Arctic cloud, Mixed-phase cloud, ACLOUD, Cloudnet, PWRF, Cloud microphysics scheme

Student Number: 2015-30984

Table of Contents

List of Figures

List of Tables

Chapter 1. Introduction

1.1 Background and motivation

The surface temperature and the extent of sea ice and snow melt are significantly influenced by the frequent occurrence of Arctic clouds at low altitudes. This is mainly due to modulation of downward longwave and shortwave radiation. (Urrego-Blanco et al., 2019; Yeo et al., 2022). In particular, the liquid water properties of clouds are relevant to the surface energy budget in the Arctic, as the downward longwave radiation and the shortwave reflectivity of cloud tops are highly sensitive to the small effective radius of cloud droplets and the cloud liquid water path (Twomey, 1974; Garrett et al., 2002). Quantifying the contribution of clouds to observed Arctic amplification and cloud feedback mechanisms is challenging, as clouds have a significant impact on the global radiative budget and climate (Goosse et al., 2018). Assessing cloud-related changes in the surface energy budget therefore requires modelling or observational estimates of Arctic cloud properties such as cloud optical thickness and cloud fraction (CF) (Kay et al., 2016).

Many studies have investigated Arctic cloud properties and associated radiative effects using global and regional-scale simulation models, focusing mainly on cloud-radiative feedbacks between boundary layer clouds, near-surface temperature, and sea ice melt (Serreze and

Barry, 2011; Morrison et al., 2015; Lelli et al., 2022). However, accurate simulations of Arctic cloud properties remain a challenge due to the complexity of cloud microphysical processes (**Figure 1**) (Vavrus et al., 2008; Klein et al., 2009; Barton et al., 2012; de Boer et al., 2012; Wesslen et al., 2014; Sotriopoulou et al., 2021; Shaw et al., 2022). The parameterization of cloud microphysical properties and model validation face challenges due to the limited in situ and remote sensing observations of Arctic cloud properties (Kay et al., 2016; Boisvert et al., 2018).

While different cloud microphysics schemes describing the formation, growth, and deposition of hydrometeors have been developed to represent clouds and their radiative effects (Seiki et al., 2022; Zhou et al., 2022), the differences in the treatment of their microphysical processes lead to uncertainties in cloud-radiative interactions (Voigt et al., 2019; Sedlar et al., 2020). Previous studies have shown that different cloud microphysics schemes used in climate models lead to significant differences in the simulated geometric (e.g., cloud amount and height) and microphysical (e.g., cloud phases, droplet size, and hydrometeor shapes) properties of clouds over the mid-latitude and tropical regions (English et al., 2014; Park et al., 2014; Silber et al., 2018).

Cloud microphysical parameterizations have typically been developed for tropical and mid-latitude clouds, but have not been extensively validated for Arctic clouds due to a lack of field observations (Nguyen et al., 2022). Although cloud microphysics schemes have been evaluated in several field experiments over the Arctic (e.g., Surface Heat Budget of the Arctic Ocean (SHEBA) campaign, Intrieri et al., 2002; Arctic Summer Cloud-Ocean Study (ASCOS) campaign, Tjernstrom et al., 2014; and Atmospheric Radiation Measurement West Antarctic Radiation Experiment (AWARE), Lubin et al., 2020), simulations of the microphysical properties of Arctic clouds have generally performed poorly, showing significant discrepancies with those obtained from ground-based and airborne observations (Walsh et al., 2002; Kretzschmar et al., 2020). Several recent studies have also investigated the sensitivity of cloud microphysics schemes in regional-scale Weather Research and Forecasting (WRF) model predictions over the polar regions (Hines and Bromwich, 2008; Wilson et al., 2012; Seo and Yang, 2013; Bromwich et al., 2016; Hines and Bromwich, 2017; Kim et al., 2022). However, the differences in model performance using different cloud microphysics schemes over the Arctic region, particularly with respect to Arctic summer clouds, have not been investigated. Version 4.1.1 of WRF, which is included in Polar-optimized WRF (PWRF), has not

3

been optimized for the Arctic, although it has been optimized for the Antarctic environment (Hines et al., 2021). Therefore, the performance of the cloud microphysics schemes included in version 4.1.1 of the PWRF model for simulated Arctic clouds and radiative feedback processes needs to be extensively evaluated.
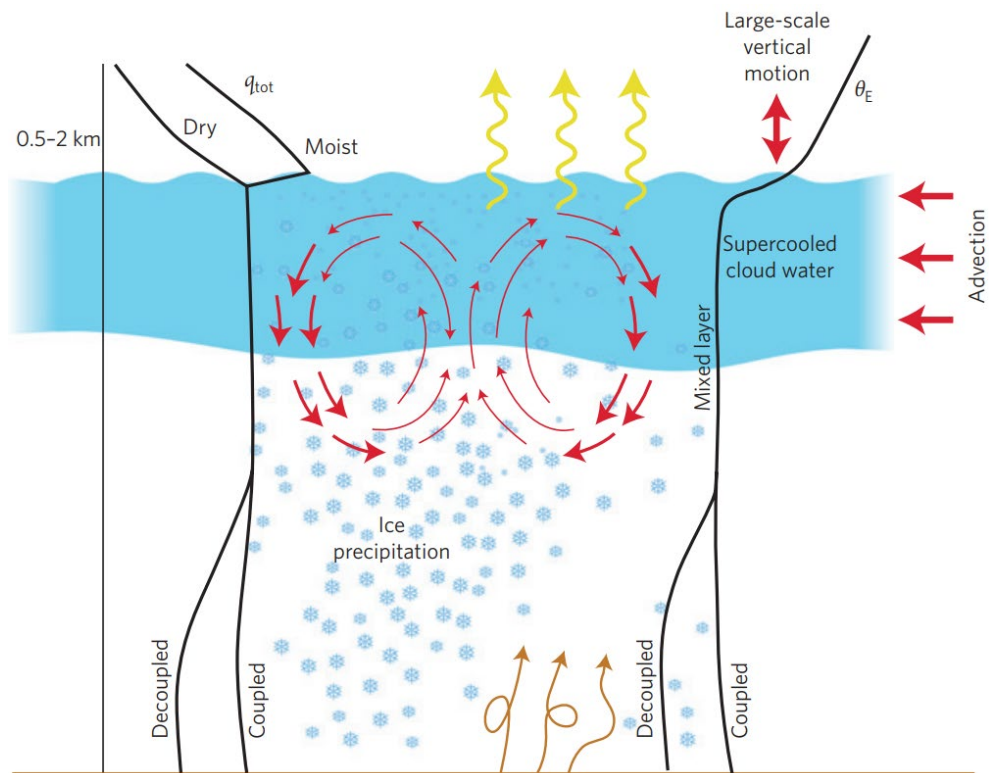
Figure 1. A conceptual model illustrating the primary processes and basic structure of Arctic mixed-phase clouds. Figure adapted from Morrison et al. (2012).

1.2 Scientific Questions

The specific scientific questions of this study are as follows:

(1) What are the characteristics of Arctic mixed-phase clouds, and how do cloud microphysical processes affect the persistence of mixed-phase clouds?

Hydrometeors in the liquid and ice phases typically vary in size and shape, nucleation, growth and evaporation, and rate of fall (Pruppacher and Klett, 2012). All of these properties affect the way they interact with the radiation in the atmosphere and the efficiency with which they grow to precipitation size. Mixed-phase clouds are formed in the Arctic boundary layer (Shupe et al., 2008a,b; Lawson and Zuidema, 2009; de Boer et al., 2009; Morrison et al., 2011, 2012) and consist of a thin layer of supercooled liquid water at the top and falling ice particles below (Rauber and Tokay, 1991; Shupe et al., 2008a). Shupe et al. (2006) showed that mixed-phase clouds occur about 40% of the time in the western Arctic, most frequently during the transitional period from spring to autumn and with a significant presence during the cold and dark Arctic winter.

A study using ground-based measurements at the Atmospheric Radiation Measurement North Slope of Alaska (NSA) site between

October 2006 and September 2009 (Qui et al., 2015) found an annual mixed-phase cloud occurrence of 42.3%, with the highest occurrence in October (72%) and the lowest in March (10%). The increase in mixed-phase cloud occurrence during winter is mainly due to increased moisture inversion intensity threshold. The resilience of mixed-phase clouds has also been extensively studied with different hypotheses (Pinto, 1998; Morrison et al., 2012). Studies have found a high occurrence of humidity inversion near the top of the mixed-phase cloud, which served as a source of moisture to persist in the Arctic environment (Solomon et al., 2011, 2014; Qiu et al., 2015). Due to the limitation of surface measurement sites and short study time, the characteristics of mixed-phase clouds only represent the local environmental effect. Therefore, the formation and persistence of mixed-phase clouds and their interactions and feedbacks with the Arctic environment need further investigation.

(2) What is the performance of current model simulations on the occurrence of Arctic mixed-phase clouds, and to which cloud microphysical processes is the PWRF model simulation most sensitive in estimating the amount of mixed-phase clouds?

Recent studies have shown that the Arctic is the most sensitive to

climate change, where clouds exert a significant influence on the radiative flux and surface energy budget associated with climate feedback (Carrett and Zhao, 2006; Bennartz et al., 2013). Mixed-phase clouds are known to be the most frequently observed cloud type over the Arctic (Shupe, 2011), so misrepresentation of these clouds has a large potential to increase model simulation uncertainties associated with climate change projections. However, the representation of Arctic clouds and their climate feedback in climate models remains challenging (Xie et al., 2013; Barton et al., 2014; English et al., 2014) due to poor understanding of the complex interactions with the surrounding environment, local dynamics, formation, persistence, and dissipation processes.

The number of mixed-phase clouds simulated by cloud microphysics schemes is influenced by the effects of droplet activation, droplet number concentration, nucleation processes, turbulence, and vertical velocities. Morrison and Pinto (2005) have shown that neglecting the subgrid vertical velocity results in weak activation and low droplet number concentrations (<90 cm^{-3}), suggesting that model simulation of mixed-phase cloud formation is sensitive to the treatment of nucleation processes and droplet number concentrations. In addition, the parameterization of the vertical velocity of cloud droplets should be

better characterized in the cloudy boundary layer. The parameterization of the ice parameters particle fall speeds (Harrington et al., 1999), collection efficiency for riming, and crystal habit (Lohmann et al., 2003) in the model are also sensitive in modeling Arctic clouds. A more detailed assessment of the sensitivity of the model to the different ice parameters should be investigated.

1.3 Objectives of this study

To answer the above scientific questions, this study aims to understand the microphysical properties of Arctic clouds in the PWRF model and to assess the radiative effect of mixed-phase clouds on observations and model simulations.

The specific objectives of this work are the following:

(1) To investigate the spatiotemporal variability of Arctic cloud properties.

(2) To identify characteristics of Arctic mixed-phase cloud properties associated with radiative effects.

(3) To compare discrepancies in cloud microphysical properties between PWRF cloud microphysical schemes.

(4) To analyze the contribution of Arctic mixed-phase clouds to the radiative effect in PWRF simulations.

Chapter 2. Data and model description

2.1 ACLOUD campaign

Comprehensive airborne in-situ measurements of cloud microphysical properties were performed over Svalbard during the ACLOUD campaign (May-June 2017) as part of the ArctiC Amplification: Climate Relevant Atmospheric and SurfaCe Processes and Feedback Mechanisms (AC)[3] project (Ehrlich et al., 2019; Wendisch et al., 2019). In this campaign, the Polar-6 aircraft is equipped with in-situ instruments to measure microphysical and optical properties of clouds using five different optical array and scattering probes: the Cloud Droplet Probe (CDP), the Cloud Imaging Probe (CIP), the Precipitation Imaging Probe (PIP), the Small Ice Detector Mark (SID-3), and the Particle Habit Imaging and Polar Scattering Probe (PHIPS). The CDP, an optical forward scattering spectrometer, operated in the size range of 2-50 μm using a single-mode diode laser at a wavelength of 0.658 μm (Wendisch et al., 1996; Lance et al., 2010). It provided counts and size measurements of individual droplets in 1 μm size bins for small droplets (2-14 μm) and 2 μm size bins for larger cloud droplets (16-50 μm).

The liquid water content (LWC) and effective droplet diameter (D_{eff}) were derived from the particle number size distribution (PNSD) using Mie theory particle size determination, followed by correction using a

Monte Carlo inversion method. The CIP used optical array probes (Knollenberg, 1976; Baumgardner et al., 2011) to measure the size and shape of cloud particles. It analyzed particle dimensions and shapes in the size range 25-1550 μm (25 μm resolution and 64 diodes) and determined crystal diameter (Baker and Lawson, 2006) and its mass-diameter relationship (Brown and Francis, 1995; Mioche et al., 2017).

The CIP provided the mean mass diameter (MMD) and ice water content (IWC) using the method described by Crosier et al. (2011). The vertical profiles of air temperature, pressure, relative humidity, and wind measured by sensors installed in a nose boom of the aircraft were used for analysis (Hartmann et al., 2018).

Temperature measurements during the ACLOUD campaign were corrected for adiabatic heating caused by dynamic pressure in slightly unstable or stable stratification conditions where turbulent heat fluxes are small. This correction is important because temperature measurements were used to derive turbulent fluxes at the atmospheric boundary layer. In addition, only straight and level flight measurements were used due to calibration problems with the five-hole probe.

Clouds were categorized into three types, namely liquid, ice, and mixed-phase clouds, using the ice water fraction (IWF) as a criterion. The IWF is calculated by dividing the LWC by the sum of the LWC and IWC

(Korolev and Milbrandt, 2022). Clouds with an IWF greater than 0.95 (or less than 0.05) were classified as ice (or liquid) clouds, while mixed-phase clouds were characterized by an IWF between 0.05 and 0.95.

2.2 Cloud radar data

The Cloudnet retrieval algorithm suite (Illingworth et al., 2007, Nomokonova et al., 2019) is applied to the AWIPEV atmospheric observatory measurements. This provides vertically resolved information on the presence of cloudiness, ice, melting ice and drizzle/rain in each radar height bin. In conjunction with numerical weather prediction data, cloud radar reflectivity, Doppler velocity and ceilometer attenuated backscatter profiles are analyzed. The resulting categorization profiles provide information up to a height of about 12 km with a temporal and vertical resolution of 30 s and 20 m, respectively.

Based on this target classification, LWC, IWC, and the effective radii of the liquid (re_{liq}) and ice (re_{ice}) are determined. Depending on the cloud situation, different microphysical retrieval algorithms are applied. If ice particles are present, the IWC is calculated from the radar reflectivity Z and temperature T (Hogan et al., 2006), which is also a standard Cloudnet algorithm. Ice particle effective radius is calculated following Delanoë and Hogan (2010), with IWC and visible extinction coefficient as inputs.

The latter is also calculated depending on Z and T (Hogan et al., 2006). The relative uncertainties for the effective radius of the ice are reported to be in the order of 30% (Delanoë and Hogan, 2010). When both ice and liquid are present in a radar bin, ice dominance of the signal in Z is expected (Shupe et al., 2004), and the same retrievals are applied as for pure ice cloud. For all radar bins containing cloud droplets, LWC and re_{liq} are retrieved.

For single-layer water clouds, the LWC can be calculated using the relation given by Frisch et al. (1998). Here, the microwave radiometer (MWR) liquid water path (LWP) is vertically distributed following the radar reflectivity profile shape. This method also works for cases where the ice cloud is located on top of the single-layer of liquid cloud. The effective radius of the liquid, re_{liq}, in these cases is derived from Frisch et al. (2002), which also uses the LWP and Z as inputs. It should be noted that, a log-normal droplet size distribution with a fixed spectral width is set to 0.3. For the effective radius of the liquid they found an uncertainty of about 20%.

In particular, when both liquid and ice are present in a single radar bin, Frisch et al. (1998) technique is inapplicable because radar reflectivity related only to liquid drops are not known. Thus, in this case, we calculate an adiabatic LWC profile and scale it so that the integrated

liquid water content equals the observed LWP from the MWR. A similar approach is also used for multilayer liquid clouds in Shupe et al. (2015), where a scaled adiabatic method is used. The effective radius for these cases was taken as 5mm, the median value of the liquid effective radius for all observed cases from Ny-Ålesund, where the algorithm of Frisch et al. (2002) was used. Note that for rain or drizzle particles, no microphysical properties are retrieved. Also when rain or drizzle occurs in a liquid cloud, the methods of Frisch et al. (1998) and Frisch et al. (2002) are not applicable. In such cases, Z is dominated by the few large rain droplets and is no longer proportional to the LWC. For this reason, a scaled adiabatic LWC profile and the climatological value of re_{liq} are assumed. Recently, Nomokonova and Ebell (2019) published this dataset of retrieved cloud microphysical properties.

2.3 Surface radiation data

The Baseline Surface Radiation Network (BSRN) measures the surface radiation flux with the greatest possible accuracy at selected sites in various climatic zones with well-defined and calibrated state-of-the-art instruments. To date, more than 50 anchor sites worldwide report high temporal resolution (1 minute data) measurements of both shortwave and longwave downward radiation to the World Radiation Monitoring Centre (WRMC). The Ny-Ålesund station is

13

located in a fjord on the west coast of Svalbard (Spitsbergen), where the mountains to the south determine the length of the potential sunlight period at the site. The time resolution of the radiation data is one minute. More details on the in-situ observations at the buoy stations can be found on the official website of the buoy stations (https://www.pmel.noaa.gov/gtmba/).

2.4 PWRF model configuration

Clouds were simulated in the Polar-optimized Weather Research and Forecasting model (PWRF 4.1.1; http://polarmet.osu.edu/PWRF/) using four different cloud microphysics schemes. PWRF optimizes the Noah land-surface model for surface energy balance and heat transfer, specifically for Arctic sea ice and permanent ice surfaces. Based on the work of Wilson et al. (2011, 2012), the land mask associated with sea ice was updated. In this study, the PWRF was applied with three two-way nested grids, with horizontal grid spacings of 27 km, 9 km, 3 km and 1 km, and 45 vertical levels in the lowest 5 km of the atmosphere. The surface boundary conditions were obtained from the 6-hourly final analysis of the Global Forecast System (CGS) of the National Centers for Environmental Prediction (NCEP) (FNL; NCEP 1999). Forecasts for each cloud microphysics scheme were tested 18 hours prior to the start of the

flight time for each case. The first 6 hours of each simulation were considered to be a spin-up period to ensure that the results were accurate, while the remaining 12 hours were used for the evaluation. The macrophysical options used in the PWRF model runs were consistent with those described in Hines and Bromwich (2017), which includes the Mellor-Yamada-Nakanishi-Niino (MYNN) fast radiative transfer model, the MYNN-2.5 level TKE boundary layer, and the newGrell convective scheme.

Many WRF model studies have compared the ability of the cloud microphysics scheme to represent the cloud phase and the radiative biases derived at the surface. Numerous studies have used the WRF single-moment five-class scheme (WSM5) (Powers, 2007; Li and Pu, 2008; Otkin and Greenwald, 2008; James et al., 2009; Huang et al., 2009; Shafer et al., 2009), WRF double-moment six-class scheme (WDM6) (Hong et al., 2010; Lim and Hong, 2010; Bae et al., 2016; Halder and Mukhopadhyay, 2016; Guo et al., 2019), Morrison (Halder et al., 2015), National Severe Storms Laboratory (NSSL) two-moment microphysics (Johnson et al., 2016; Khain et al., 2016; Li et al., 2017), and Predicted Particle Property Scheme (P3) (Gevorgyan, 2018; Hines et al., 2019; Huang et al., 2021; Hua et al., 2023) microphysics options to evaluate the performance of WRF for simulating clouds and precipitation over

different weather phenomena and regions.

In this study, four cloud microphysics schemes were selected from a total of 32 options for the following reasons. The Morrison scheme, which is widely used in the polar region and is the basic cloud microphysics scheme optimized for the polar region (Morrison et al., 2009). The WDM6 scheme produces a large amount of ice compared to other schemes, which may have an advantage in simulating mixed-phase clouds in the Arctic region (Lim and Hong, 2010). A newer version of the NSSL scheme, which additionally predicts the bulk volume of hail/graupel. This means that the bulk density of hail/graupel in this scheme is not constant as in other schemes (Mansell et al., 2010). The P3 scheme represents the microphysics of ice by predicting particle properties rather than separating ice into different ice categories as in other schemes (Morrison and Milbrandt, 2015).

- The Morrison scheme is a two-moment microphysics scheme that parameterizes the mixing ratio and number concentration of hydrometeors, including cloud droplets, rain, ice crystals, snow, and graupel.

- The WDM6 scheme predicts the mixing ratio of six water species (water vapor, cloud droplets, rain, ice crystals, snow, and graupel) and the number concentration of cloud droplets, rain,

and cloud condensation nuclei (CCN). The WDM scheme is a competitive option in WRF by reproducing.

- The NSSL scheme simulates the mass and number concentration of six hydrometeor types (cloud droplets, rain, ice crystals, snow, graupel, and hail) and includes the prediction of the bulk number concentration of CCN and the density of graupel, allowing graupel to represent both high-density hail and low-density graupel.

- The P3 scheme calculates various properties of ice crystals within a single ice category using four predictive ice-related variables: total ice crystal number concentrations, rimmed ice mixing ratio, deposited ice mixing ratio, and rimmed volume mixing ratio. Unlike traditional microphysics schemes, this scheme does not employ an auto-conversion parameter for solid phase particles (ice crystals, snow, and graupel/hail). However, it still uses a standard double-moment approach for the liquid phase hydrometeors (cloud droplets and rain), similar to the other three schemes.

A designed, systematic exploration of the required model initialization and setup. This approach considers the best prediction for the Arctic environment around Ny-Ålesund, Svalbard.

Two methods are compared to see which collocation method is best suited for comparing model results with flight observations. The moving average is calculated every minute, while the 4D interpolation method is calculated every second, following the observation time. This time-averaging already produces a discrepancy of data that can be used for evaluation (moving average: 282, 4D interpolation = 16901).

Spin-up times of 1, 7, 13, 19, and 25 hours were compared for each method. The temperature correlation with 1-hour spin-up is 0.91 for both methods, while the correlation increases to 0.92 for 7 hour spin-up. This means there is not much difference between the moving average and 4D interpolation methods. Therefore, 4D interpolation is chosen because more data points can be used for the analysis.

Grid spacing and nesting tests are carried out. Simulations were run from 27 km nesting down to 9 km, 3 km, and 1 km, showing clear improvements in terms of lower error when the grid spacing is reduced from 27 km to 1 km. However, both 1 km and 3 km simulations tend to predict temperature well, with a correlation of 0.90. The 1 km simulation (1126) is chosen because it has the most data points.

Chapter 3. Arctic cloud properties at Ny-Ålesund, Svalbard

3.1 Definition of diagnostics

In this chapter, the vertical structure of clouds at Ny-Ålesund is characterized using lidar-radar synergy, together with the additional constraints for the separation of liquid and ice from mixed-phase clouds. The Cloudnet algorithm suite (Illingworth et al., 2007) combines observations from a synergy of ground-based instruments. The Cloudnet output includes several products, such as a cloud target classification and microphysical property products. In order to provide complete vertical information on clouds, Cloudnet requires measurements from a Doppler cloud radar, a ceilometer-lidar, a microwave radiometer and thermodynamic profiles from a numerical weather prediction (NWP) model. The 94 GHz FMCW JOYRAD-94 cloud radar, the CL51 ceilometer and the HATPRO MWR are used at the Ny-Ålesund station. The NWP icosahedral non-hydrostatic model (ICON) is used to derive model data. Lidar backscatter and Doppler radar parameters are analyzed with model thermodynamic profiles (Hogan and O'Connor, 2004) for target classification. The target classification consists of the categories aerosols and insects, insects, aerosols, melting ice and cloud droplets, melting ice, ice and supercooled droplets, ice, drizzle rain and cloud droplets, drizzle

19

or rain, cloud droplets only, and clear sky.

In order to differentiate the cloud phase (liquid, ice, and mixed) and to identify different cloud types, the target categorization of Cloudnet is used and additional constraints are applied to the categorization. The ratio of IWC to total water content indicates how much ice crystals are included in the total water content. This ice water fraction (IWF) above 0.95 and below 0.05 indicates that the amount of ice observed in a cloud column is not statistically suitable to be considered as a mixed-phase cloud. The monthly variation of the IWF density is shown in **Figure 2**. Liquid-dominated mixed-phase clouds occur most frequently in May, suggesting that characterizing mixed-phase clouds during the melt season could lead to a bias in the partitioning between ice and liquid layers. For this reason, this paper uses the Cloudnet algorithm's mixed-phase cloud classification threshold (**Figure 3**), where all mixed-phase clouds with IWFs greater (less) than 0.95 (0.05) are considered to be ice (liquid).

Clouds are classified into single-layer and multi-layer clouds in addition to the occurrence of hydrometeor types. Single-layer clouds are further classified into liquid phase, ice phase and mixed phase clouds. To classify, each Cloudnet profile is examined from top to bottom for cloud layers. Clouds are defined as layers of at least three consecutive cloud heights.
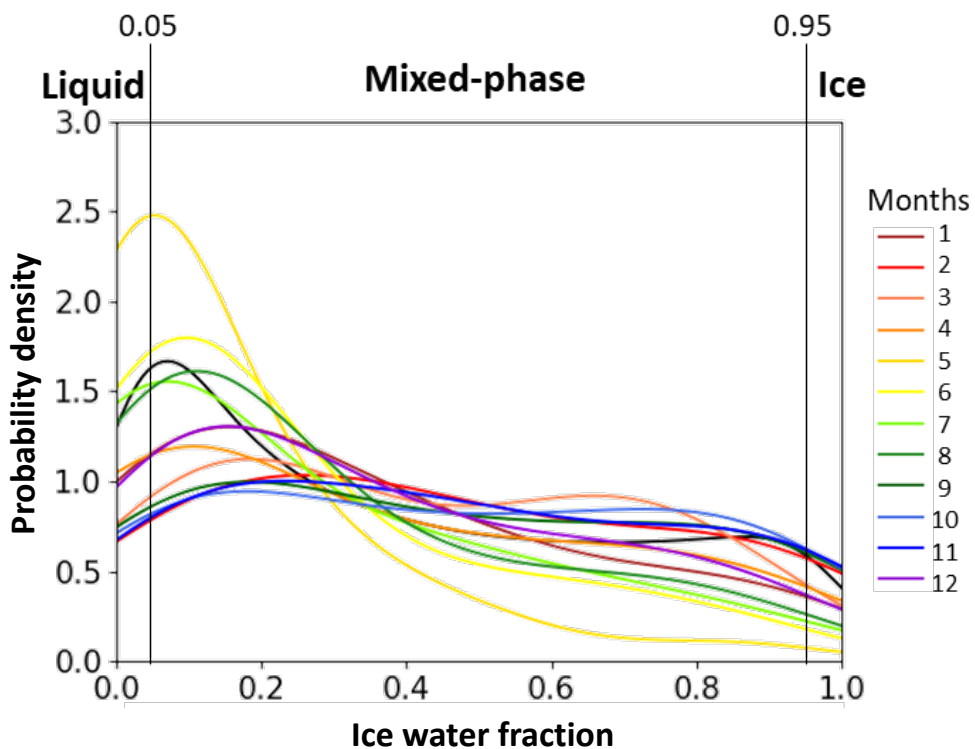
Figure 2. Probability density of ice water fraction observed during the study period at Ny-Ålesund.

Based on the number of cloud layers identified, clouds were classified as single or multilayered. Cases were considered to have multilayers, where one or more clear sky height bins separated two or more cloud layers. Using the wet bulb temperature calculated from the model data, the Cloudnet algorithm identifies the 0°C isotherm for classification. Therefore, at temperatures close to 0°C, model uncertainties can lead to misclassification of liquid ice. For cloud precipitation, model uncertainties are reduced by the Cloudnet algorithm using radar Doppler observations. A significant gradient in the vertical velocity of the particles is used by the algorithm to identify the 0°C isotherm.
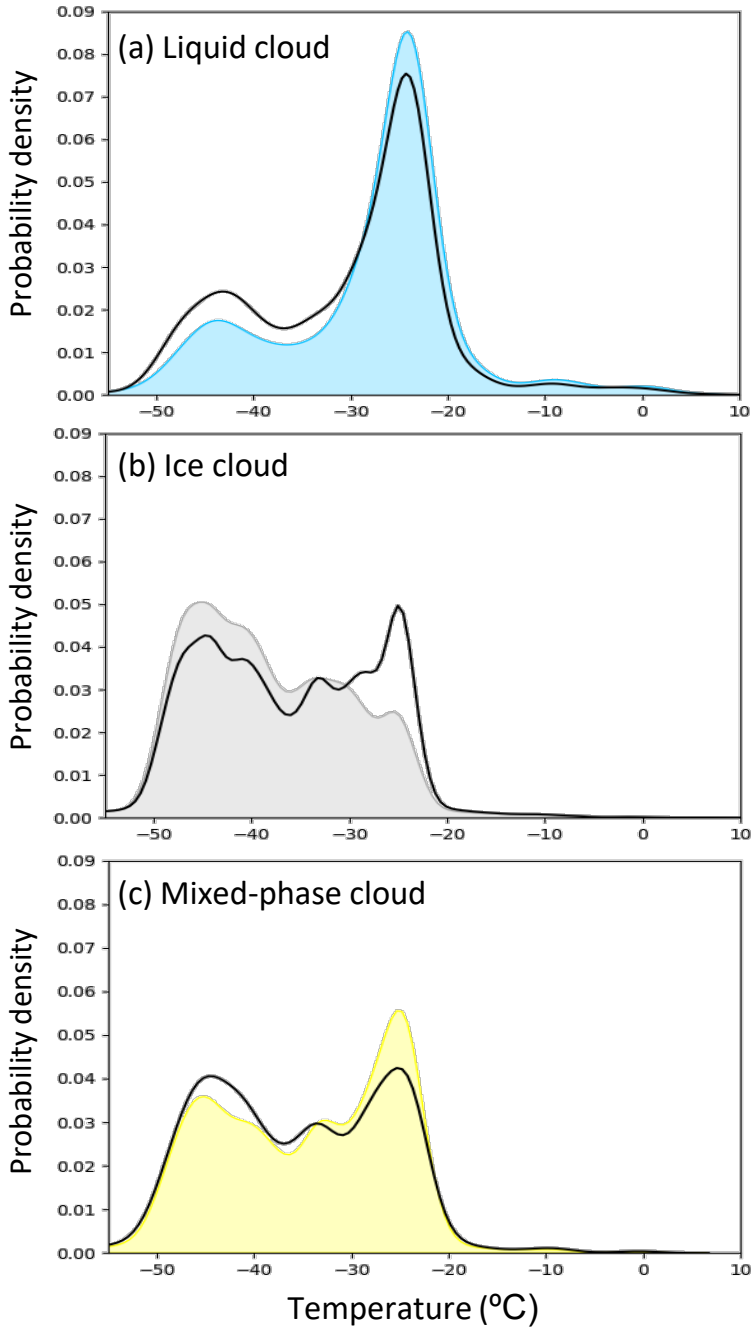
Figure 3. Probability density of (a) liquid, (b) ice, and (c) mixed-phase cloud using Cloudnet algorithm (contour) and ice water fraction threshold method (black line).

3.2 Classification of hydrometeors and clouds properties

An overview of the occurrence of cloud types in Ny-Ålesund for the whole period of this study is shown in **Figure 4.** The availability of the cloud network is above 90% for most months. The exception is from 09 October 2018 to 11 June 2019, when cloud radar observations are missing. The total number of cloud network profiles analyzed per month is about 81 thousand. The frequency of cloud occurrence is on average ~46%, with the highest in August and October 2017 (~79%) and the lowest in March 2018 (~31%).

A cloud is considered to be mixed if both ice and liquid are present at the exact boundary of the cloud, regardless of whether the liquid and ice are in the same region. In other words, mixed-phase cloudiness encompasses instances where the top of the cloud is liquid and the bottom is ice, as well as instances where both phases (ice and liquid) occur somewhere within the detected cloud base. Examples of cloud classification using the Cloudnet algorithm can be seen in **Figure 5**, where the total number of clouds over the entire data period is 77.6%, the number of single-layer clouds is 37.2%, and the number of mixed-phase clouds is 14.9%. Among the occurrence of mixed-phase clouds, the frequencies of whether the mixed-phase layer was present at the base,

middle, or top of the total cloud thickness were 1.9%, 5%, and 8%, respectively. This indicates that most of the mixed-phase layer was in the middle and top layers of the total cloud thickness.

Seasonal and monthly variability is also evident in the monthly occurrence of single-layer liquid and ice clouds (**Figure 6**). Approximately 15% of the single-layer liquid clouds were detected in summer, but less than 2% in other months. Ice cloud occurrence is 15-20% in winter and spring and less than 5% in other months. Single-layer mixed-phase clouds and multi-layer clouds were present most of the time, with typical frequencies of about 20% and 45% respectively. This suggests that the cloud systems are associated with complex microphysical processes, with most having a complicated structure and/or consisting of both liquid and ice phases. Conversely, the observational capabilities of these types of clouds are limited. In situations with multiple liquid layers, whether warm or mixed phase, the distribution of observations between these different layers is particularly challenging and leads to more significant uncertainties (Shupe et al., 2015).
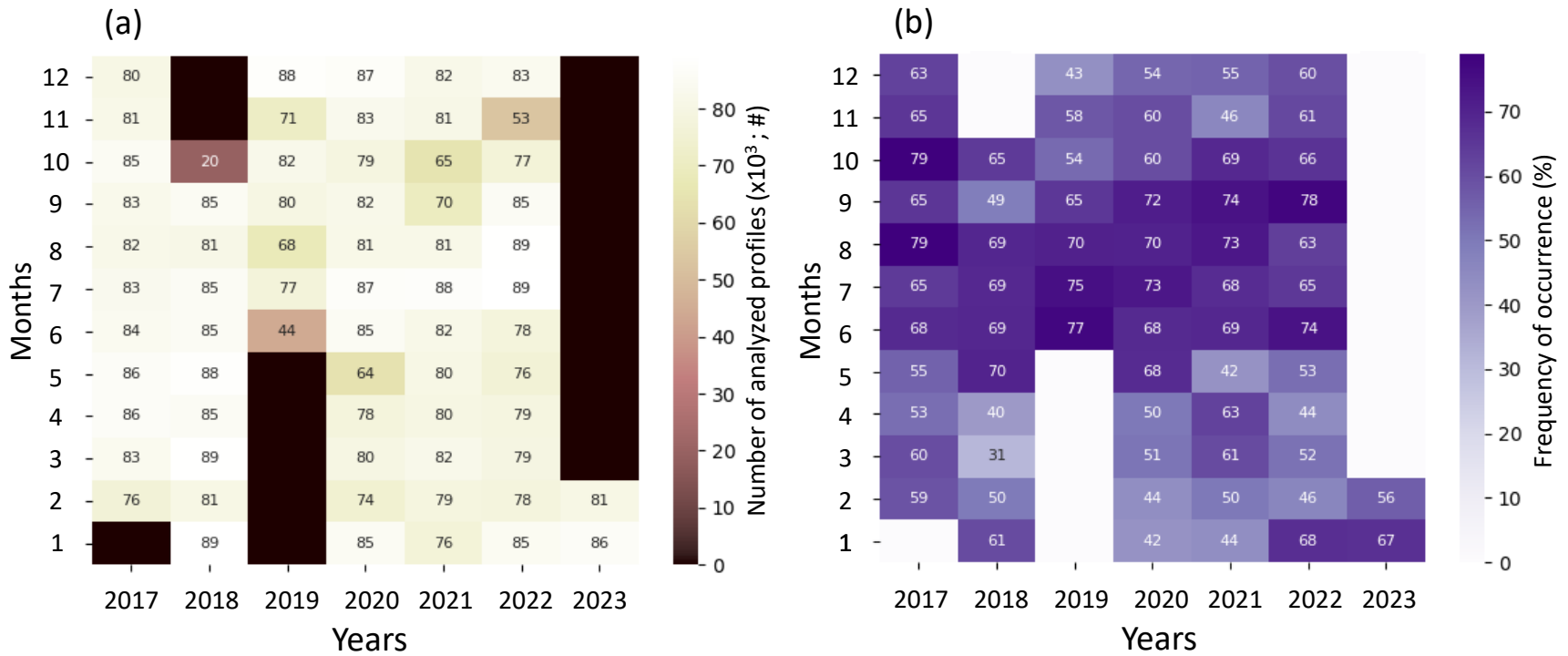
Figure 4. Cloudnet (a) data availability and (b) frequency of cloud occurrence at Ny-Ålesund station from February 2017 to February 2023. The absence of data for the month is shown in (a) black and (b) white contour.
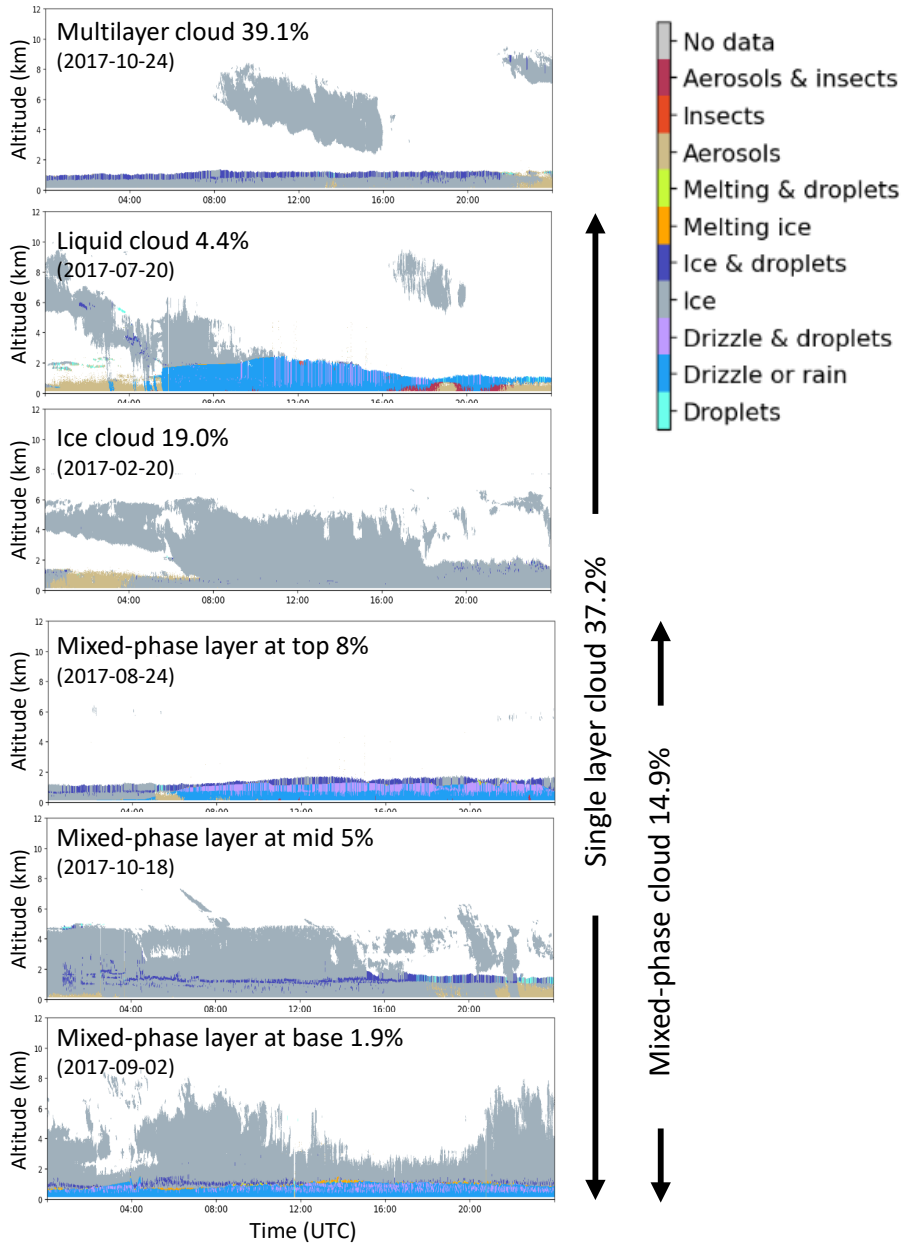
Figure 5. Example of cloud classification (Multilayer, 24 Oct 2017; liquid, 20 July 2017; ice, 20 Feb 2017; mixed-phase layer at top, 24 Aug 2017; mixed-phase layer at mid, 18 Oct 2017; mixed-phase layer ab base, 2 Sep 2017) and frequency of occurrence from Cloudnet from February 2017 to February 2023.

The seasonal probability distributions of cloud occurrence as a function of height are shown in **Figure 7** for the data period February 2017 to February 2023. In general, clouds were more frequent below 5 km in height. In spring, where the cloud frequency was dominated by mixed-phase clouds (24%), the vertical distribution of the maximum in the lower troposphere is at 2.2 km with a CF of 0.09. In summer, the mean CF peaked at 0.08 at 1.9 km and decreased from 4.8 km upwards. In autumn and winter, the CF is about half as low as in spring and summer.

The classification of multi-layer clouds requires a reliable profiling of the liquid layers, which is limited by the significant attenuation of the lidar signals in the first liquid layer. Compared to lidar, radar is better at propagating through the entire vertical cloud structure. This can mask the presence of small particles, e.g. liquid drops, in the same volume. Therefore, radar reflectivity alone cannot reliably detect the liquid phase in multilayer mixed-phase clouds.

Figure 8 shows a statistical overview of the top temperature, cloud thickness, cloud top height, and cloud base height during the study period. The results refer to cloud layers where both the cloud base and the top layer are more than 30 m. The minimum geometric depth of the cloud is also 30 m. Average cloud top temperatures were 0°C for liquid clouds, -8°C for ice clouds, and -3°C for mixed-phase clouds. Cloud top

temperatures were slightly higher in summer and autumn and slightly lower in spring and winter. Note that the number of liquid cloud observations was less than 3% of the ice and mixed-phase cloud profiles.
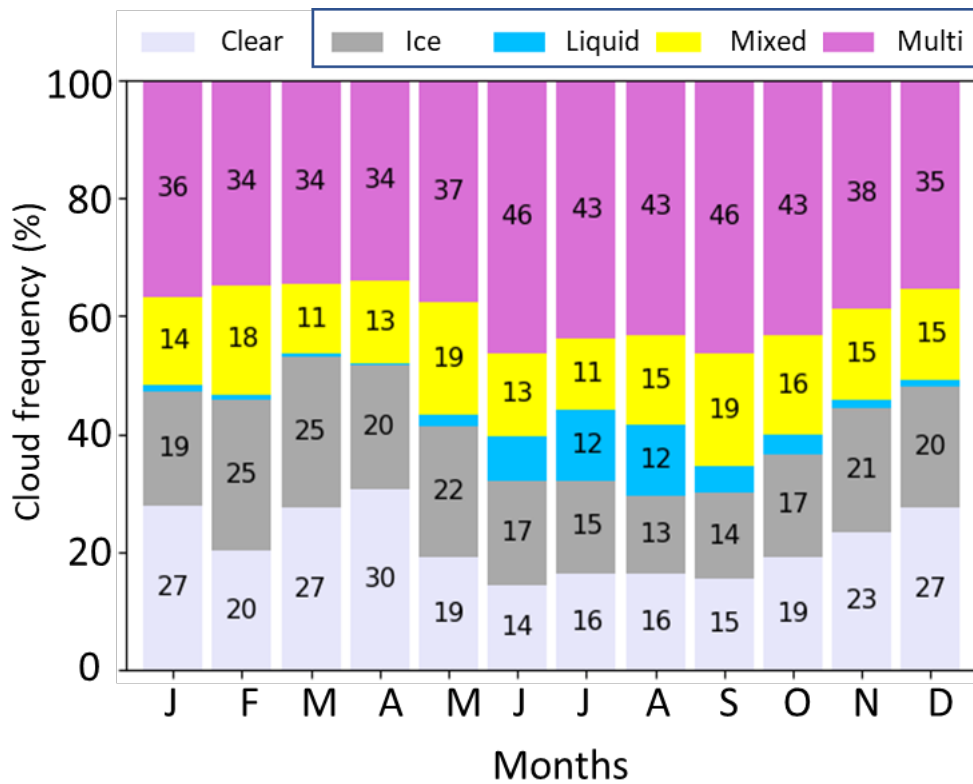
Figure 6. Monthly frequency of occurrence of different types of multilayer clouds, single-layer clouds (liquid, ice, and mixed-phase), and clear sky profiles from February 2017 to February 2023.
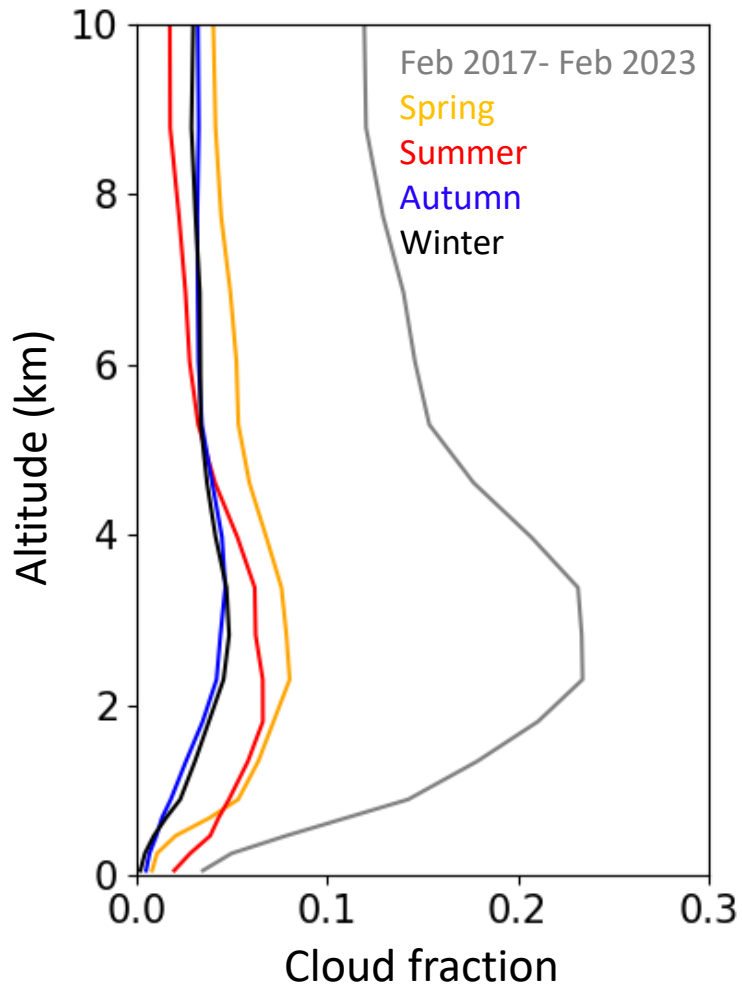
Figure 7. Profiles of cloud fraction for the data period February 2017 to February 2023 and each season: Spring (yellow), Summer (red), Autumn (blue), and Winter (black).

The seasonal characteristics of cloud top and base heights for liquid clouds differ from those of ice and mixed-phase clouds, which are relatively unchanged in vertical distribution between summer and autumn. However, the ice and mixed-phase clouds had higher cloud top height and constant cloud thickness during spring, autumn, and winter. It is known that the increase in top height and cloud thickness of mixed-phase clouds with precipitation is associated with the passage of a low-pressure system (Achtert et al., 2014).

The clouds observed from February 2017 to February 2023 were shallow, with a mean geometric thickness of 620±1308 m. Liquid clouds were found to be the thinnest throughout the season with little variation with a mean of 1419±1879 m. Ice clouds were the thickest with a mean of 1645±2128 m, having a similar mean throughout the season. Mixed-phase clouds were consistently thick, with a mean of 1596±1957 m. It should be noted that these statistics are dominated by three cloud types in summer but by ice and mixed-phase clouds in spring, autumn, and winter.
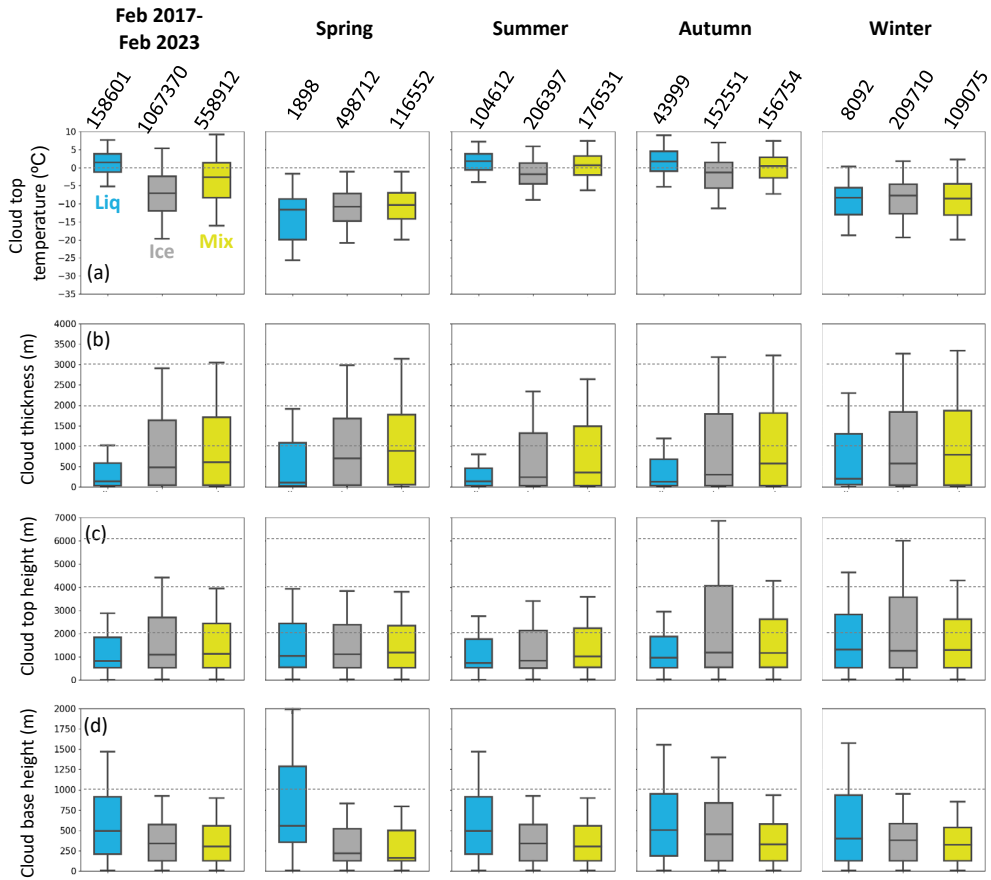
Figure 8. Statistical overview of cloud occurrence with respect to (a) cloud top temperature, (b) geometric thickness, (c) cloud top height, and (d) base height from February 2017 to February 2023 for all (first column) and each season (2nd to 5th column). The colors indicate the different cloud types: liquid (blue), ice (grey), and mixed (yellow). The numbers in the top panel indicate the number of profiles considered in each analysis.

Monthly observed time-height cross-sections of simulated LWC and IWC are shown in **Figure 9**. The observations show a liquid top mixed-phase cloud with an ice cloud base during the summer months. The amount of IWC decreased in autumn and increased in winter near the surface with a relatively high value (0.09 g m^{-3}). The simulated cloud base height of liquid clouds (**Figure 8**), which frequently occurred in summer, was high compared to ice or mixed-phase clouds. This feature generally corresponds to near-surface precipitation, where the observed signal is classified as precipitation rather than cloud. The frequency distribution of LWC and IWC of different cloud types is shown in **Figure 10**. There are almost no differences between cloud types in both distributions with a peak at about 10^{-1} g m^{-3} for LWC and 7.3×10^{-2} g m^{-3} for IWC. The mixed-phase clouds appear to follow both the liquid and ice cloud distributions.
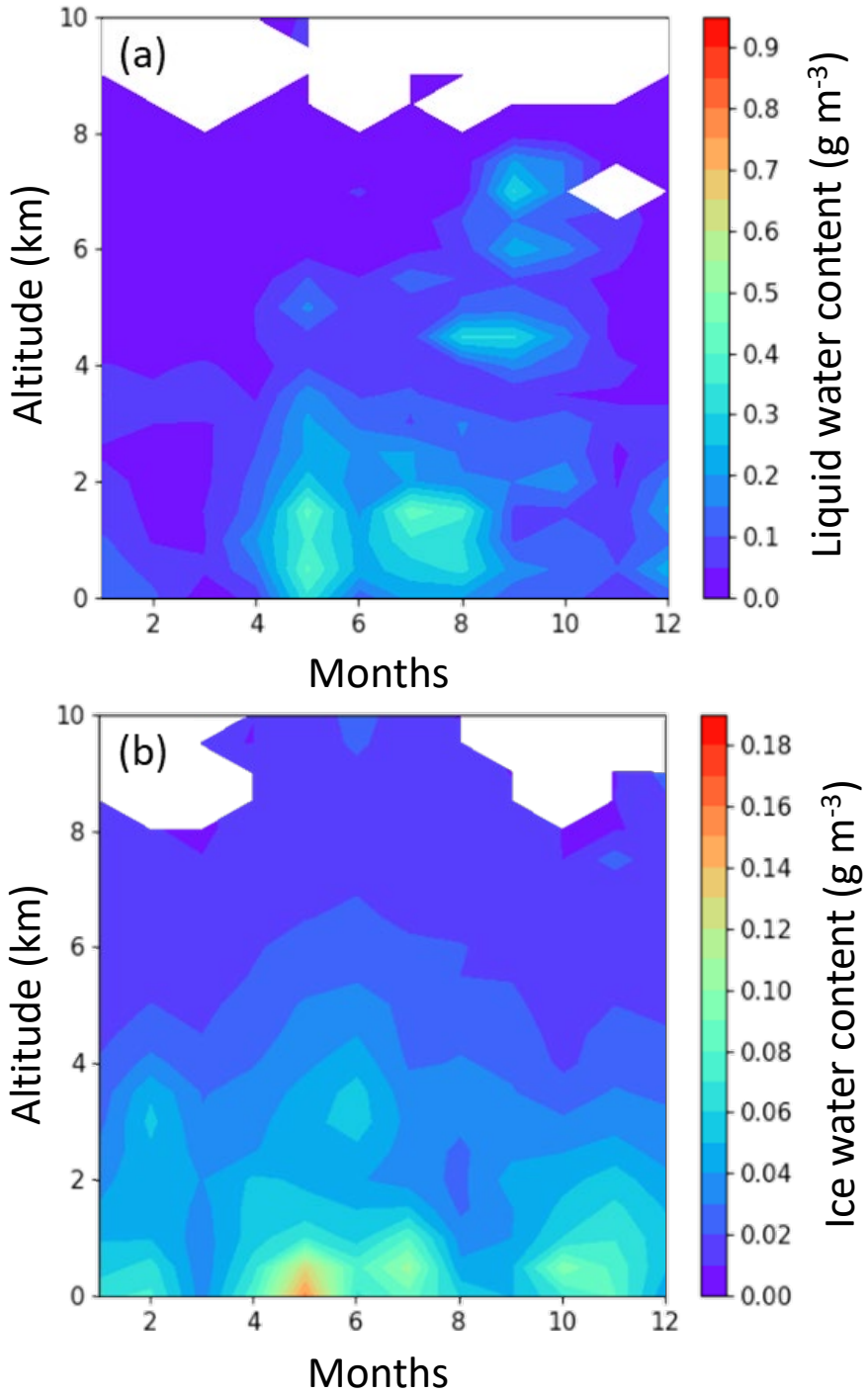
Figure 9. Monthly cross-sections of (a) liquid water content and (b) ice water content from Cloudnet observations.
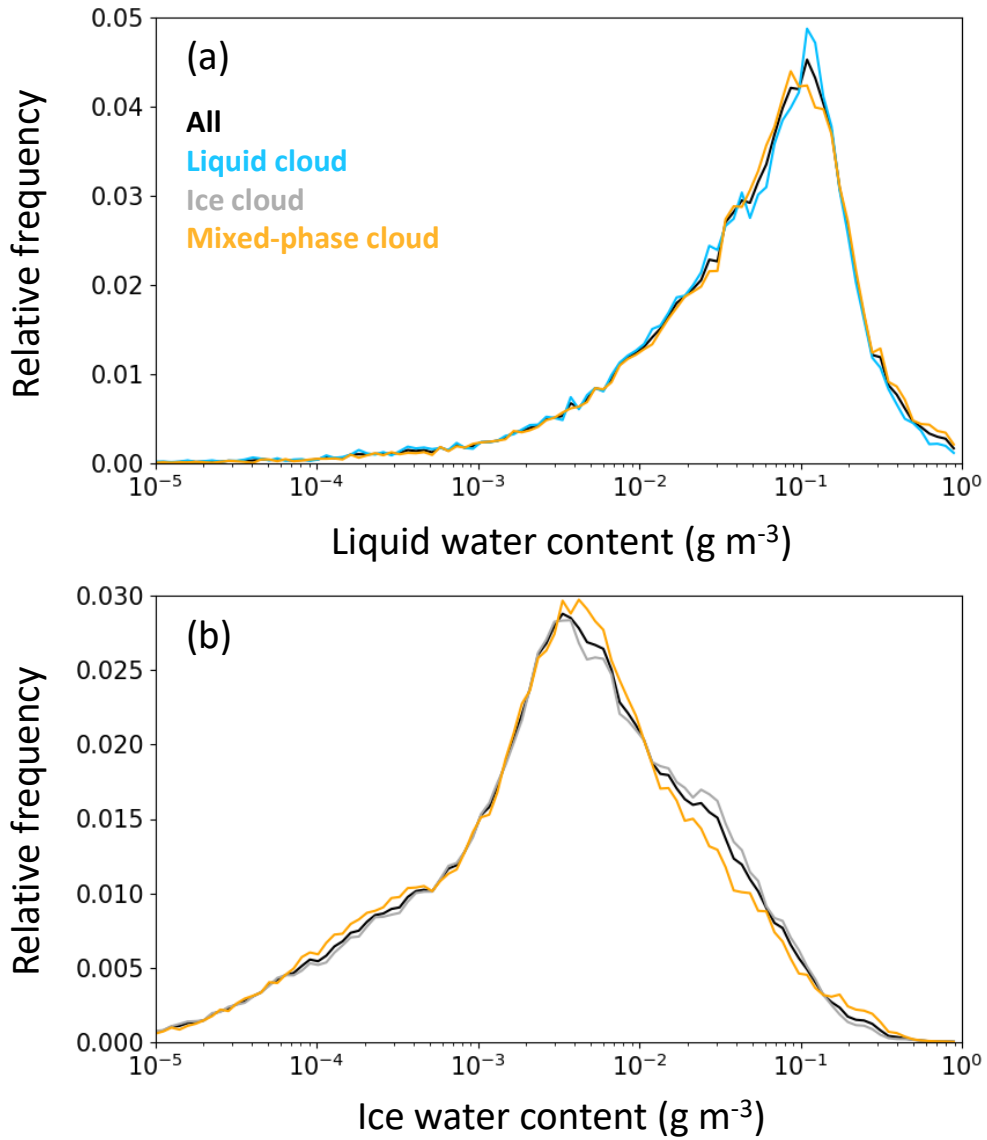
Figure 10. Histogram of the frequency of occurrence of (a) liquid water content and (b) ice water content for all (black), liquid (blue), and mixed-phase (yellow) clouds from February 2017 to February 2023.

Figure 11 shows the amount of ice, liquid, and mixed-phase cloud re-distributed in terms of temperature. The new method seems to categorize mixed-phase clouds into ice clouds at a temperature range -21~-25°C but reducing ice clouds at a temperature range -40 to 45°C. Liquid cloud, on the other hand, shows the opposite structure where cloud is categorized more at -40°C and lowered at -20°C.
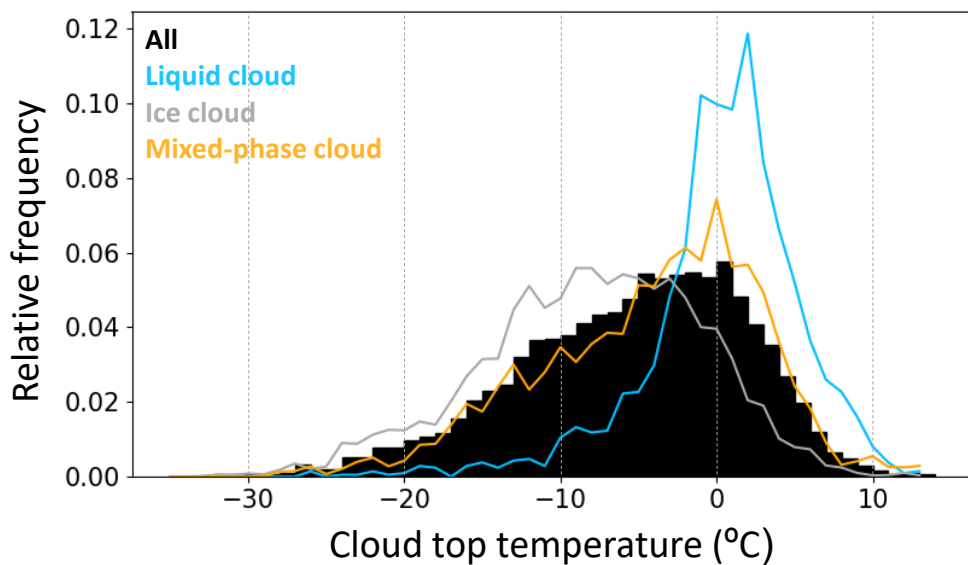
Figure 11. Relative frequency of cloud top temperature for each all (shaded), liquid (blue), ice (grey), and mixed-phase (yellow) cloud during Feb 2017 to Feb 2023 over Svalbard, Ny-Ålesund.

3.3 Statistics of Arctic mixed-phase clouds and their radiative effect

One of the most important cloud characteristics determining the radiative properties is the composition of the cloud phase (Sun and Shine, 1994; Yoshida and Asano, 2005). The radiative effect of liquid cloudiness is greater than that of icy cloudiness (Shupe and Intrieri, 2004). Phase partitioning is of particular importance in the Arctic, where clouds consisting of liquid and mixed phases can persist for several days (Morrison et al., 2012). Intrieri et al. (2002) and Shupe and Intrieri (2004) have shown that during the polar winter, liquid clouds strongly influence the net radiative effect of clouds, resulting in increased surface warming. The authors also reported that in mid-summer the cloud-driven radiative cooling of the shortwave (SW) radiation dominates the warming of the longwave (LW) radiation. With the exception of the Summit station in Greenland, where the cloud radiative forcing effect is positive throughout the year due to the high surface albedo of the snow cover, SW radiative cooling of the surface has been reported for several Arctic regions this summer (Miller et al., 2015).

Clouds have an impact on the Earth's climate through cooling in the SW and warming in the LW. The macro- and microphysical properties of clouds determine their net radiative forcing. In the global hydrological

cycle, clouds also play an important role. In a complex system of climate feedbacks, the radiative effect of clouds on climate causes changes in clouds. One of the key climate variables identified in the WMO report is cloudiness, or CF, which is the fraction of the Earth's surface covered by clouds. CF is a strong determinant of the net cloud radiative forcing. Depending on their type (high or low), their amount of liquid or ice, and so on, they can cause cooling at top-of-atmosphere (TOA) in SW and heating in LW. The influence of the net TOA clouds radiation effect on the modulation of surface temperature trends through clouds radiation feedback (Stephens, 2005, Haugstad et al., 2017) is not well understood and can be addressed using model simulations, which are subject to large uncertainty in estimates of clouds radiation feedback.

BSRN observations have been used to analyze radiative forcing by cloud type in the Arctic region, where mixed-phase clouds are common. The frequency distribution of LW up (LWU), LW down (LWD), SW up (SWU), and SW down (SWD) for the cloud phase (liquid, ice, and mixed-phase) is shown in **Figure 12**. Liquid cloud had more cases of high LWU and LWD than ice or mixed-phase cloud. Liquid cloud also has a high relative frequency of SWU and SWD. While the LWU is dependent on the surface properties and temperature, the LWD is dependent on the atmospheric temperature and humidity and is strongly influenced by the

presence of clouds and the water vapor content of the atmosphere. Therefore, LW radiation fluxes will be higher at higher summer atmospheric temperatures with high liquid cloud cover. In winter, absolute values of LW radiation are lower due to atmospheric temperature and humidity and the radiative effect of clouds (ice and mixed-phase). Relatively lower values of LWU and LWD for ice and mixed-phase clouds were highly correlated with cloud top temperature by phase (**Figure 11**).
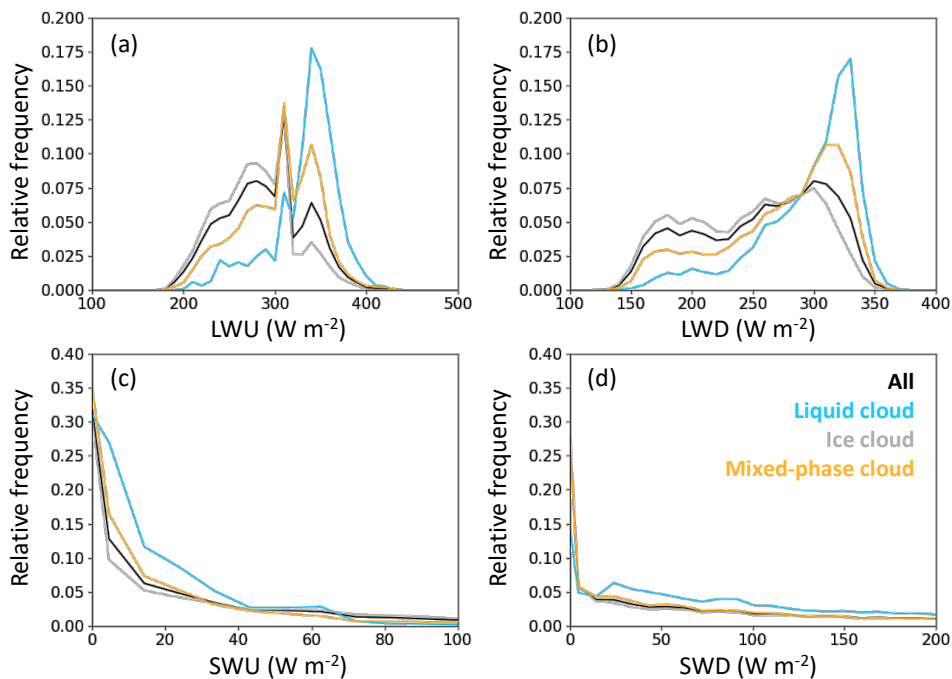
Figure 12. Histogram of the occurrence frequency of (a) longwave upward, (b) longwave downward, (c) shortwave upward, and (d) shortwave downward for all types (black), liquid (blue), ice (grey), and mixed-phase (yellow) cloud.

SW variability is found to be modified by surface texture, with spring being the onset of the snowmelt season for the Arctic region, which shows higher reflected SWU. SWU is also a key parameter driving summertime radiation changes in the ice-albedo feedback (Chapin et al., 2005). For SWU radiation of about 14 W m^{-2}. The net cloud radiative forcing is governed by the macrophysical (i.e., CF and cloud top temperature) and microphysical (i.e., phase, effective radius, and optical depth) properties of the clouds, which show large spatial and temporal variations (Saud et al., 2016; Ali et al., 2019; Kant et al., 2019). Note that the Ny-Ålesund BRSN station is affected by the axial tilt of the Earth, with the absence of solar radiation during the winter season.

Thus, the radiative flux at Ny-Ålesund, Svalbard, is only measured during the sunlit period. Therefore, in order to analyze the radiative effect in winter, the radiative flux for each cloud type simulated by the Cloudnet model was analyzed (**Figure 13**). The quantitative variability of surface and TOA net radiation in Ny-Ålesund is calculated for each cloud phase (i.e., ice, liquid, and mixed-phase) as categorized above.

The radiative forcing of liquid and mixed-phase clouds follows a similar pattern, and for ice and multi-layer clouds, the effect on the net radiative flux appears to be less. The amount of radiative energy absorbed by the net radiation at the surface is mainly controlled by the

SW radiation. Seo et al. (2023) show that net surface radiation absorption is on a rising trend, reaching over 70 W m^{-2} in summertime, when liquid and mixed phase cloudiness are dominant.
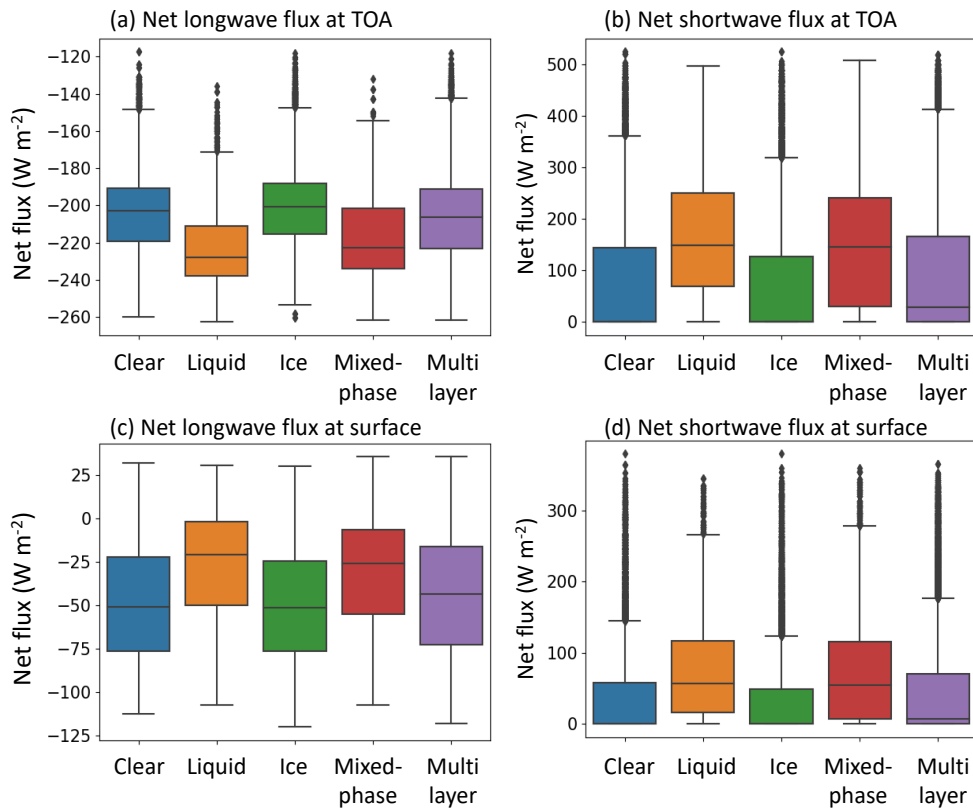
Figure 13. Net shortwave radiation at (a) the surface, (b) the top of the atmosphere, net longwave radiation at (c) the surface, and (d) the top of the atmosphere over Ny-Ålesund.

Figure 14 compares the cloud top temperature (CTT) with the net longwave radiation at TOA and surface for a mixed-phase cloud. The correlation between climate variability and cloud properties   and the radiation on mixed-phase clouds is analyzed. The comparison of the IWF threshold and the original cloud net categorization method shows that the use of the IWF threshold reduces the correlation between CTT and net surface and TOA longwave radiation. This could indicate that the amount of liquid or ice cloud re-categorized from mixed-phase cloud contains water content, which could directly affect the net LW radiative forcing.

Since mixed-phase clouds tend to be optically thicker than ice-only clouds (Sun and Shine, 1994; Shupe and Intrieri, 2004; Turner, 2005; Zuidema et al., 2005), the frequent occurrence of mixed-phase clouds has important implications for cloud radiative forcing at the surface. The presence of mixed-phase clouds relative to ice-only clouds can also have a significant impact on boundary layer structure and large-scale dynamics through the influence of cloud top radiative cooling (Morrison and Pinto, 2006).

Overall, mixed-phase clouds consist of a mixture of liquid droplets (supercooled) and ice crystals, which are highly abundant throughout the year. It also occurs as a thick single or multi-layer structure with the liquid layer mostly at the cloud top and the ice below, which is consistent with previous campaign studies conducted over the Arctic region (Zuidema et al., 2005; Shupe et al., 2006; Verlinde et al., 2007; Boer et al., 2009). The liquid layer on top of the mixed-phase cloud has a significant influence on the surface radiative fluxes, and therefore it is crucial to develop a consolidating theoretical classification of different types of mixed-phase clouds.
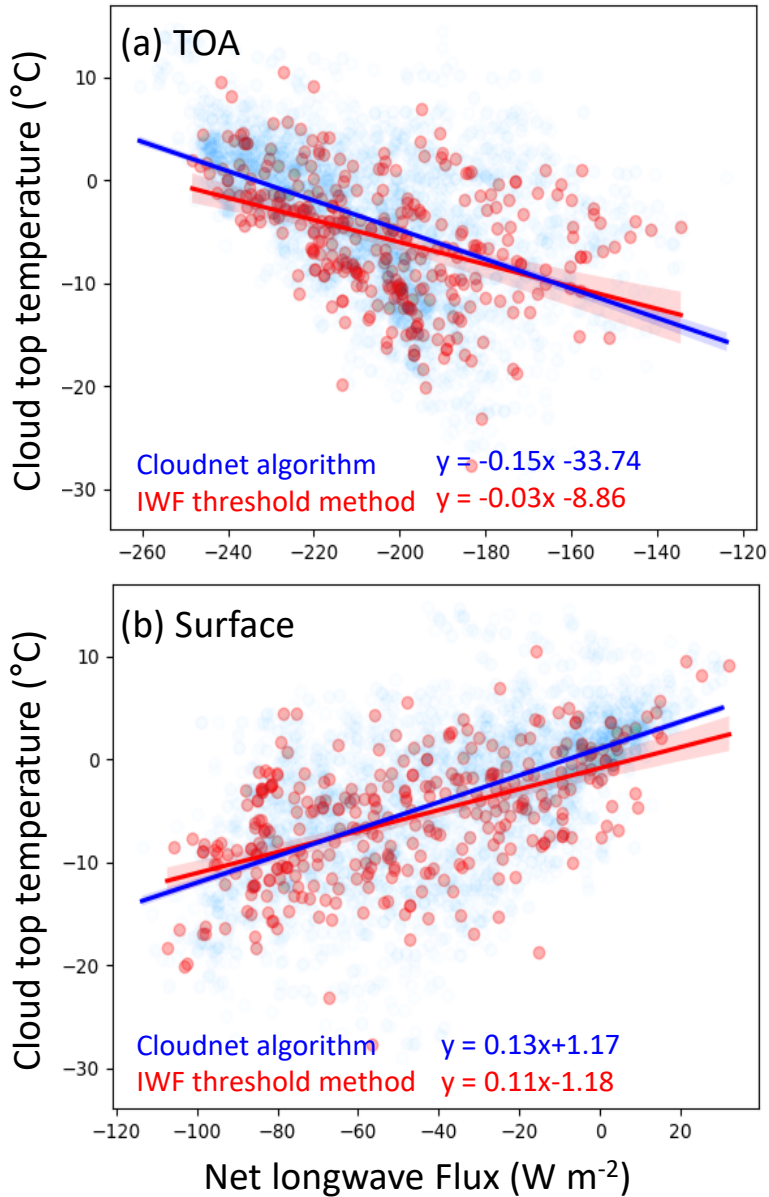
Figure 14. Comparison of cloud top temperature for net longwave radiation at the (a) top of the atmosphere and the (b) surface using Cloudnet algorithm (blue) and IWF threshold method (red) to classify mixed-phase clouds.

Chapter 4. Arctic mixed-phase clouds: comparison between observation and model

The influence of Arctic clouds on surface temperature and sea ice and snow melt is significant, mainly through the modulation of downward longwave and shortwave radiation (Urrego-Blanco et al., 2019; Yeo et al., 2022). Numerous studies have investigated Arctic cloud properties and their associated radiative effects using global and regional-scale simulation models, with a focus on cloud-radiative feedback between boundary layer clouds, near-surface temperature, and sea ice melt (Serreze and Barry, 2011; Morrison et al., 2015; Lelli et al., 2022). However, accurate simulation of Arctic cloud properties remains challenging due to the complex nature of cloud microphysical processes (Vavrus et al., 2008; Klein et al., 2009; Barton et al., 2012; Boer et al., 2012; Sotiropoulou et al., 2021; Shaw et al., 2022) and, as mentioned in the previous chapter, the complex properties of mixed-phase clouds.

Parameterizing cloud microphysical properties and validating models is challenging due to the limited availability of in situ and remote sensing observations of Arctic cloud properties (Kay et al., 2016; Boisvert et al., 2018). Various schemes for cloud microphysics have been developed to represent clouds, and their radiative effects, including the processes of hydrometeor formation, growth, and deposition (Seiki et al.,

45

2022; Zhou et al., 2022), but differences in the treatment of these microphysical processes introduce uncertainties in cloud-radiative interactions (Voigt et al., 2019; Sedlar et al., 2020). Previous studies have highlighted significant differences in the simulated geometric properties (e.g., cloud amount and height) and microphysical properties (e.g., cloud phases, droplet size, and hydrometeor shapes) of clouds over mid-latitude and tropical regions when different cloud microphysical schemes are used in climate models (English et al., 2014; Park et al., 2014; Silber et al., 2018). Cloud microphysics parameterizations have traditionally been developed for tropical and mid-latitude clouds and have not been extensively validated for Arctic clouds due to a lack of field observations (Nguyen et al., 2022). Although cloud microphysics schemes have been evaluated in the context of several Arctic field experiments (**Table 1**), simulations of Arctic cloud microphysical properties have generally shown significant discrepancies when compared to ground-based and airborne observations (Walsh et al., 2002; Kretzschmar et al., 2020). Several recent studies have also investigated the sensitivity of cloud microphysical schemes in regional-scale forecasts using the Weather Research and Forecasting (WRF) model over polar regions (Hines and Bromwich, 2008, 2017; Wilson et al., 2012; Seo and Yang, 2013; Bromwich et al., 2016; Kim et al., 2022).

However, the performance differences of models using different cloud microphysics schemes specifically for Arctic summer clouds have not been investigated. While version 4.1.1 of the WRF model, optimized for the Antarctic environment, has been developed for Polar-optimized WRF (PWRF), it has not been optimized for the Arctic (Hines et al., 2021). Therefore, a comprehensive evaluation of the performance of the cloud microphysics schemes included in version 4.1.1 of the PWRF model is required to represent Arctic cloud properties accurately.

This chapter aims to evaluate the microphysical properties of Arctic low-level clouds simulated by four commonly used cloud microphysics schemes included in the PWRF. The model simulations using these four schemes were validated against comprehensive in-situ airborne observations collected over Svalbard during the ACLOUD campaign, conducted from May to June 2017. In addition, to assess the variations in simulated Arctic low-level cloud properties under the different schemes, the differences in microphysical parameterizations will be analyzed.

Table 1. Previous field campaigns to study the Arctic clouds.

Campaign	Goals	Reference
Surface Heat Budget of the Arctic Ocean (SHEBA)	Evaluation of regional climate models on Arctic cloud and radiation processes	Intrieri et al. (2002) Wyser et al. (2008)
Norwegian Young sea-ICE Campaign (N-ICE2015)	Evaluation of ERA-Interim simulations on cloud properties	Graham et al. (2016)
Arctic Summer Cloud-Ocean Study (ASCOS)	Evaluate the performance of atmospheric reanalyses and global climate models in the simulation of the high Arctic environment	Tjernström et al. (2014) Boer et al. (2014)

4.1 Meteorological contexts during the ACLOUD campaign

During the ACLOUD campaign from 2-20 June 2017, low-level clouds were observed over Svalbard in warm air above both sea ice and the open ocean. A total of seven flights were conducted to record these cloud formations. **Figure 15** shows the spatial distribution of synoptic weather patterns, CF, and daily air mass back trajectories during the study period. The sea level pressure pattern (**Figure 15a**) showed distinct high and low pressure systems, resulting in a predominant advection of air masses from the Arctic pole towards the airborne observation areas near Svalbard (**Figure 15b**). The 5-day back trajectories, computed using the Hybrid Single-Particle Lagrangian Integrated Trajectory (HYSPLIT) with NCEP meteorological data from each flight altitude, showed the transport of air masses from the sea ice region into the open ocean, passing through a transition zone over the GIN Sea to Ny-Ålesund. The air masses experienced relatively warm near-surface temperatures (4°C) (**Figure 14c**). It appears that the air masses were heated by adiabatic motions and sensible/latent heat fluxes during their journey, resulting in a high cloud fraction over the flight area (Knudsen et al., 2018).

Under different meteorological conditions, cloud properties can vary. About 30-50% of low-level liquid clouds are observed over Greenland under the surface melting conditions (Shupe et al., 2011, 2013; Cesana et al., 2012; Bennartz et al., 2013). On the other hand, ice clouds are mainly formed by warm and moist air masses moving across the open ocean (specifically the Kara, Barents, and GIN Seas) from the Kara Sea to Svalbard (Ding et al., 2017; Graversen et al., 2011; Lee et al., 2017). It appears that a significant number of clouds are generated in the transition zone, with 81% of cloud-generating air masses passing through the transition between sea ice and the open ocean (**Figures 14b and 14c**). Mioche et al. (2017) suggested that the frequent occurrence of riming and diffusive growth leads to the generation of a significant amount of both liquid and ice crystals over the transition zone.
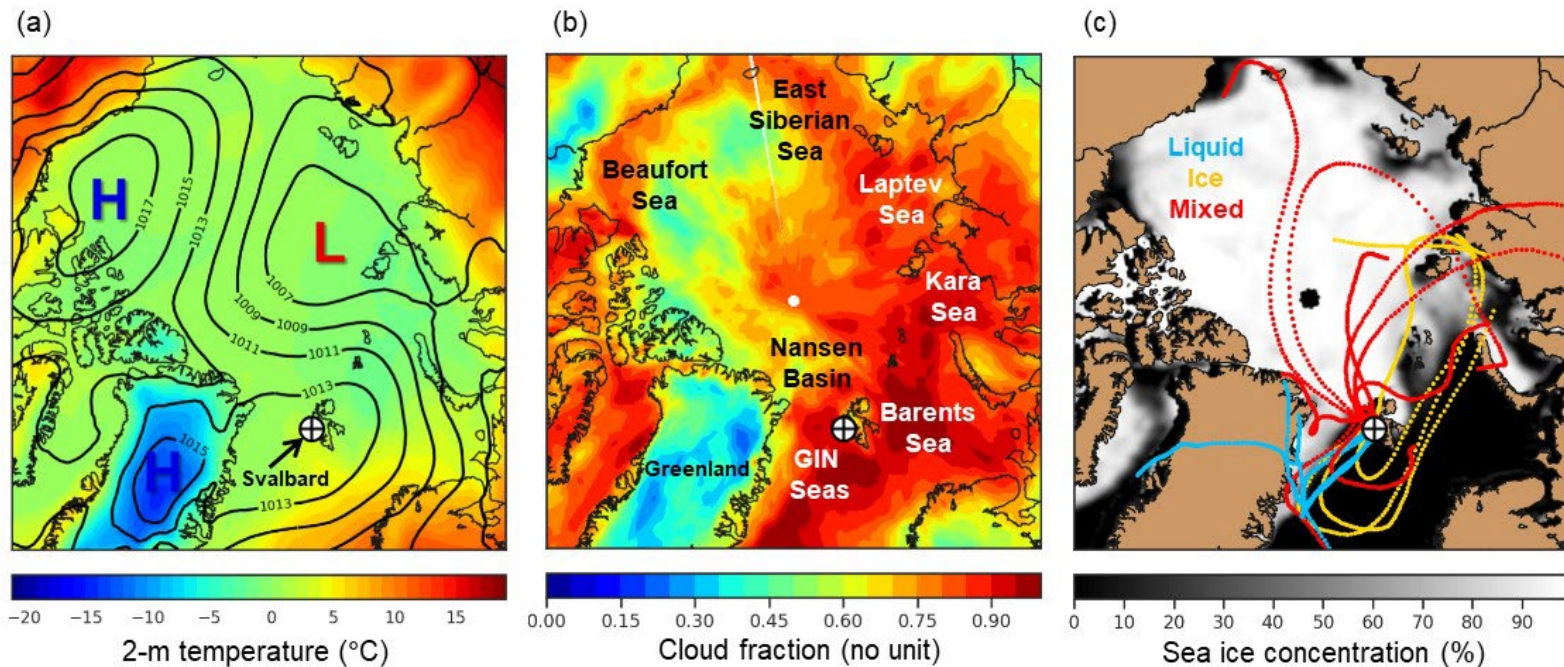
Figure 15. (a) Sea level pressure (in hPa; line) with 2-hPa contour interval and 2-m temperature (in °C; shading) using ERA5 reanalysis, (b) MODIS cloud fraction (shading) using MODIS-Aqua cloud mask, and (c) daily air mass backward trajectories from NOAA ARL Hybrid Single-Particle Lagrangian Integrated Trajectory (HYSPLIT) for each cloud phase (liquid, blue; ice, yellow; mixed, red). The shading in (c) represents the average sea ice concentration using NIMBUS-7 from May 29, 2017, to June 23, 2017.

Figure 16 shows the vertical distributions of LWC, IWC, and temperature measured during the ACLOUD campaign period, together with the probability density function (PDF) of the kernel density estimate (KDE). KDE is a non-parametric method used to estimate the PDF of variables by assigning weights to the kernels. The LWC in liquid clouds is below 0.6 g m^{-3} and is mainly observed below 1.2 km, with the PDF peaking at about 0.5 km at relatively warm temperatures (-3.8±0.2°C; **Figures 15a and 15c**). On the other hand, the PDF of LWC in mixed-phase clouds had a wide distribution and decreased exponentially above 0.8 g m^{-3} at all flight altitudes.

The majority of the IWC recorded from airborne CIP measurements during the ACLOUD campaign is below 0.1 g m^{-3} (**Figure 15b**). The IWC in ice clouds is mainly observed below 0.5 km within a temperature range of -12 to 3°C, with the PDF showing a slight peak at 3 km altitude. However, the IWC in mixed-phase clouds is observed at all flight altitudes.
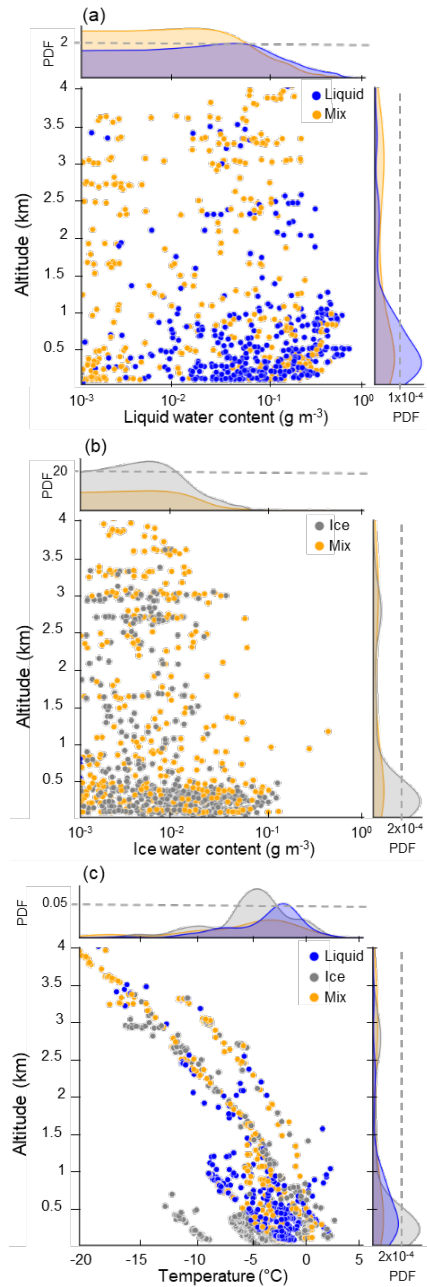
Figure 16. Vertical distributions of (a) liquid water content, (b) ice water content, and (c) temperature for liquid (blue), ice (grey), and mixed-phase clouds (yellow). The top and right panels show the kernel density estimate of the probability distribution function (PDF) for each variable.

4.2 Cloud microphysical properties: Observation vs. model

To efficiently handle computational complexity and reduce time constraints, this study uses the most accurate 4D interpolation method to co-locate trajectory observations (in seconds) with simulation time (in minutes). This method simplifies the process and avoids the need for complex and computationally intensive interpolation techniques such as polynomial, bicubic, spline, and kriging. The model simulation maps atmospheric parameter values onto a 4D grid, with latitude, longitude, altitude, and time (at 1-minute intervals) as the four axes. This grid is then aligned with the ACLOUD flight observations, which occur every second. It should be noted that the PWRF simulation calculates LWC values using the liquid mixing ratio. For ice, snow, and graupel mixing ratios in the model simulations, the corresponding IWC values are calculated for comparison with ACLOUD flight observations. This approach is consistent with the IWC derivation method used in the ACLOUD observations, where all particles in the 75-1550 µm size range are considered to be ice crystals.

Figure 17 shows the spatial distribution of temperature, LWC, and IWC based on airborne observations and simulations from four cloud microphysics schemes. The research flights were conducted during the ACLOUD campaign over both sea ice and open ocean regions, including the transition zone between them. In this study, the transition zone is defined as the area with a sea ice concentration of 15%. Previous studies have shown that lower sea ice concentrations absorb more solar radiation from the sea surface, leading to increased ocean warming and cloud formation through increased moisture transport to the atmosphere (Barton et al., 2012; Palm et al., 2010). However, there is no statistically significant difference between airborne LWC measurements over sea ice (0.14 g m^{-3}) and those over the open ocean (0.13 g m^{-3}). A similar trend is observed in the simulations of the four schemes (sea ice vs. open ocean): Morrison, 0.0091 g m^{-3} vs. 0.0075 g m^{-3}; WDM6, 0.0108 g m^{-3} vs. 0.0034 g m^{-3}; NSSL, 0.0099 g m^{-3} vs. 0.0052 g m^{-3}; and P3, 0.0099 g m^{-3} vs. 0.0065 g m^{-3}. The observed IWC over sea ice (0.024±0.042 g m^{-3}) is slightly higher than that over the open ocean (0.016±0.040 g m^{-3}), but the difference between model simulations and observations for IWC is similar to that for LWC.
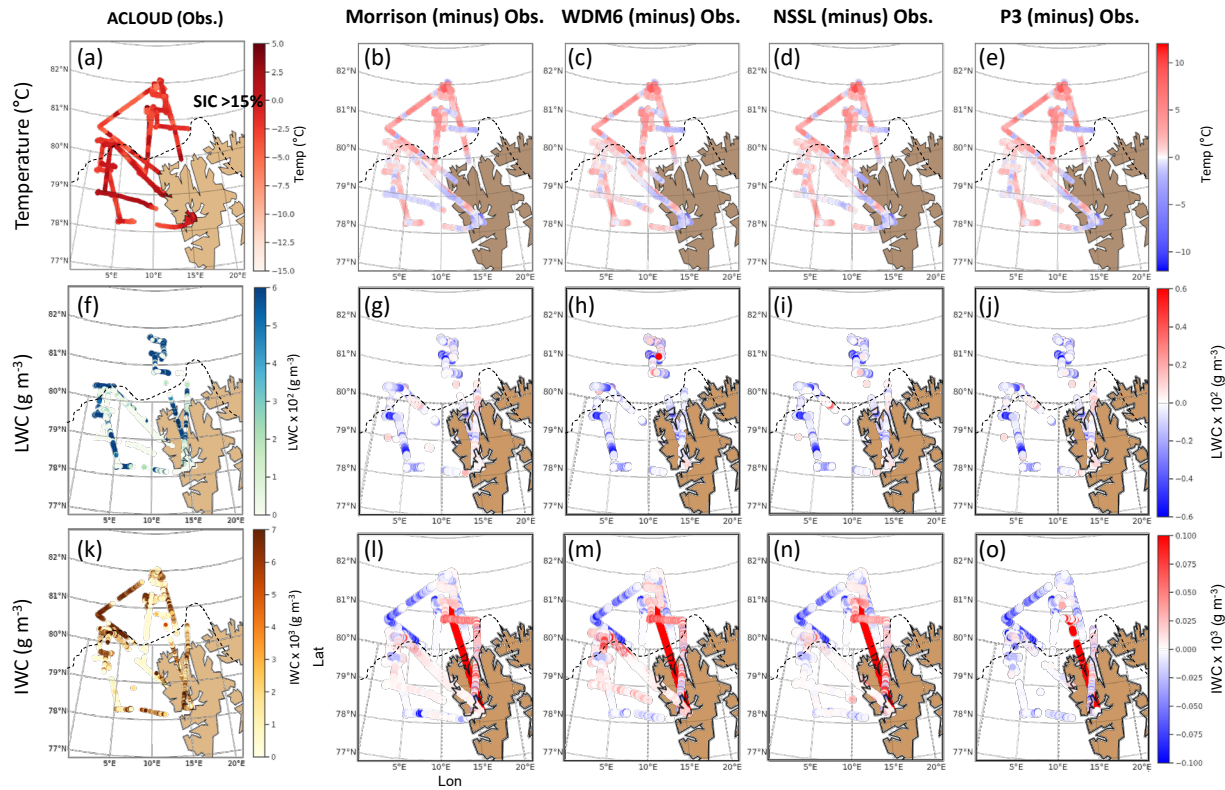
Figure 17. Spatial distribution of observations (a,f, and k) and the difference between model simulations of (b-e) temperature, (g-j) liquid water content, and (i-o) ice water content. The dashed line indicates the 15% ice cover averaged over the study period.

The variations in IWC simulations among the four schemes were not as pronounced as those observed for LWC. However, for the 14 July flight, all four systems significantly overestimated IWC (**Figure 17**). These overestimations are thought to be due to the observed temperature (-20~-15°C) at an altitude of about 3.5 km, which caused a discrepancy between observations and simulations in the amount of ice crystals.
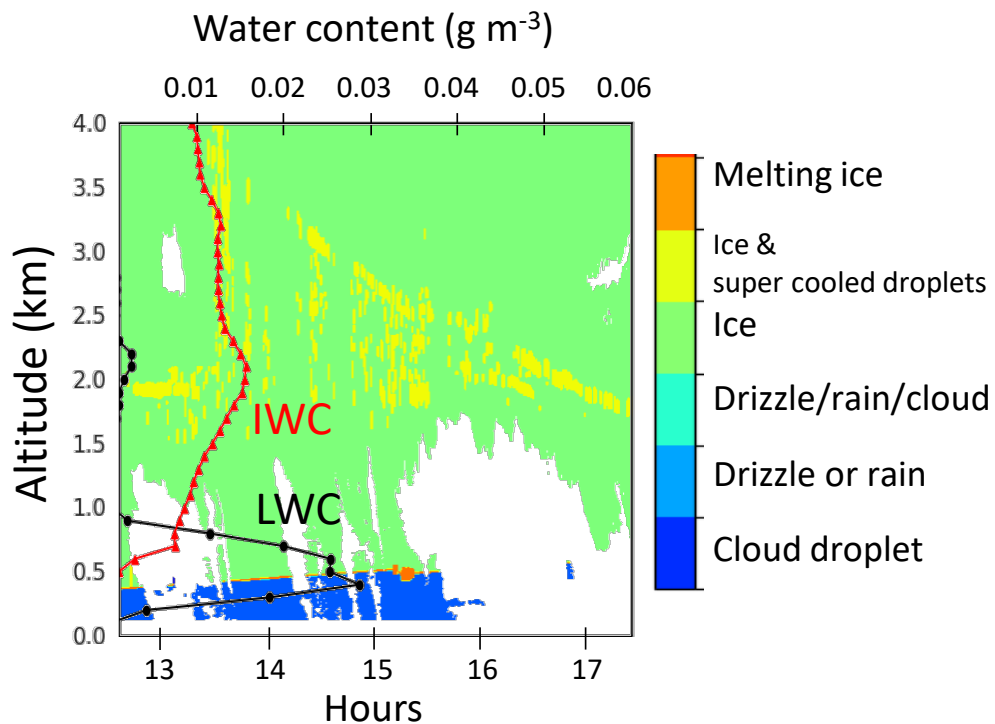
Figure 18. Cloud classification (contour), liquid water content (black), and ice water content (red) from 12:30 to 17:30 on 14 June 2017.

The cloud classification, LWC, and IWC observed by Cloudnet during the ACLOUD campaign can be seen in **Figure 18**. The averaged LWC and IWC from 12:30 to 17:30 on 14 June 2017, show the presence of cloud droplets and drizzle or rain from 0 km to 0.5 km altitude. The LWC in this case is concentrated below 1 km and mixed-phase clouds with ice and supercooled droplets near 2 km.

For the 14-day case where the IWC was overestimated, Cloudnet's cloud classification, rainfall rate, backscatter coefficient, liquid water path and radar reflectivity factor were analyzed (**Figure 19**). The case 10:00 (UTC) 14 June 2017, when the clouds started to arrive, the radar reflectivity factor shows the cloud shape up to a height of about 6 km, and the backscatter coefficient shows the height at which ice particles are observed in the clouds at about 2 km. The base height of the cloud is about 1 km, and drizzle, or rain is observed below.
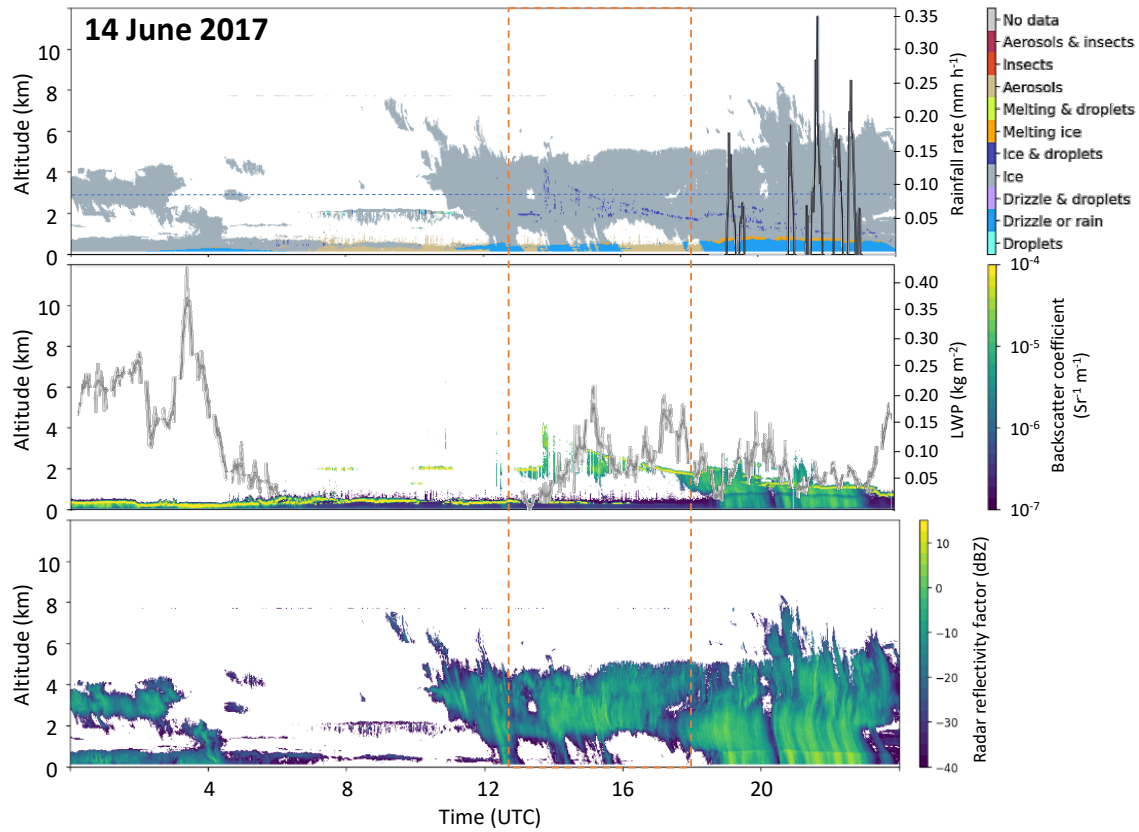
Figure 19. Time series of cloud classification, rainfall rate, backscatter coefficient, liquid water path, and radar reflectivity factor for the period on 14 June 2017.

Especially, a large amount of rainfall rate was observed after 18:00 (UTC). For an indication of how well the PWRF model reproduces the arrival times of the clouds, the simulated CF for each scheme was compared (**Figure 20**). Overall, the four cloud microphysics schemes show a delay in cloud formation of about 3 hours. For the Morrison scheme, the clouds formed in the upper layers and then decreased, with the amount of cloud fraction simulated in the WDM6 P3 NSSL order being distributed to higher layers over time. All schemes under-simulated the LWC for the day (**Figure 17**), and when looking at the LWC time series for each scheme, it appears that they are not simulating the LWC at all for this time.

For the IWC, all schemes overestimate (**Figure 21**), where the observed IWC shows a continuous ice and mixed-phase cloud above 1 km. The model simulated IWC does not capture the actual cloud pattern. Looking at the LWC and IWC of the observations and each scheme by height (**Figure 22**), the large amount of LWC seen in the observations is not simulated. To determine whether precipitation was misclassified in the observations, precipitation was examined (**Figure 23**).

It was found that the liquid water content has properties that are independent of precipitation and are present in mixed-phase clouds. It can be seen that the Morrison scheme has the smallest error in the actual amount of precipitation, while the other three schemes calculate significantly more precipitation. IWC simulates a large number of values above 2 km.
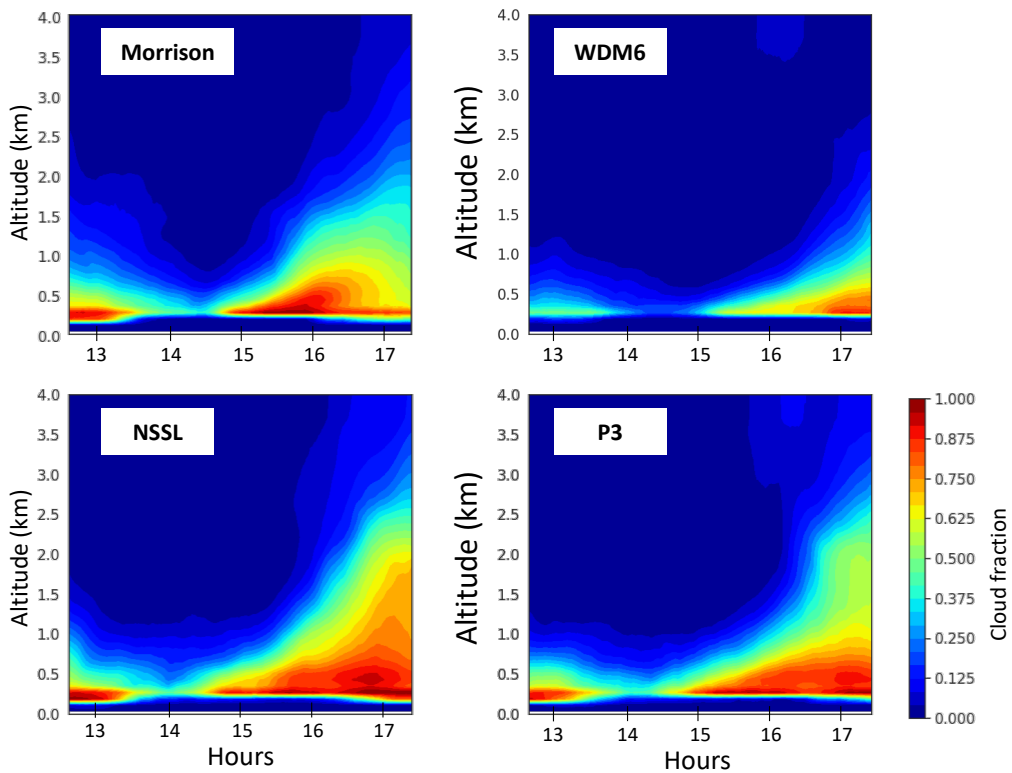
Figure 20. Cloud fraction on 14 June 2017 for each cloud microphysics scheme.

As can be seen in **Figure 21**, it takes time for the ice-bearing cloud to form, and once the ice is triggered, it is simulated with a higher water content than the observed amount of ice crystals. Given these findings, it appears that the IWC overestimation from all four cloud microphysics schemes for this date case is due to a delay of about 3 hours of cloud formation, but the ice initiators gave a significantly higher value of ice than the actual observations, simulating an ice cloud rather than a mixed-phase cloud.

Figure 25 shows the vertical profiles of observed and simulated LWC, IWC, and temperature. The bias and root mean square error (RMSE) of LWC and IWC between observations and simulations for different cloud phases are listed in **Table 2**. The simulated LWC showed a smaller bias (<0.1 g m^{-3}) at altitudes between 0.5 and 1 km, but a significant discrepancy with a bias of up to 10^{-2} g m^{-3} is observed at altitudes above 1 km. The IWC bias of the mixed-phase cloud ranged from -0.009 to -0.017 g m^{-3}, which is lower than that of the ice cloud (-0.016 to -0.019 g m^{-3}; **Table 2**). The NSSL scheme showed a small bias for both mixed phase (-0.009 g m^{-3}) and ice (-0.016 g m^{-3}) clouds, but with a large RMSE (0.087 for mixed phase and 0.067 for ice clouds).
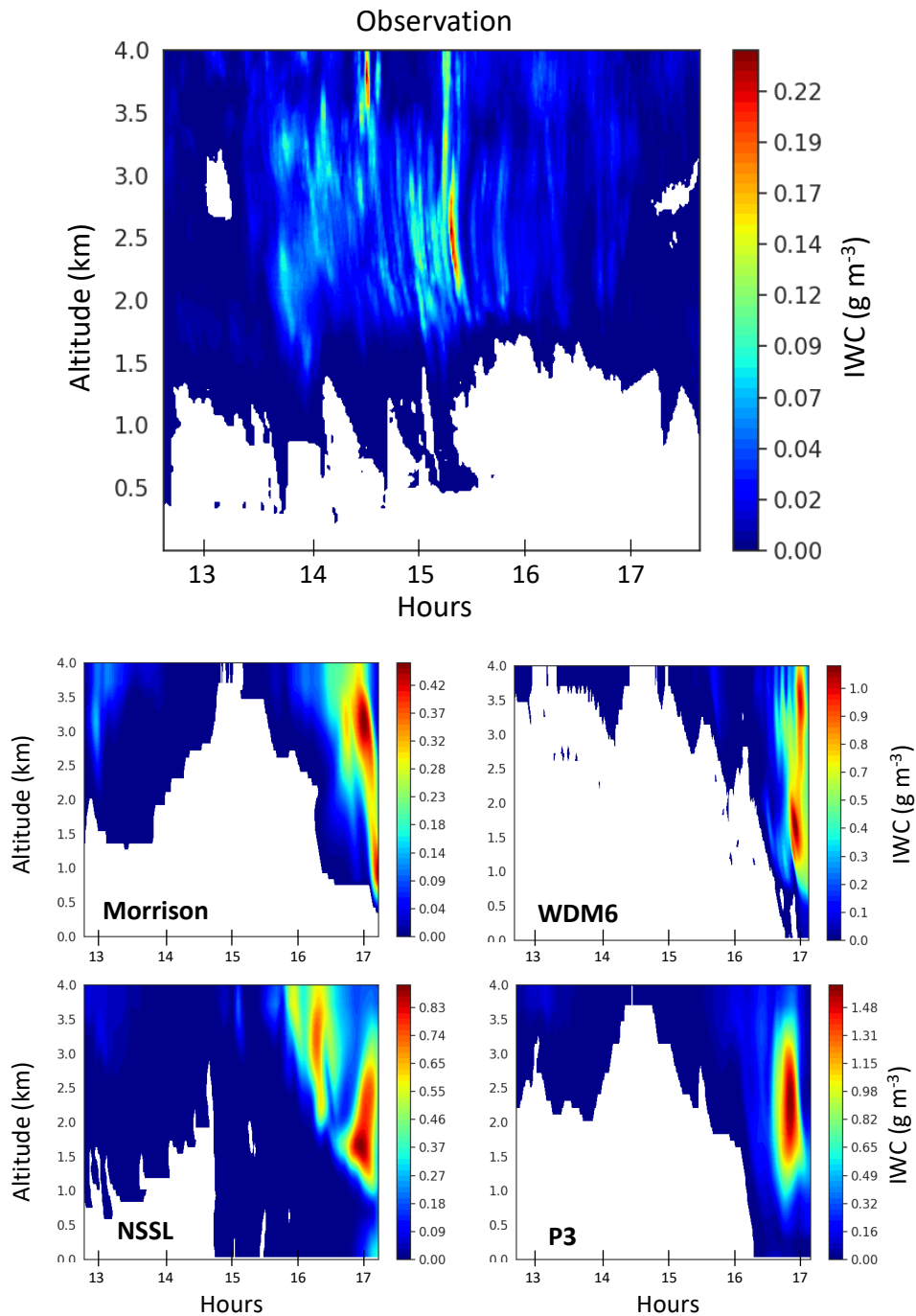
Figure 21. Ice water content on 14 June 2017 for observation and four microphysics schemes.

The comparison of the temperature profiles is shown in **Figure 24c**. There is no significant discrepancy between the models. The models tend to overestimate the temperature below 1 km and underestimate it above 1.5 km. This bias can be attributed to the planetary boundary layer (PBL) scheme in the PWRF model. Under weak surface winds and stable stratification in the Arctic region, the local PBL scheme (MYNN 2.5) performs better in predicting surface temperature (Dong et al., 2018), but it still shows a slight overestimation. Furthermore, at altitudes above 1 km with higher wind speeds, the intensity of turbulence, which is directly influenced by the PBL parameterization scheme, can affect the temperature under similar stability conditions, leading to an underestimation of temperature (Battisti et al., 2017).

Temperature plays a crucial role in simulating IWC, and its impact on IWC bias is considered more significant than on LWC bias. The MYNN2 PBL scheme (Holt and Raman, 1988) is employed to model a low-level cloud, which parameterizes boundary layers and surface properties such as turbulent vertical flux, moisture, and temperature.
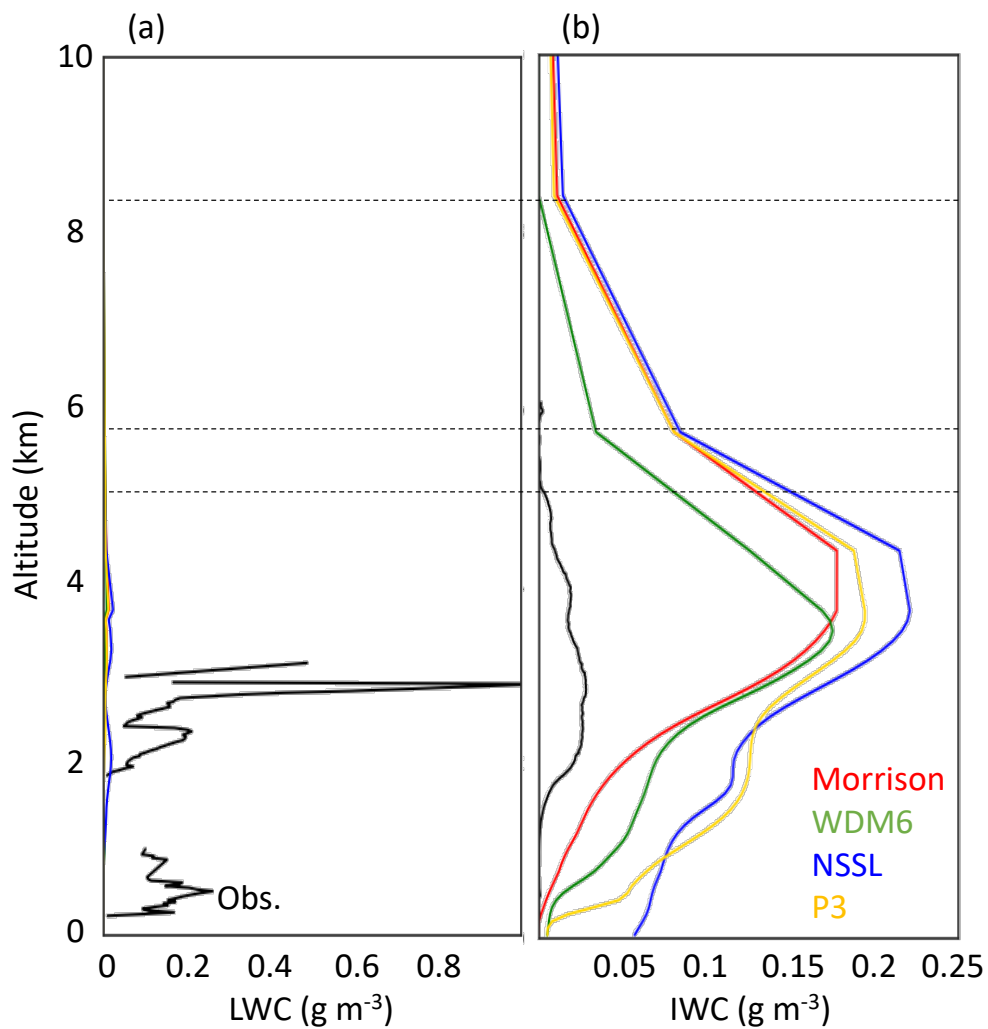
Figure 22. Vertical distribution of (a) LWC and (b) IWC for Cloudnet observation and model simulations (Morrison scheme, red; WDM6 scheme, green; NSSL scheme, blue; P3 scheme, yellow). The data cover the period from 12:30 to 17:30 on 14 June 2017.

Kilpeläinen et al. (2012) observed that different PBL schemes (Mellor-Yamada-Janjic, Yonsei University, Quasi-Normal Scale Elimination) used in PWRF yielded varying results due to differences in excessive mixing within the PBL and shortcomings in representing the surface energy balance. However, an overall warm bias is detected, particularly near the surface. Consequently, the PBL schemes can generate temperature profiles that underestimate temperature inversion and depth, which can influence the temperature thresholds for ice crystal formation.
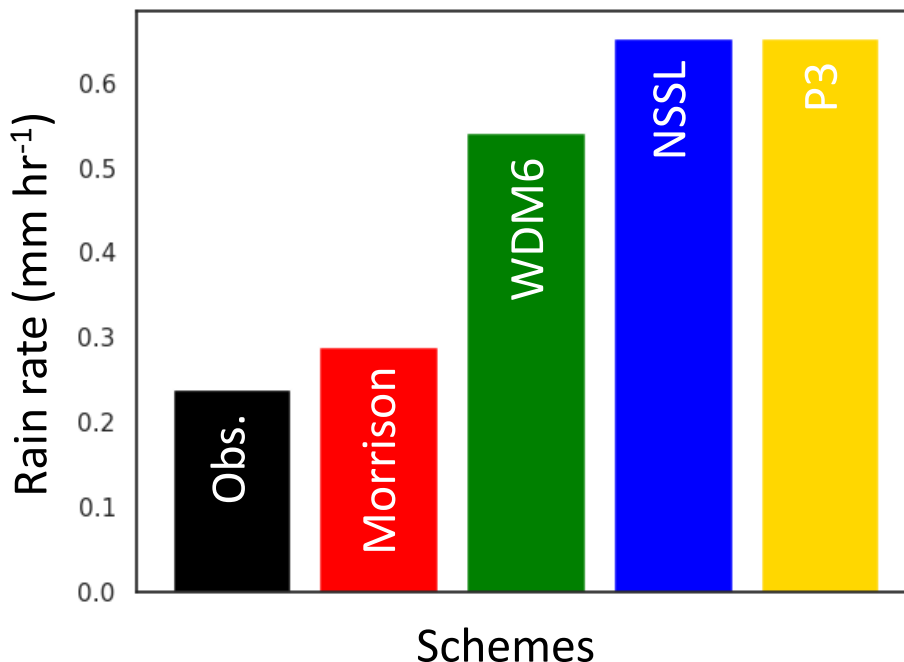
Figure 23. Rainfall rate for each scheme simulation during the period from 12:30 to 17:30 on 14 June 2017.
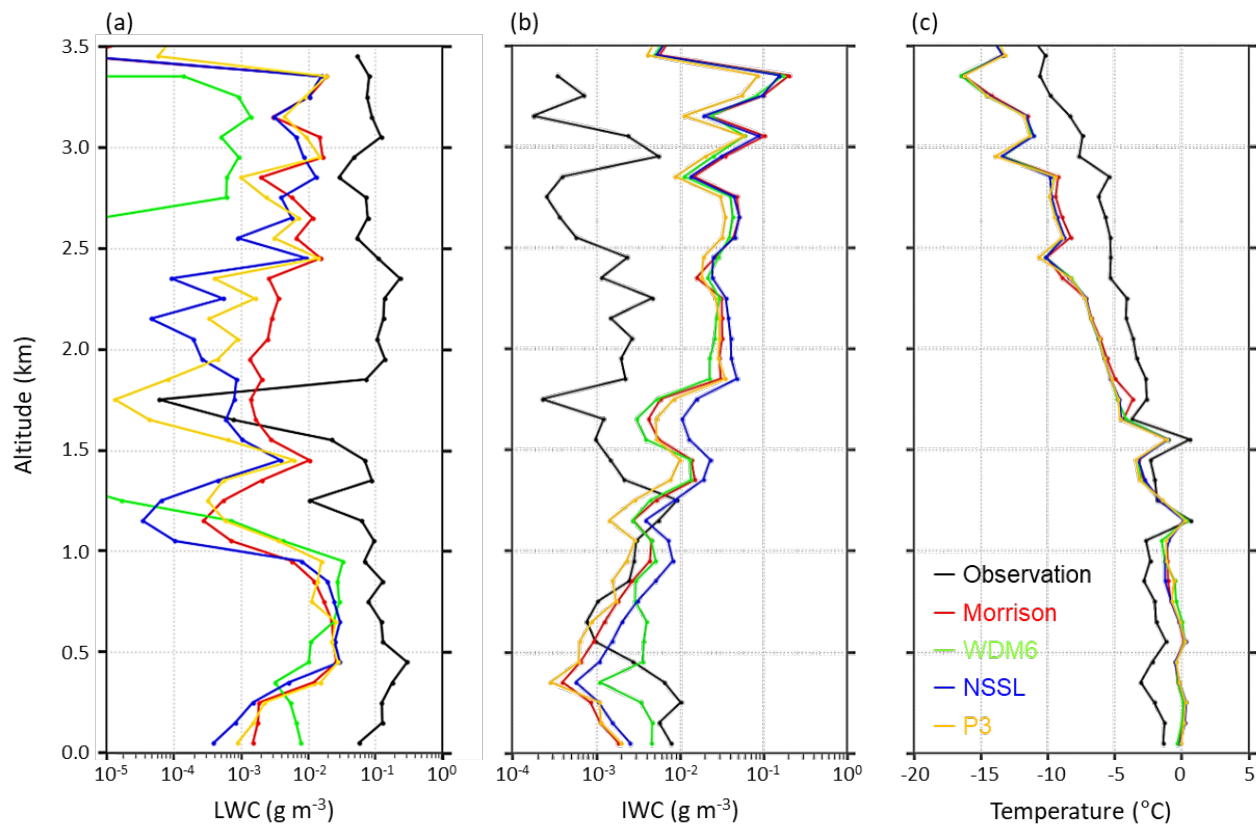
Figure 24. PWRF-model-simulated and the ACLOUD-observed profiles of (a) liquid water content, (b) ice water content, and (c) temperature.

Simulating mixed-phase clouds has been reported to be challenging due to the involvement of supercooled water droplets. The presence of supercooled water droplets can be identified using various methods (Zhang et al., 2020; Luke et al., 2021; Yang et al., 2021). For instance, high content of supercooled water droplets is observed when high LWC and low IWC values are present at temperatures below 0°C. A similar pattern is observed in the study where a mixed-phase cloud had a substantial amount of supercooled water content, contributing significantly to the IWC bias. In this study, the continuous variables of LWC and IWC are evaluated by bias and RMSE methods in the PWRF simulations.

So far, the performance of PWRF model on the ACLOUD campaign dates were only evaluated. The goal of this study is to extend this to look at how much difference there is in the amount of cloud observed when the model is run for a year.

The cloud fraction, calculated in PWRF using five different microphysical schemes, is defined as the fractional cloudiness of each pixel grid. For comparison and contrast, the Morrison scheme is chosen as the default scheme as it is modified for the Arctic environment and is recommended when using PWRF (Hines and Bromwich, 2017).

Table 2. Bias and RMSE in the liquid water content and ice water content for each liquid, ice, and mixed-phase layers between PWRF cloud microphysics schemes and ACLOUD observations.

		Bias (g m^{-3})				RMSE (g m^{-3})			
Schemes		Morrison	WDM6	NSSL	P3	Morrison	WDM6	NSSL	P3
Mixed	LWC	-0.044	-0.062	-0.060	-0.045	0.091	0.100	0.100	0.093
	IWC	-0.017	-0.014	-0.009	-0.016	0.113	0.073	0.087	0.071
Liquid	LWC	-0.121	-0.131	-0.126	-0.124	0.192	0.204	0.192	0.192
Ice	IWC	-0.016	-0.019	-0.016	-0.018	0.073	0.057	0.067	0.059

Figure 25 shows the annual average of column CF (from surface to 12 km). WDM6 underestimates the CF compared to the Morrison scheme, especially in the Arctic region. Although MILB, THOM, and NSSL are in good agreement with Morrison, there is an underestimation of about 0.04 in the Nansen Basin and an overestimation in the Canada Basin, Central Arctic, and the Laptev Sea.

The vertical distribution of CF over the Arctic region (70-83°N) is shown in **Figure 26**. The Arctic region (70-83°N) was chosen because of evaluation problems when using limited satellite observations up to 82.5°N, such as Cloud and Aerosol Lidar with Orthogonal Polarization (CALIOP) aboard the Cloud-Aerosol Lidar and Infrared Pathfinder Satellite Observation (CALIPSO Liu et al., 2009) and Cloudsat (Marchand et al., 2008). In general, CF increased during the winter season, which is similar to other studies. WDM6 underestimated low-level clouds during most of the season, but overestimated during summer. NSSL underestimated CF in summer, but overestimated it in winter.
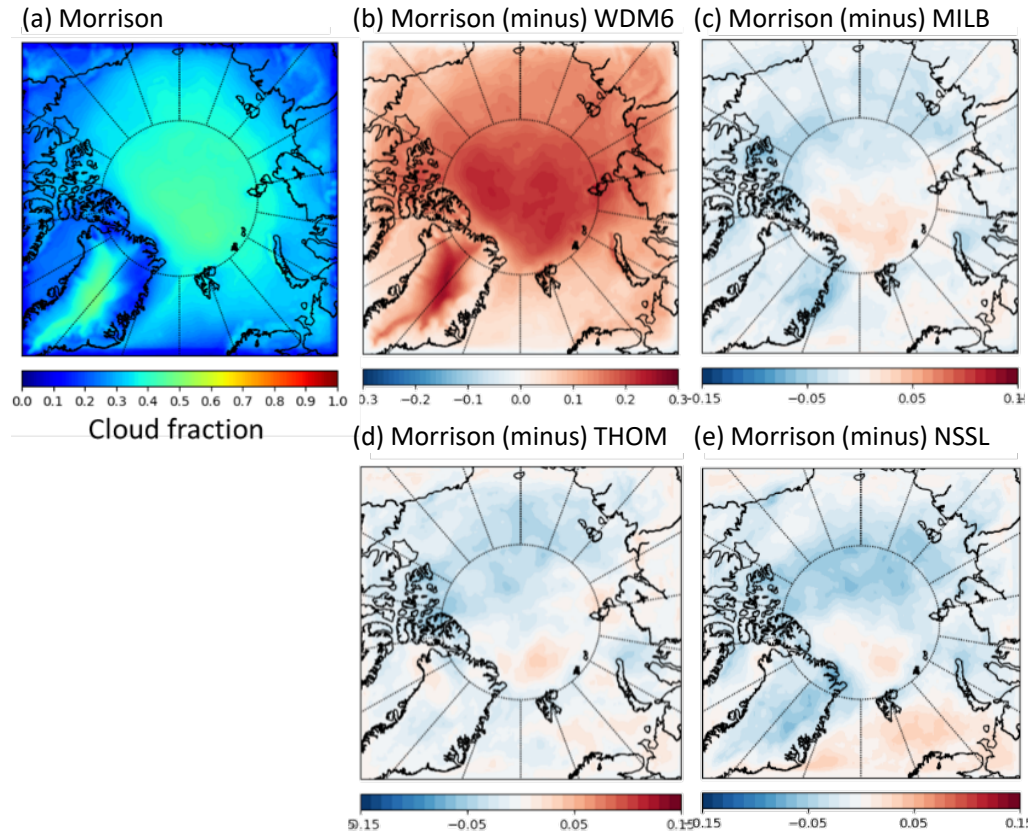
Figure 25. Spatial distributions of the year averaged (March 2008 to February 2009) cloud fraction using the MORR scheme and the associated difference from four selected schemes, given as the Morrison (minus) WDM6, MILB, THOM, and NSSL.

The discrepancy in the calculated CF is mainly due to how each scheme calculates the size distribution of particles in diameter for hydrometeor categories such as cloud water, rain, cloud ice, snow, and graupel. The model result of the area mean cloud water and cloud ice for October 2008 is shown in **Figure 27**. WDM6 underestimates the mixing ratio of cloud water, but overestimates cloud ice. This may indicate that the underestimated low-level CF of WDM6 is mainly due to the underestimated amount of cloud water. Further investigation of the individual hydrometeor process terms is required.

CALIPSO and CloudSat radar observations are used for cloud analysis over the Arctic region. To calculate CF over the Arctic region, a 2°x2° grid is created on a polar stereographic projection. The orbital data from CALIPSO and CloudSat are accumulated on each grid cell to produce a monthly average CF. Based on frequency distribution analysis, the number of data points in a grid cell was at least 50 for both CloudSat and CALIPSO for reasonable statistical accuracy. In order to limit the satellite coverage near the poles, monthly CF values are computed from 70 to 82.5°N.
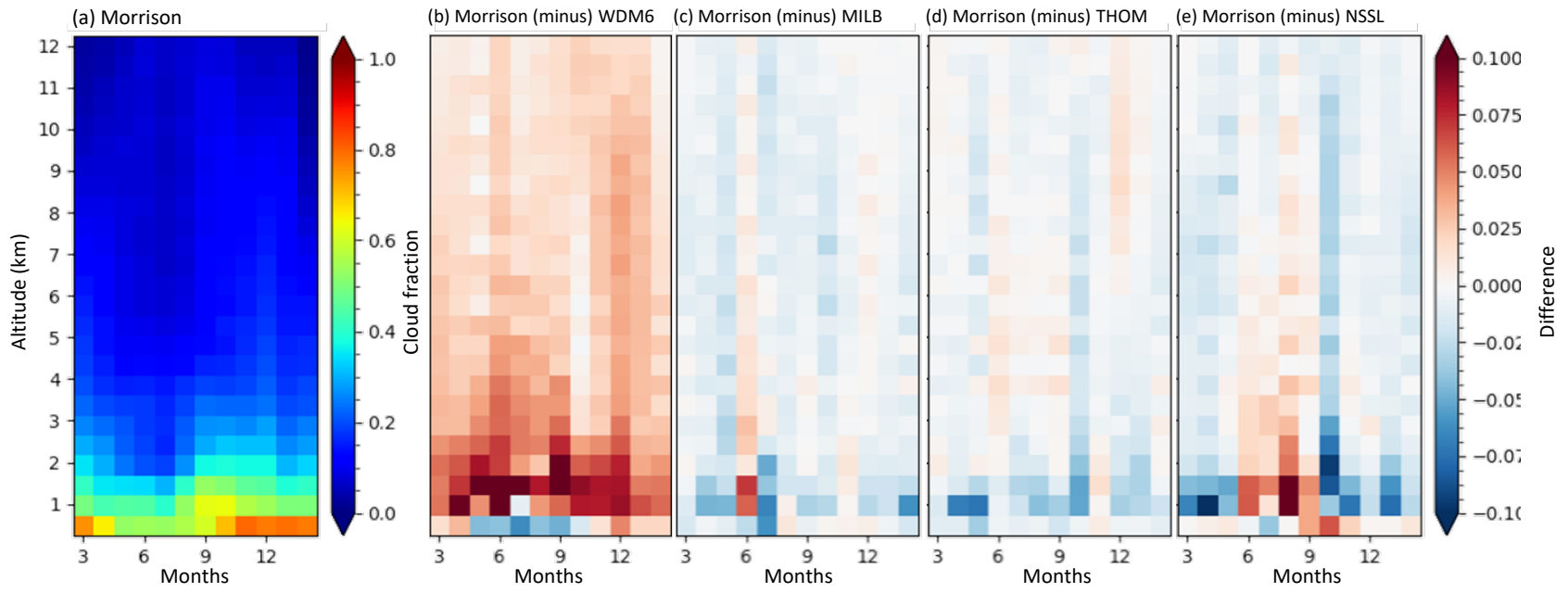
Figure 26. Vertical distribution of cloud fraction for Morrison and difference of four selected schemes, from March 2008 to February 2009 in the Arctic region (70-83°N).
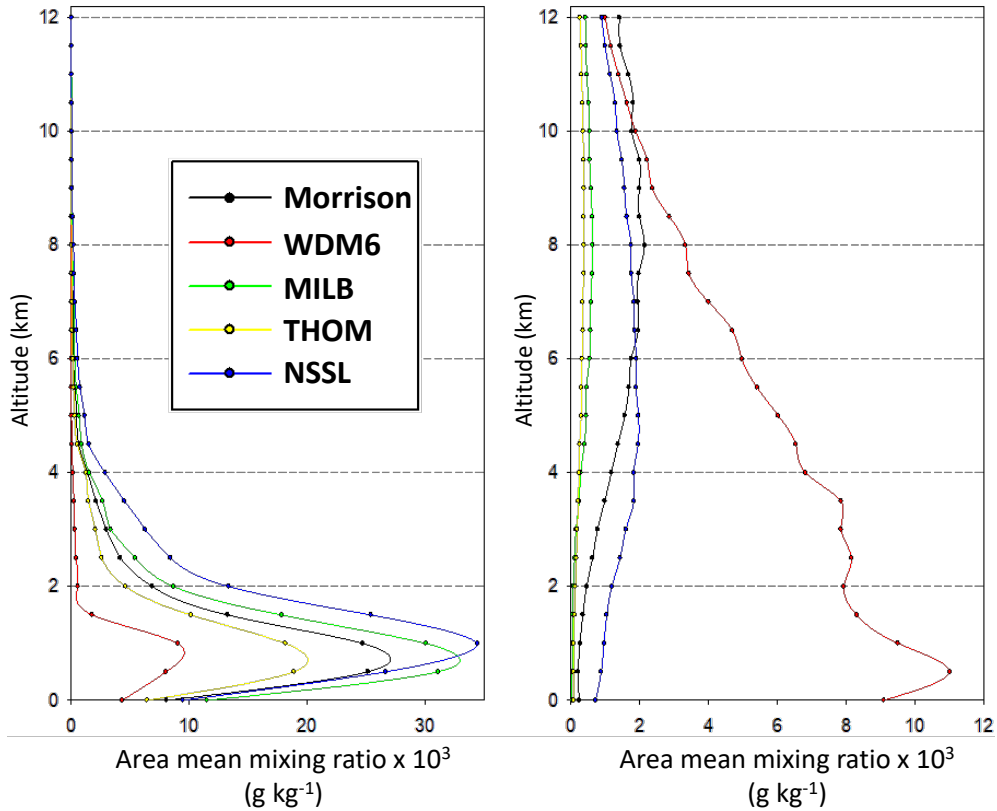
Figure 27. Area mean cloud-water and cloud-ice mixing ratio from model simulations during October 2008 over the Arctic region (70-83°N).

Annual averages of CF in the Arctic region were found to be 0.71 and 0.53 from CALIPSO and CloudSat, respectively. There is a large discrepancy between CALIPSO and CloudSat over the general area, with a cloud percentage difference of about 18%. Geometrically thin clouds with depths less than 2 km are typically missed by CloudSat observations. In particular, near-surface thin clouds (<0.3 km) over sea ice are misclassified by CALIPSO and not observed by CloudSat t (Chan and Comiso, 2013).

The cloud fraction over the GIN seas and the Barents Sea region shows the highest values of about 0.9 and 0.8 for CALIPSO and CloudSat, respectively. This is mainly due to the different geographical locations of the open ocean and sea ice. Therefore, the cloud microphysical characteristics of each geographical location should be considered when evaluating model simulations.
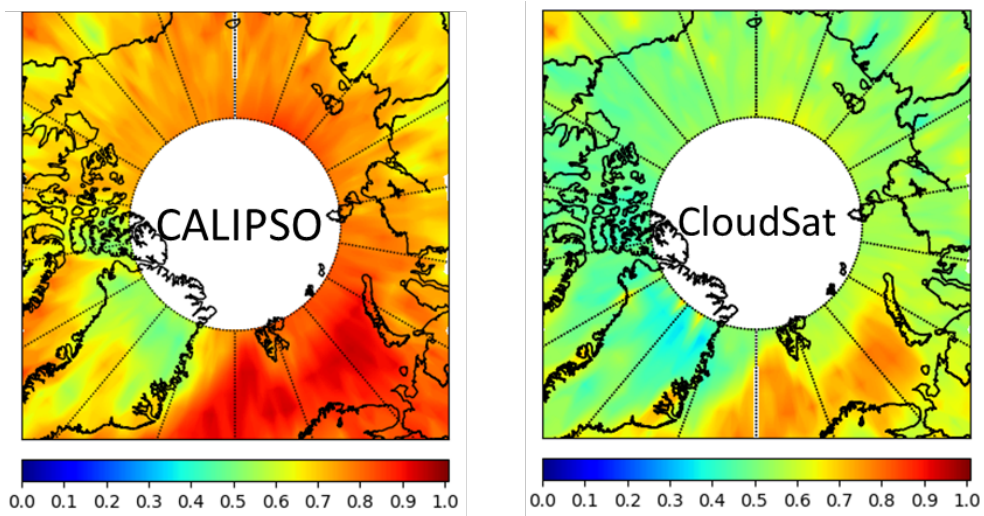
Figure 28. CALIPSO and CloudSat-based cloud fraction on the merged cloud mask product on a 2°x2° grid from March 2008 to February 2009.

A case study approach has been used in previous studies of clouds to compare observations of clouds with models. However, it requires the analysis of many cases to compare them. The lidar signal must not be attenuated by low clouds in order to detect the liquid layer inside clouds.

A measure of the liquid water path is also needed to determine the liquid water content within the cloud. This is provided by measurements made by microwave radiometers. The CALIPSO cloud phase retrieval algorithm can be used to evaluate clouds in the Polar WRF model. CALIPSO uses lidar profiles to detect clouds every 333 m with a vertical resolution of 480 m. Cloud pixels are classified as liquid, ice-dominated, and undefined using the polarisation state of laser light scattered by cloud particles and the temperature. The final product is averaged over a 2°x2° grid to produce monthly, global, three-dimensional CF (Chepfer et al., 2010; Cesana et al., 2012). CALIPSO observations can be used to assess Arctic cloud occurrence and vertical structure and to simulate Arctic cloud phase and surface radiative fluxes.

A number of days can be selected if they contain long-lived liquid layer clouds and at times when the CALIPSO path is over the Arctic region. Satellite exchanges with multiple liquid or mixed-phase cloud layers will be excluded, as the liquid water content of each layer cannot be retrieved. Removing contaminated datasets provides more useful information than a case study. However, it is not sufficient for a complete climatological study.

4.3 Theoretical analysis of scheme algorithm

To assess the occurrence of clouds, measured as a binary event (presence or absence), the WMO/WWRP (2012) scoring method followed, using frequency bias (FB) and log odds ratio values. It is important to note that clouds are only considered present if the cloud phase can be distinguished by its amount in the model simulations. The FB score is calculated by dividing the total number of predicted cloud occurrences by the total number of observed cloud occurrences (defined by $\alpha+\beta$ and $\alpha+\kappa$, respectively) (Mittermaier, 2012).

$$FB = \frac{\alpha+\beta}{\alpha+\kappa} \, , \tag{1}$$

where α is when cloud occurrence is reported by both model and observations, β is when the model produces clouds that are not detected by observations, and κ is when observations detect clouds that are not simulated by the model. The FB value of 1 indicates a perfect model, while a value greater or less than 1 represents an over- or under-predicted cloud occurrence, respectively.

The log-odds ratio, which is the natural logarithm of the odds ratio quantifying the strength of the relationship between two variables, is employed to validate FB metrics (Hogan et al., 2009).

$$\ln\theta = \ln\left(\frac{\alpha v}{\beta\kappa}\right) \, , \tag{2}$$

where v indicates no clouds based on both model and observations. The logarithm of correctly predicted cloud events (αv) is divided by the product of incorrectly predicted cloud events ($\beta \kappa$). A higher log-odds ratio indicates a more accurate prediction by the model.

Figure 29 shows the FB and log-odds ratio values representing cloud occurrence based on four cloud microphysics schemes. The Morrison and WDM6 schemes showed a similar tendency to give an FB value closer to 1 (Morrison: 1.07, WDM6: 1.13), and the odds ratios of these schemes (Morrison: 0.50, WDM6: 0.48) were higher than those of the other schemes (**Figure 29b**). The predictive skill of the model's cloud occurrence simulations, specifically the ability of each cloud microphysics scheme to accurately represent clouds in terms of timing, horizontal distribution, and altitude, revealed that these two schemes tended to overpredict cloud occurrence, but performed best. The NSSL and P3 schemes showed similar skill scores for FB value (NSSL: 1.30, P3: 1.56) and log-odds ratio (NSSL: 0.17, P3: 0.16), indicating that both schemes overpredicted clouds with significant biases. Overall, the differences between the microphysics schemes were slightly more pronounced in the log-odds ratio than in the FB values, suggesting that these schemes produced biased cloud simulations.
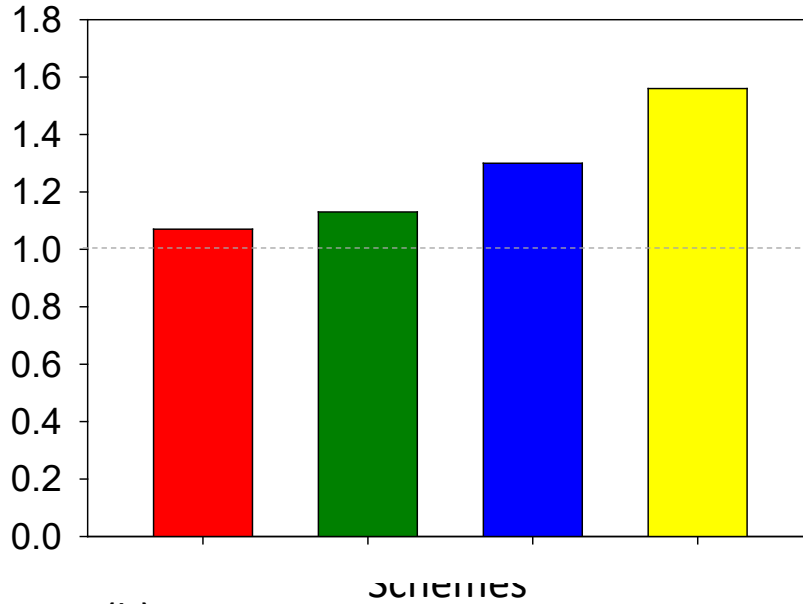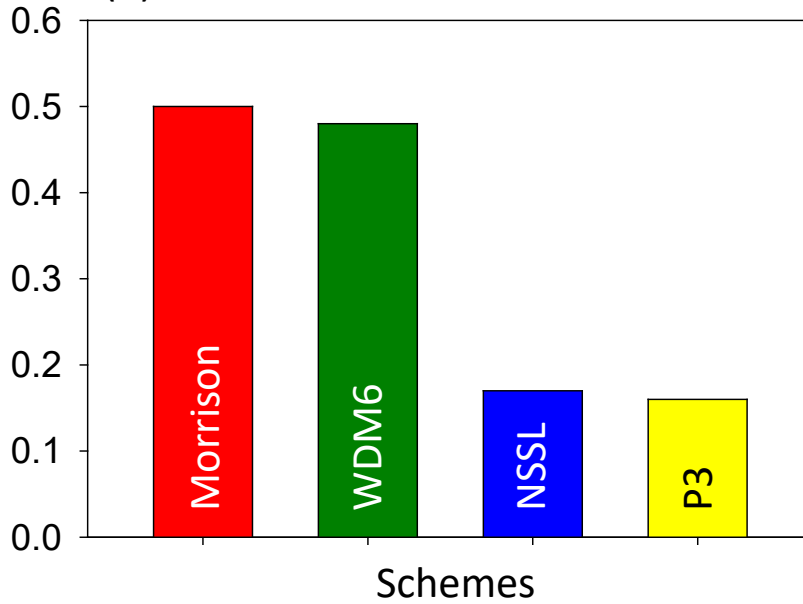
Figure 29. Performance scores of (a) frequency bias and (b) log-odds ratio on the PWRF cloud occurrence prediction derived from cloud fraction for each cloud microphysics scheme.

The distinction between liquid water droplets and ice crystals in the simulations varies mainly due to the temperature threshold (Bao et al., 2019; Klein et al., 2009). **Figure 30** shows the vertical profiles of liquid, rain, ice crystal, snow, and graupel hydrometeors averaged over time and domain for the four cloud microphysics schemes. Since the P3 scheme combines the mixing ratios of rimmed ice and deposited ice instead of separate mixing ratios for snow and graupel, the simulated snow and graupel mixing ratios from the Morrison, WDM6, and NSSL schemes were compared. The profiles obtained from these schemes showed marked differences in the formation of primary ice crystals in terms of temperature, hydrometeor mixing ratio, and saturation ratio (**Table 3**). The primary condensation simulated by the Morrison scheme is based on the mixing ratio of liquid and snow. However, the temperature required to initiate ice formation appeared too high for this scheme. The WDM6 and P3 schemes appeared to produce more ice crystals at lower altitudes, while the ice condensate gradually increased above 1.5 km (**Figure 30a**). It is worth noting that the Morrison scheme uses -8°C as the threshold for parameterization of deposition and condensation (Cooper, 1986). The liquid mixing ratio of the WDM6 scheme is an order of magnitude lower than the other schemes above 1.2 km, especially at 1-2.6 km (**Figure 30b**).

80
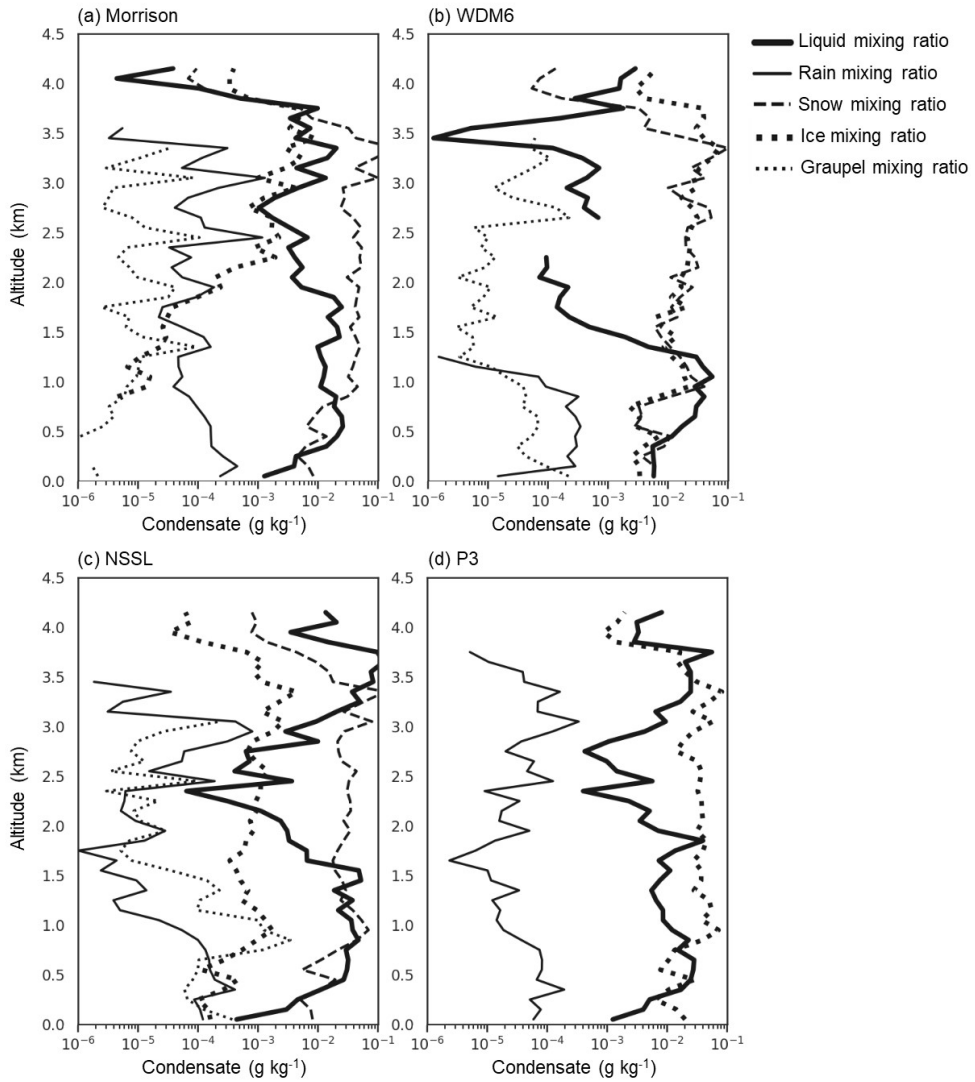
Figure 30. Vertical profiles of cloud liquid, rain, ice, snow, and graupel mixing ratio (g kg^{-1}) of hydrometeors simulated by four schemes: (a) Morrison, (b) WDM6, (c) NSSL, and (d) P3.

The increase in snow and ice condensate with altitude indicated that liquid hydrometeors were deposited as snow and ice, consistent with the deposition/concentration parameterization reported by Hong and Lim (2006). The liquid and snow mixing ratios for the NSSL scheme were higher than other hydrometeors. The NSSL scheme uses a homogeneous freezing threshold proposed by Bigg (1997) and incorporates the deposition and condensation parameterization reported by Cotton et al. (1986). The P3 scheme simulates liquid droplets, ice crystals, and low-value rain condensate. As P3 represents different properties of ice crystals within a single ice category, ice condensation in P3 is consistent with other schemes that combine ice crystal, snow, and graupel condensation. The general homogeneous freezing thresholds (-38°C) and deposition/condensation parameterization of Cooper (1986) were used in the P3 scheme. This scheme generates ice crystals using the same parameterization threshold as the Morrison scheme, but the Morrison scheme uses -4°C, whereas the P3 scheme uses -15°C. The difference in IWC between the Morrison and P3 schemes is attributed to the variation in temperature threshold.

Table 3. Characteristics of ice formation and ice-nucleating particle parameterization for the microphysics schemes.

Scheme	Triggering of ice formation	Ice-nucleating particle parameterization
Morrison	$T < -8°C$ & $S_w > 0.999$ or $S_i > 1.08$	Deposition/condensation (Cooper,1986)
	$T < -4°C$ & $q_c > 1.e^{-14}$	Contact nuclei (Meyers et al.,1992)
	$T < -4°C$ & $q_r > 1.e^{-14}$	Immersion freezing (Bigg,1955)
	$T < -40°C$ & ($q_c > 1.e^{-14}$ or $q_r > 1.e^{-14}$)	Homogeneous freezing of cloud water/rain
WDM6	$T < 0°C$ & $S > 0$	Deposition/nucleation
	$-70°C < T < 0°C$ & $q_r > 0$	Immersion freezing
	$-40°C < T < 0°C$ & $q_c > q_i$	Heterogeneous freezing (Bigg,1953)
	$T < -40°C$ & $q_c > 0$	Homogeneous freezing (Hong and Lim,2006)
NSSL	$S_w \geq 0$	Deposition/condensation
	$q_i > 1.e^{-12}$ & $D_i > 0$	Deposition/sublimation (Cotton et al.,1986)
	$T < -5°C$ & $q_c > 1.e^{-9}$	Homogeneous freezing (Bigg,1953; Ferrier, 1994)
	$T < -2°C$ & $q_c > 1.e^{-9}$	Contact nuclei (Meyers et al.,1992)
P3	$T < -15°C$ & $S_i > 1.05$	Deposition/condensation (Cooper,1986)
	$T < -4°C$ & $q_c \geq 1.e^{-14}$	Contact & immersion freezing
	$T < -40°C$ & $q_c \geq 1.e^{-14}$	Homogeneous freezing

T: atmospheric temperature, S: saturation ratio, S_w: saturation ratio for water, S_i: saturation ratio for ice, q_c: liquid water content, q_r : rain water content, q_c: cloud water content, q_i: ice water content, D_i: Diameter of ice

In the observed data, the amount of ice and liquid in the cloud is used as a criterion for classifying mixed-phase clouds, and the same classification criterion was applied to the model for comparative analysis. However, there are various liquid-ice interaction processes used in simulating clouds (cloud droplet evaporation and condensation, autoconversion, raindrop evaporation, conversion processes, snow, and graupel density and falling rates, aggregation processes, hail processes, and ice multiplication). Mixed-phase cloud physics and dynamics are known as nonlinear (Morrison et al., 2011), where the liquid-ice transition depends on the availability of complex microphysical interactions between supercooled liquid and ice nuclei. The present study focused on the relationship between cloud liquid and ice concentration and temperature for the partition question.

All schemes showed a similar liquid water mixing ratio in the clouds, about $0.8 \, \text{g kg}^{-1}$ at altitudes between 0.4 and 0.8 km. However, there were significant discrepancies between the schemes with respect to the microphysics of ice crystal, snow, and graupel production. Empirical parameterizations tailored to different temperature and/or supersaturation thresholds contribute to the differences in ice formation in each scheme (Barton et al., 2012; Sotiropoulou et al., 2021; Vignon et al., 2021).

Figure 31 shows the vertical temperature distribution observed during the ACLOUD campaign compared to radiosonde, dropsonde, and model simulations. Dropsondes were measured at Ny-Ålesund, Svalbard, at the beginning of each flight, while radiosondes were operated once per day, with launches every 6 hours during the ACLOUD campaign. It is important to note that both dropsondes and radiosondes were launched from Svalbard, but measured at different latitudes and longitudes compared to the ACLOUD flight observations. The mean temperature observed during the ACLOUD campaign shows a temperature inversion pattern similar to the dropsondes, while radiosondes and FNL (a model simulation) show a similar pattern below 0.3 km. All three observations show a similar temperature profile above the temperature inversion layer (at 0.3 km). Therefore, it can be concluded that the temperature bias due to the observation method is small, except for the geographical differences.
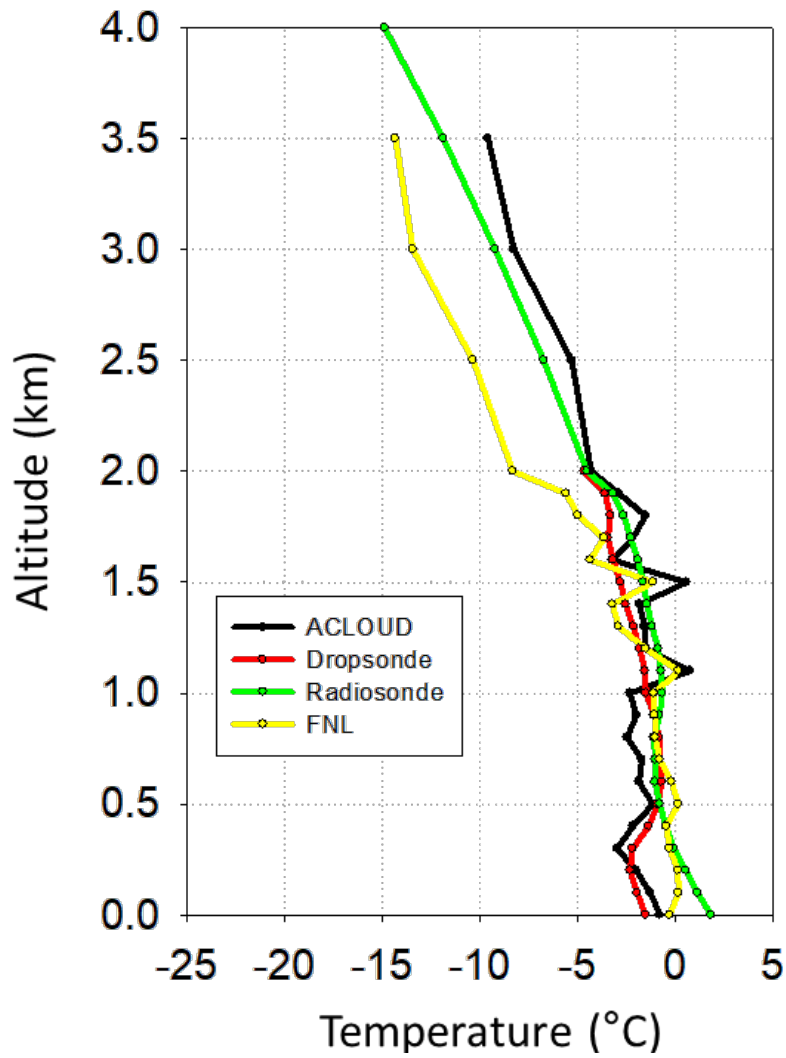
Figure 31. Vertical profile of observed and model-simulated temperature during the ACLOUD campaign. Polar 5 flight (black), dropsonde (red), radiosonde (green), a model product derived from NCEP FNL (yellow).

4.4 Radiative forcing at the surface

Climate and weather models tend to struggle to predict the observed frequency and persistence of Arctic mixed-phase clouds, leading to bias in surface radiative flux. These models also typically struggle with mixed-phase cloudiness at mid-latitudes (Illingworth et al., 2007). In order to improve the simulations, studies have suggested that a more robust treatment of the modelled cloud microphysics is required. A ratio of liquid to ice mass that is inconsistent with Arctic observations may be prescribed by models with less sophisticated microphysics. However, models with separate predictor variables for the liquid and the ice, and with detailed microphysical data, can lead to inaccurate results (Morrison et al., 2015).

These models may require more realistic treatment of ice microphysics, particularly the number concentration of small ice and snow, to improve results. Many modelling studies (Pinto, 1998; Harrington et al., 1999; Morrison and Pinto, 2005) have shown a strong sensitivity of mixed-phase clouds to ice crystal number concentration. By reducing the ice nucleus number concentration, which influences the ice crystal number concentration, from mid-latitude values to the low values observed in the Arctic, Prenni et al. (2007) significantly improved their simulation of mixed-phase clouds. The representation of ice nucleus

scavenging by ice precipitation is also sensitive in their simulation. Morrison and Pinto (2005) improved their Arctic mixed-phase stratus simulation by reducing the specified snow size distribution intercept parameter; this corresponds to reducing the snow number concentration for a given snow mixing ratio.

The relative importance of LW and SW cloud processes and their dependence on cloud microphysical properties can be assessed by calculating the radiative feedback from mixed-phase clouds. **Figure 32** shows box plots of BSRN radiative flux observations and model simulations of mixed-phase cloud cases during the ACLOUD campaign. In general, the model-simulated LW and SW fluxes are underestimated and overestimated, respectively. For LWU, there are minor differences between the models (Morrison: 313.3 W m^{-2}; WDM6: 311.2 W m^{-2}, NSSL: 311.3 W m^{-2}, P3: 311. 6 W m^{-2}), but in the case of LWD, the NSSL scheme simulated the least (248.3 W m^{-2}) with a significant bias (-56.2 W m^{-2}), and the Morrison scheme had the least bias (-48.1 W m^{-2}) with a mean of 257.4 W m^{-2}.

The simulated SWU for each cloud microphysics scheme is 201% higher than the BSRN observation (72.7 W m^{-2}). In the case of SWD, the model overestimates (observation: 235.0 W m^{-2}, Morrison: 328.1 Wm^{-2}, WDM6: 341.3 W m^{-2}, NSSL: 357.7 W m^{-2}, P3: 301.4 W m^{-2}), but the bias

seems to be smaller than for SWU.

Changes in surface reflectivity are the main contributor to the overestimation of SW radiation. Therefore, the model biases of the SW are more related to the simulation of the snow melt than to the properties of the clouds. LWU depends on surface properties and temperature, with the high underestimate representing model biases from the initial temperature limit. LWD flux, on the other hand, depends on atmospheric temperature and humidity, where each cloud microphysics scheme simulates differently. The underestimation of the LWD flux is highly correlated with the LWC bias of each scheme (**Figure 24a**).
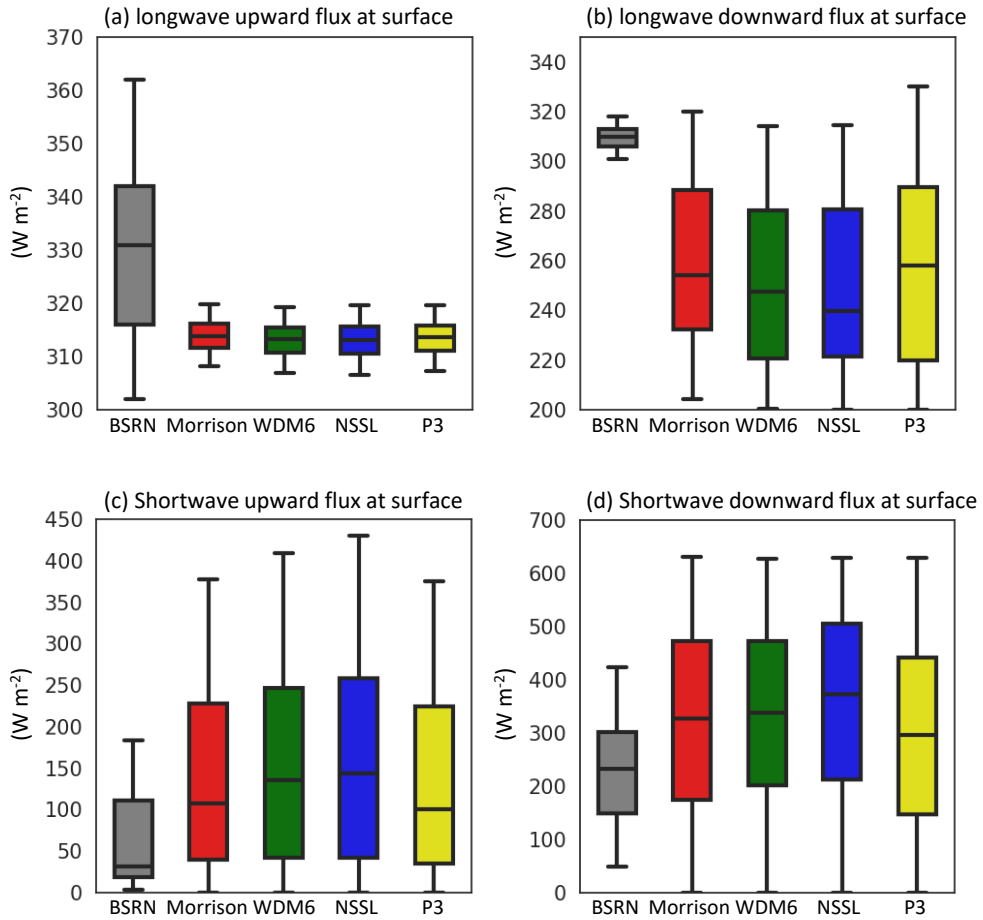
Figure 32. Box plots of (a) upwelling longwave flux, (b) downwelling flux, (c) upwelling shortwave flux, and (d) downwelling flux at the surface over Ny-Ålesund.

Chapter 5. Summary and future direction

The role of clouds in the complex Arctic environment is not fully understood. In order to develop a better representation of cloud-related climatological effects, cloud properties at Arctic stations are quantitatively investigated. Until recently, few Arctic observations have been conducted by air and ship campaigns, providing a short dataset for characterizing the macro- and microphysical and radiative properties of Arctic clouds. In June 2016, the Ny-Ålesund, Svalbard station for continuous cloud observations will be established, followed by the (AC)[3] project. The climate in Svalbard is generally complex and influenced by many factors, including the interaction of sea ice-ocean-atmosphere-land heat.

In the first part of this thesis, based on the ACLOUD flight campaign and Cloudnet observations over Ny-Ålesund station, Svalbard, a detailed analysis of cloud macro- and microphysical properties is performed. A classification of liquid and ice particles is essential to provide more accurate information on mixed-phase clouds, which is valuable for improving cloud parameterization in numerical weather prediction models. This study used additional conditions of IWF calculated from liquid and ice water content to avoid the limitation of lidar and radar observation calculated by Cloudnet algorithm. By using the new method

for classifying liquid, ice, and mixed-phase clouds, the total occurrences of clouds were found to be ~77.6% from February 2017 to February 2023. The most predominant cloud types are multilayer clouds, which occur 39.1% of the time, and single-layer clouds, which occur ~37.2% of the time. The total occurrences of single-layer ice clouds, liquid clouds and mixed phase clouds are 19%, 4.4% and 14.9%, respectively. In addition, surface measurements of SW and LW radiation in the upward and downward directions have been investigated in the framework of the BSRN at the Ny-Ålesund station. The relatively lower values of the upwelling and downwelling longwave fluxes for ice and mixed-phase clouds were highly correlated with the cloud top temperature by phase.

We evaluated the microphysical properties simulated by four cloud microphysics schemes (Morrison, WDM6, NSSL, and P3) in the PWRF model using in situ airborne observations during the ACLOUD experiment in the summer of 2017 (May-June). Our evaluation focused on the horizontal and vertical distribution of cloud occurrence, LWC, and IWC. Synoptic weather patterns during the ACLOUD campaign showed a high number of clouds around Svalbard due to the transport of air masses from the sea ice region to the open ocean, where adiabatic motions and sensible/latent heat fluxes heated the air masses.

The simulated microphysical properties of the clouds showed that the Morrison scheme best predicted cloud occurrence (i.e., a FB value of 1.07) and demonstrated accurate predictions with a high log-odds ratio (0.50). The WDM6 scheme also performed well during the study period, with FB (1.13) and log-odds ratio (0.48) values. The NSSL scheme produced mainly liquid and snow, and the simulated temperatures were too high to produce sufficient ice crystals at low altitudes. The Morrison scheme showed a 33% increase in ice mixing ratio above 1.3 km. The P3 scheme is designed to simulate different properties of ice crystals within a single ice category, and the ice condensation simulated by P3 was consistent with the combined snow, ice crystals, and graupel simulated by the Morrison and NSSL schemes. The WDM6 scheme produced higher ice mixing ratios compared to the Morrison and NSSL schemes, but the latter two schemes tended to produce more snow and graupel, which eventually combined to form IWC, resulting in less discrepancy between the three schemes. In addition, the NSSL scheme showed less bias in simulating IWC in mixed-phase clouds than the other schemes, suggesting that the ice-nucleating particle parameterization of the NSSL scheme effectively predicted mixed-phase clouds near Svalbard during the study period.

Overall, the cloud microphysics schemes underestimated both LWC and IWC compared to airborne observations. The significant differences in temperature thresholds for ice formation resulted in notable differences between simulated and observed IWC. The temperature bias pattern was consistent with the IWC simulated by the four cloud microphysics schemes. In the layer below 1.2 km, with a warm bias, less IWC is produced, while above 1.2 km, with a cold bias, a significant amount of IWC is produced. The PBL scheme is thought to be the main factor contributing to the IWC bias.

In addition, the mixed-phase cloud radiative flux was compared for each cloud microphysics scheme to assess the relative importance of the LW and SW cloud processes and to investigate their dependence on cloud microphysical properties. The main contribution to the overestimation of SW radiation is due to changes in surface reflectivity. Therefore, the model biases of SW are related to the simulation of snow melt rather than to the cloud properties simulated by the cloud microphysics scheme. LWU depends on surface properties and temperature, so a large underestimation represents model bias from the initial temperature boundary. LWD flux, on the other hand, depends on atmospheric temperature and humidity, which are simulated differently by each cloud microphysics scheme. The underestimation of the LWD flux is highly

94

correlated with the LWC bias of each scheme.

The interactions between aerosols, clouds, water vapor, and aerosols, and their feedback to longwave radiative fluxes in the Arctic are highly complex. To improve the simulation of Arctic clouds, further parameterization is needed to accurately represent ice nucleation particles, which should be developed in collaboration with field observations.

The cloud observation data used in this study are clouds that occurred during a very warm period in the Arctic, mainly observed near 0ºC near the surface, so the study was conducted with the expectation that the liquid and ice partitioning bias that occurs in the model simulation would be sensitive to temperature. It is a short time to conduct an additional sensitivity experiment and add it to this paper, but it seems that the analysis can be further extended with future research. Also, most of the mixed-phase cloud formation heights observed in this study were between 1 and 4 km. It seems that the nudging method can be used to improve the simulation of surface temperature, wind speed, and humidity to improve the accuracy of the simulation of mixed-phase clouds in the Arctic.

References

Achtert, P., Tesche, M., 2014. Assessing lidar-based classification schemes for polar stratospheric clouds based on 16 years of measurements at Esrange, Sweden. Journal of Geophysical Research: Atmospheres 119, 1386–1405. https://doi.org/10.1002/2013JD020355

Ali, Md.A., Islam, Md.M., Islam, Md.N., Almazroui, M., 2019. Investigations of MODIS AOD and cloud properties with CERES sensor based net cloud radiative effect and a NOAA HYSPLIT Model over Bangladesh for the period 2001–2016. Atmospheric Research 215, 268–283. https://doi.org/10.1016/j.atmosres.2018.09.001

Bae, S.Y., Hong, S.-Y., Lim, K.-S.S., 2016. Coupling WRF Double-Moment 6-Class Microphysics Schemes to RRTMG Radiation Scheme in Weather Research Forecasting Model. Advances in Meteorology 2016, e5070154. https://doi.org/10.1155/2016/5070154

Baker, B., Lawson, R.P., 2006. Improvement in Determination of Ice Water Content from Two-Dimensional Particle Imagery. Part I: Image-to-Mass Relationships. Journal of Applied Meteorology and Climatology 45, 1282–1290. https://doi.org/10.1175/JAM2398.1

Bao, J.-W., Michelson, S.A., Grell, E.D., 2019. Microphysical Process Comparison of Three Microphysics Parameterization Schemes in the WRF Model for an Idealized Squall-Line Case Study. Monthly Weather Review 147, 3093–3120. https://doi.org/10.1175/MWR-D-18-0249.1

Barton, N.P., Klein, S.A., Boyle, J.S., Zhang, Y.Y., 2012. Arctic synoptic regimes: Comparing domain-wide Arctic cloud observations with CAM4 and CAM5 during similar dynamics. Journal of Geophysical Research: Atmospheres 117.

https://doi.org/10.1029/2012JD017589

Barton, N.P., Klein, S.A., Boyle, J.S., 2014. On the Contribution of Longwave Radiation to Global Climate Model Biases in Arctic Lower Tropospheric Stability. Journal of Climate 27, 7250–7269. https://doi.org/10.1175/JCLI-D-14-00126.1

Battisti, A., Acevedo, O.C., Costa, F.D., Puhales, F.S., Anabor, V., Degrazia, G.A., 2017. Evaluation of Nocturnal Temperature Forecasts Provided by the Weather Research and Forecast Model for Different Stability Regimes and Terrain Characteristics. Boundary-Layer Meteorol 162, 523–546. https://doi.org/10.1007/s10546-016-0209-y

Baumgardner, D., Brenguier, J.L., Bucholtz, A., Coe, H., DeMott, P., Garrett, T.J., Gayet, J.F., Hermann, M., Heymsfield, A., Korolev, A., Krämer, M., Petzold, A., Strapp, W., Pilewskie, P., Taylor, J., Twohy, C., Wendisch, M., Bachalo, W., Chuang, P., 2011. Airborne instruments to measure atmospheric aerosol particles, clouds and radiation: A cook's tour of mature and emerging technology. Atmospheric Research 102, 10–29. https://doi.org/10.1016/j.atmosres.2011.06.021

Bennartz, R., Shupe, M.D., Turner, D.D., Walden, V.P., Steffen, K., Cox, C.J., Kulie, M.S., Miller, N.B., Pettersen, C., 2013. July 2012 Greenland melt extent enhanced by low-level liquid clouds. Nature 496, 83–86. https://doi.org/10.1038/nature12002

Bigg, E.K., 1953. The Supercooling of Water. Proc. Phys. Soc. B 66, 688. https://doi.org/10.1088/0370-1301/66/8/309

Bigg, E.K., 1955. Ice-crystal counts and the freezing of water drops. Quarterly Journal of the Royal Meteorological Society 81, 478–479. https://doi.org/10.1002/qj.49708134920

Bigg, E.K., 1997. An independent evaluation of a South African hygroscopic cloud seeding experiment, 1991–1995. Atmospheric Research 43, 111–127. https://doi.org/10.1016/S0169-8095(96)00019-1

Boer, G. de, Eloranta, E.W., Shupe, M.D., 2009. Arctic Mixed-Phase Stratiform Cloud Properties from Multiple Years of Surface-Based Measurements at Two High-Latitude Locations. Journal of the Atmospheric Sciences 66, 2874–2887. https://doi.org/10.1175/2009JAS3029.1

Boer, G. de, Chapman, W., Kay, J.E., Medeiros, B., Shupe, M.D., Vavrus, S., Walsh, J., 2012. A Characterization of the Present-Day Arctic Atmosphere in CCSM4. Journal of Climate 25, 2676–2695. https://doi.org/10.1175/JCLI-D-11-00228.1

Boer, G., Shupe, M.D., Caldwell, P.M., Bauer, S.E., Persson, O., Boyle, J.S., Kelley, M., Klein, S.A., Tjernström, M., 2014. Near-surface meteorology during the Arctic Summer Cloud Ocean Study (ASCOS): evaluation of reanalyses and global climate models. Atmospheric Chemistry and Physics 14, 427–445. https://doi.org/10.5194/acp-14-427-2014

Boisvert, L.N., Webster, M.A., Petty, A.A., Markus, T., Bromwich, D.H., Cullather, R.I., 2018. Intercomparison of Precipitation Estimates over the Arctic Ocean and Its Peripheral Seas from Reanalyses. Journal of Climate 31, 8441–8462. https://doi.org/10.1175/JCLI-D-18-0125.1

Bromwich, D.H., Wilson, A.B., Bai, L.-S., Moore, G.W.K., Bauer, P., 2016. A comparison of the regional Arctic System Reanalysis and the global ERA-Interim Reanalysis for the Arctic. Quarterly Journal of the Royal Meteorological Society 142, 644–658. https://doi.org/10.1002/qj.2527

Brown, P.R.A., Francis, P.N., 1995. Improved Measurements of the Ice Water Content in Cirrus Using a Total-Water Probe. Journal of Atmospheric and Oceanic Technology 12, 410–414. https://doi.org/10.1175/1520-0426(1995)012<0410:IMOTIW>2.0.CO;2

Cesana, G., Kay, J.E., Chepfer, H., English, J.M., de Boer, G., 2012. Ubiquitous low-level liquid-containing Arctic clouds: New observations and climate model constraints from CALIPSO-GOCCP. Geophysical Research Letters 39. https://doi.org/10.1029/2012GL053385

Chan, M.A., Comiso, J.C., 2013. Arctic Cloud Characteristics as Derived from MODIS, CALIPSO, and CloudSat. Journal of Climate 26, 3285–3306. https://doi.org/10.1175/JCLI-D-12-00204.1

Chapin, F.S., Sturm, M., Serreze, M.C., McFadden, J.P., Key, J.R., Lloyd, A.H., McGuire, A.D., Rupp, T.S., Lynch, A.H., Schimel, J.P., Beringer, J., Chapman, W.L., Epstein, H.E., Euskirchen, E.S., Hinzman, L.D., Jia, G., Ping, C.-L., Tape, K.D., Thompson, C.D.C., Walker, D.A., Welker, J.M., 2005. Role of Land-Surface Changes in Arctic Summer Warming. Science 310, 657–660. https://doi.org/10.1126/science.1117368

Chepfer, H., Bony, S., Winker, D., Cesana, G., Dufresne, J.L., Minnis, P., Stubenrauch, C.J., Zeng, S., 2010. The GCM-Oriented CALIPSO Cloud Product (CALIPSO-GOCCP). Journal of Geophysical Research: Atmospheres 115. https://doi.org/10.1029/2009JD012251

Cooper, W.A., 1986. Ice Initiation in Natural Clouds, in: Braham, R.R., Cooper, W.A., Cotton, W.R., Elliot, R.D., Flueck, J.A., Fritsch, J.M., Gagin, A., Grant, L.O., Heymsfield, A.J., Hill, G.E., Isaac, G.A., Marwitz, J.D., Orville, H.D., Rangno, A.L., Silverman, B.A., Smith, P.L. (Eds.), Precipitation Enhancement—A Scientific Challenge, Meteorological Monographs. American Meteorological Society, Boston, MA, pp. 29–32. https://doi.org/10.1007/978-1-935704-

17-1_4

Cotton, W.R., 1986. Averaging and the Parameterization of Physical Processes in Mesoscale Models, in: Ray, P.S. (Ed.), Mesoscale Meteorology and Forecasting. American Meteorological Society, Boston, MA, pp. 614–635. https://doi.org/10.1007/978-1-935704-20-1_26

Ding, Q., Schweiger, A., L'Heureux, M., Battisti, D.S., Po-Chedley, S., Johnson, N.C., Blanchard-Wrigglesworth, E., Harnos, K., Zhang, Q., Eastman, R., Steig, E.J., 2017. Influence of high-latitude atmospheric circulation changes on summertime Arctic sea ice. Nature Clim Change 7, 289–295. https://doi.org/10.1038/nclimate3241

Dong, T.-Y., Dong, W.-J., Guo, Y., Chou, J.-M., Yang, S.-L., Tian, D., Yan, D.-D., 2018. Future temperature changes over the critical Belt and Road region based on CMIP5 models. Advances in Climate Change Research, Including special topic on China Energy Modeling Forum 9, 57–65. https://doi.org/10.1016/j.accre.2018.01.003

Ehrlich, A., Wendisch, M., Lüpkes, C., Buschmann, M., Bozem, H., Chechin, D., Clemen, H.-C., Dupuy, R., Eppers, O., Hartmann, J., Herber, A., Jäkel, E., Järvinen, E., Jourdan, O., Kästner, U., Kliesch, L.-L., Köllner, F., Mech, M., Mertes, S., Neuber, R., Ruiz-Donoso, E., Schnaiter, M., Schneider, J., Stapf, J., Zanatta, M., 2019. A comprehensive in situ and remote sensing data set from the Arctic CLoud Observations Using airborne measurements during polar Day (ACLOUD) campaign. Earth System Science Data 11, 1853–1881. https://doi.org/10.5194/essd-11-1853-2019

English, J.M., Kay, J.E., Gettelman, A., Liu, X., Wang, Y., Zhang, Y., Chepfer, H., 2014. Contributions of Clouds, Surface Albedos, and Mixed-Phase Ice Nucleation Schemes to Arctic Radiation Biases in CAM5. Journal of Climate 27, 5174–5197. https://doi.org/10.1175/JCLI-D-13-00608.1

Frisch, A.S., Feingold, G., Fairall, C.W., Uttal, T., Snider, J.B., 1998. On cloud radar and microwave radiometer measurements of stratus cloud liquid water profiles. Journal of Geophysical Research: Atmospheres 103, 23195–23197. https://doi.org/10.1029/98JD01827

Frisch, P.C., Grodnicki, L., Welty, D.E., 2002. The Velocity Distribution of the Nearest Interstellar Gas. ApJ 574, 834. https://doi.org/10.1086/341001

Garrett, T., Radke, L., and Hobbs, P., 2002. Aerosol effects on cloud emissivity and surface longwave heating in the Arctic, J. Atmos. Sci., 59, 769–778, doi:10.1175/1520- 0469,0592.0.CO;2, 2002.

Garrett, T.J., Zhao, C., 2006. Increased Arctic cloud longwave emissivity associated with pollution from mid-latitudes. Nature 440, 787–789. https://doi.org/10.1038/nature04636

Gevorgyan, A., 2018. Convection-Permitting Simulation of a Heavy Rainfall Event in Armenia Using the WRF Model. Journal of Geophysical Research: Atmospheres 123, 11,008-11,029. https://doi.org/10.1029/2017JD028247

Goosse, H., Kay, J. E., Armour, K. C., Bodas-Salcedo, A., Chepfer, H., Docquier, D., Jonko, A., Kushner, P. J., Lecomte, O., Massonnet, F., Park, H. S., Pithan, F., Svensson, G., and Vancoppenolle, M., 2018. Quantifying climate feedbacks in polar regions, Nat. Commun., 9, 1919, doi:10.1038/s41467-018-04173-0.

Graham, R.M., Rinke, A., Cohen, L., Hudson, S.R., Walden, V.P., Granskog, M.A., Dorn, W., Kayser, M., Maturilli, M., 2017. A comparison of the two Arctic atmospheric winter states observed during N-ICE2015 and SHEBA. Journal of Geophysical Research: Atmospheres 122, 5716–5737. https://doi.org/10.1002/2016JD025475

Graversen, R.G., Mauritsen, T., Drijfhout, S., Tjernström, M., Mårtensson, S., 2011. Warm winds from the Pacific caused extensive Arctic sea-ice melt in summer 2007. Clim Dyn 36, 2103–2112. https://doi.org/10.1007/s00382-010-0809-z

Guo, J., Lei, H., Chen, D., Yang, J., 2019. Evaluation of the WDM6 scheme in the simulation of number concentrations and drop size distributions of warm-rain hydrometeors: comparisons with the observations and other schemes. Atmospheric and Oceanic Science Letters 12, 458–466. https://doi.org/10.1080/16742834.2019.1670584

Halder, M., Hazra, A., Mukhopadhyay, P., Siingh, D., 2015. Effect of the better representation of the cloud ice-nucleation in WRF microphysics schemes: A case study of a severe storm in India. Atmospheric Research 154, 155–174. https://doi.org/10.1016/j.atmosres.2014.10.022

Halder, M., Mukhopadhyay, P., 2016. Microphysical processes and hydrometeor distributions associated with thunderstorms over India: WRF (cloud-resolving) simulations and validations using TRMM. Nat Hazards 83, 1125–1155. https://doi.org/10.1007/s11069-016-2365-2

Harrington, J.Y., Reisin, T., Cotton, W.R., Kreidenweis, S.M., 1999. Cloud resolving simulations of Arctic stratus: Part II: Transition-season clouds. Atmospheric Research 51, 45–75. https://doi.org/10.1016/S0169-8095(98)00098-2

Haugstad, A.D., Armour, K.C., Battisti, D.S., Rose, B.E.J., 2017. Relative roles of surface temperature and climate forcing patterns in the inconstancy of radiative feedbacks. Geophysical Research Letters 44, 7455–7463. https://doi.org/10.1002/2017GL074372

Hines, K.M., Bromwich, D.H., 2008. Development and Testing of Polar Weather Research and Forecasting (WRF) Model. Part I: Greenland Ice Sheet Meteorology. Monthly Weather Review 136, 1971–1989. https://doi.org/10.1175/2007MWR2112.1

Hines, K.M., Bromwich, D.H., 2017. Simulation of Late Summer Arctic Clouds during ASCOS with Polar WRF. Monthly Weather Review 145, 521–541. https://doi.org/10.1175/MWR-D-16-0079.1

Hines, K.M., Bromwich, D.H., Wang, S.-H., Silber, I., Verlinde, J., Lubin, D., 2019. Microphysics of summer clouds in central West Antarctica simulated by the Polar Weather Research and Forecasting Model (WRF) and the Antarctic Mesoscale Prediction System (AMPS). Atmospheric Chemistry and Physics 19, 12431–12454. https://doi.org/10.5194/acp-19-12431-2019

Hines, K.M., Bromwich, D.H., Silber, I., Russell, L.M., Bai, L., 2021. Predicting Frigid Mixed-Phase Clouds for Pristine Coastal Antarctica. Journal of Geophysical Research: Atmospheres 126, e2021JD035112. https://doi.org/10.1029/2021JD035112

Hogan, R., Connor, E., 2004. Facilitating cloud radar and lidar algorithms: the Cloudnet Instrument Synergy/Target Categorization product.

Hogan, R. J., M. P. Mittermaier, A. J. Illingworth, 2006. "The Retrieval of Ice Water Content from Radar Reflectivity Factor and Temperature and Its Use in Evaluating a Mesoscale Model". Journal of Applied Meteorology and Climatology 45.2, pp. 301–317. doi: 10.1175/JAM2340.1.

Hogan, R.J., O'Connor, E.J., Illingworth, A.J., 2009. Verification of cloud-fraction forecasts. Quarterly Journal of the Royal Meteorological Society 135, 1494–1511. https://doi.org/10.1002/qj.481

Holt, T., Raman, S., 1988. A review and comparative evaluation of multilevel boundary layer parameterizations for first-order and turbulent kinetic energy closure schemes. Reviews of Geophysics 26, 761–780. https://doi.org/10.1029/RG026i004p00761

Hong, S. Y., and Lim, J. O. J., 2006. The WRF single-moment 6-class microphysics scheme (WSM6). Asia-Pacific Journal of Atmospheric Sciences, 42(2), 129-151.

Hong, S.-Y., Lim, K.-S.S., Lee, Y.-H., Ha, J.-C., Kim, H.-W., Ham, S.-J., Dudhia, J., 2010. Evaluation of the WRF Double-Moment 6-Class Microphysics Scheme for Precipitating Convection. Advances in Meteorology 2010, e707253. https://doi.org/10.1155/2010/707253

Hua, S., Chen, B., Liu, Y., Chen, G., Yang, Y., Dong, X., Zhao, Z., Gao, Y., Zhou, X., Zhang, R., Duan, J., 2023. Evaluation of the Ice Particle Simulation of Microphysics Schemes with Aircraft Measurements of a Stratiform Cloud in North China. Journal of the Atmospheric Sciences 80, 1635–1656. https://doi.org/10.1175/JAS-D-22-0155.1

Huang, X.-Y., Xiao, Q., Barker, D.M., Zhang, Xin, Michalakes, J., Huang, W., Henderson, T., Bray, J., Chen, Y., Ma, Z., Dudhia, J., Guo, Y., Zhang, Xiaoyan, Won, D.-J., Lin, H.-C., Kuo, Y.-H., 2009. Four-Dimensional Variational Data Assimilation for WRF: Formulation and Preliminary Results. Monthly Weather Review 137, 299–314. https://doi.org/10.1175/2008MWR2577.1

Huang, Y., Chou, G., Xie, Y., Soulard, N., 2019. Radiative Control of the Interannual Variability of Arctic Sea Ice. Geophysical Research Letters 46, 9899–9908. https://doi.org/10.1029/2019GL084204

Huang, Y., Wu, W., McFarquhar, G.M., Wang, X., Morrison, H., Ryzhkov, A., Hu, Y., Wolde, M., Nguyen, C., Schwarzenboeck, A., Milbrandt, J., Korolev, A.V., Heckman, I., 2021. Microphysical processes

producing high ice water contents (HIWCs) in tropical convective clouds during the HAIC-HIWC field campaign: evaluation of simulations using bulk microphysical schemes. Atmospheric Chemistry and Physics 21, 6919–6944. https://doi.org/10.5194/acp-21-6919-2021

Illingworth, A.J., Hogan, R.J., O'Connor, E.J., Bouniol, D., Brooks, M.E., Delanoé, J., Donovan, D.P., Eastment, J.D., Gaussiat, N., Goddard, J.W.F., Haeffelin, M., Baltink, H.K., Krasnov, O.A., Pelon, J., Piriou, J.-M., Protat, A., Russchenberg, H.W.J., Seifert, A., Tompkins, A.M., Zadelhoff, G.-J. van, Vinit, F., Willén, U., Wilson, D.R., Wrench, C.L., 2007. Cloudnet: Continuous Evaluation of Cloud Profiles in Seven Operational Models Using Ground-Based Observations. Bulletin of the American Meteorological Society 88, 883–898. https://doi.org/10.1175/BAMS-88-6-883

Intrieri, J.M., Shupe, M.D., Uttal, T., McCarty, B.J., 2002. An annual cycle of Arctic cloud characteristics observed by radar and lidar at SHEBA. Journal of Geophysical Research: Oceans 107, SHE 5-1-SHE 5-15. https://doi.org/10.1029/2000JC000423

James, K.A., Stensrud, D.J., Yussouf, N., 2009. Value of Real-Time Vegetation Fraction to Forecasts of Severe Convection in High-Resolution Models. Weather and Forecasting 24, 187–210. https://doi.org/10.1175/2008WAF2007097.1

Johnson, M., Jung, Y., Dawson, D.T., Xue, M., 2016. Comparison of Simulated Polarimetric Signatures in Idealized Supercell Storms Using Two-Moment Bulk Microphysics Schemes in WRF. Monthly Weather Review 144, 971–996. https://doi.org/10.1175/MWR-D-15-0233.1

Kant, S., Panda, J., Gautam, R., 2019. A seasonal analysis of aerosol-cloud-radiation interaction over Indian region during 2000–2017. Atmospheric Environment 201, 212–222. https://doi.org/10.1016/j.atmosenv.2018.12.044

105

Kay, J. E., L'Ecuyer, T., Chepfer, H., Loeb, N., Morrison, A., and Cesana, G., 2016. Recent Advances in Arctic Cloud and Climate Research, Current Climate Change Reports, 2, 159–169, doi:10.1007/s40641-016-0051-9.

Khain, A., Lynn, B., Shpund, J., 2016. High resolution WRF simulations of Hurricane Irene: Sensitivity to aerosols and choice of microphysical schemes. Atmospheric Research 167, 129–145. https://doi.org/10.1016/j.atmosres.2015.07.014

Kilpeläinen, T., Vihma, T., Manninen, M., Sjöblom, A., Jakobson, E., Palo, T., Maturilli, M., 2012. Modelling the vertical structure of the atmospheric boundary layer over Arctic fjords in Svalbard. Quarterly Journal of the Royal Meteorological Society 138, 1867–1883. https://doi.org/10.1002/qj.1914

Kim, D.-H., Kim, H.M., 2022. Effect of data assimilation in the Polar WRF with 3DVAR on the prediction of radiation, heat flux, cloud, and near surface atmospheric variables over Svalbard. Atmospheric Research 272, 106155. https://doi.org/10.1016/j.atmosres.2022.106155

Klein, S.A., McCoy, R.B., Morrison, H., Ackerman, A.S., Avramov, A., Boer, G. de, Chen, M., Cole, J.N.S., Del Genio, A.D., Falk, M., Foster, M.J., Fridlind, A., Golaz, J.-C., Hashino, T., Harrington, J.Y., Hoose, C., Khairoutdinov, M.F., Larson, V.E., Liu, X., Luo, Y., McFarquhar, G.M., Menon, S., Neggers, R.A.J., Park, S., Poellot, M.R., Schmidt, J.M., Sednev, I., Shipway, B.J., Shupe, M.D., Spangenberg, D.A., Sud, Y.C., Turner, D.D., Veron, D.E., Salzen, K. von, Walker, G.K., Wang, Z., Wolf, A.B., Xie, S., Xu, K.-M., Yang, F., Zhang, G., 2009. Intercomparison of model simulations of mixed-phase clouds observed during the ARM Mixed-Phase Arctic Cloud Experiment. I: single layer cloud. Quarterly Journal of the Royal Meteorological Society 135, 979–1002. https://doi.org/10.1002/qj.416

Knudsen, E.M., Heinold, B., Dahlke, S., Bozem, H., Crewell, S., Heygster, G., Kunkel, D., Maturilli, M., Mech, M., Rinke, A., Schmithüsen, H., Ehrlich, A., Macke, A., Lüpkes, C., Wendisch, M., 2018. Synoptic development during the ACLOUD/PASCAL field campaign near Svalbard in spring 2017 (preprint). Clouds and Precipitation/Field Measurements/Troposphere/Physics (physical properties and processes). https://doi.org/10.5194/acp-2018-494

Korolev, A., Milbrandt, J., 2022. How Are Mixed-Phase Clouds Mixed? Geophysical Research Letters 49, e2022GL099578. https://doi.org/10.1029/2022GL099578

Kretzschmar, J., Stapf, J., Klocke, D., Wendisch, M., Quaas, J., 2020. Employing airborne radiation and cloud microphysics observations to improve cloud representation in ICON at kilometer-scale resolution in the Arctic. Atmospheric Chemistry and Physics 20, 13145–13165. https://doi.org/10.5194/acp-20-13145-2020

Lance, S., Brock, C.A., Rogers, D., Gordon, J.A., 2010. Water droplet calibration of the Cloud Droplet Probe (CDP) and in-flight performance in liquid, ice and mixed-phase clouds during ARCPAC. Atmospheric Measurement Techniques 3, 1683–1706. https://doi.org/10.5194/amt-3-1683-2010

Lawson, R.P., Zuidema, P., 2009. Aircraft Microphysical and Surface-Based Radar Observations of Summertime Arctic Clouds. Journal of the Atmospheric Sciences 66, 3505–3529. https://doi.org/10.1175/2009JAS3177.1

Lee, H.J., Kwon, M.O., Yeh, S.-W., Kwon, Y.-O., Park, W., Park, J.-H., Kim, Y.H., Alexander, M.A., 2017. Impact of Poleward Moisture Transport from the North Pacific on the Acceleration of Sea Ice Loss in the Arctic since 2002. Journal of Climate 30, 6757–6769. https://doi.org/10.1175/JCLI-D-16-0461.1

Lelli, L., Vountas, M., Khosravi, N., Burrows, J.P., 2022. Satellite-based evidence of regional and seasonal Arctic cooling by brighter and wetter clouds. Atmospheric Chemistry and Physics Discussions 1–38. https://doi.org/10.5194/acp-2022-28

Li, X., Pu, Z., 2008. Sensitivity of Numerical Simulation of Early Rapid Intensification of Hurricane Emily (2005) to Cloud Microphysical and Planetary Boundary Layer Parameterizations. Monthly Weather Review 136, 4819–4838. https://doi.org/10.1175/2008MWR2366.1

Li, X., Zhang, Q., Xue, H., 2017. The role of initial cloud condensation nuclei concentration in hail using the WRF NSSL 2-moment microphysics scheme. Adv. Atmos. Sci. 34, 1106–1120. https://doi.org/10.1007/s00376-017-6237-9

Lim, K.-S.S., Hong, S.-Y., 2010. Development of an Effective Double-Moment Cloud Microphysics Scheme with Prognostic Cloud Condensation Nuclei (CCN) for Weather and Climate Models. Monthly Weather Review 138, 1587–1612. https://doi.org/10.1175/2009MWR2968.1

Lohmann, U., Zhang, J., Pi, J., 2003. Sensitivity studies of the effect of increased aerosol concentrations and snow crystal shape on the snowfall rate in the Arctic. Journal of Geophysical Research: Atmospheres 108. https://doi.org/10.1029/2003JD003377

Lubin, D., Zhang, D., Silber, I., Scott, R.C., Kalogeras, P., Battaglia, A., Bromwich, D.H., Cadeddu, M., Eloranta, E., Fridlind, A., Frossard, A., Hines, K.M., Kneifel, S., Leaitch, W.R., Lin, W., Nicolas, J., Powers, H., Quinn, P.K., Rowe, P., Russell, L.M., Sharma, S., Verlinde, J., Vogelmann, A.M., 2020. AWARE: The Atmospheric Radiation Measurement (ARM) West Antarctic Radiation Experiment. Bulletin of the American Meteorological Society 101, E1069–E1091. https://doi.org/10.1175/Bmixed-phase cloud-D-18-0278.1

Luke, E.P., Yang, F., Kollias, P., Vogelmann, A.M., Maahn, M., 2021. New insights into ice multiplication using remote-sensing observations of slightly supercooled mixed-phase clouds in the Arctic. Proceedings of the National Academy of Sciences of the United States of America 118. https://doi.org/10.1073/pnas.2021387118

Mansell, E.R., Ziegler, C.L., Bruning, E.C., 2010. Simulated Electrification of a Small Thunderstorm with Two-Moment Bulk Microphysics. Journal of the Atmospheric Sciences 67, 171–194. https://doi.org/10.1175/2009JAS2965.1

Marchand, R., Mace, G.G., Ackerman, T., Stephens, G., 2008. Hydrometeor Detection Using Cloudsat—An Earth-Orbiting 94-GHz Cloud Radar. Journal of Atmospheric and Oceanic Technology 25, 519–533. https://doi.org/10.1175/2007JTECHA1006.1

Meyers, M.P., DeMott, P.J., Cotton, W.R., 1992. New Primary Ice-Nucleation Parameterizations in an Explicit Cloud Model. Journal of Applied Meteorology and Climatology 31, 708–721. https://doi.org/10.1175/1520-0450(1992)031<0708:NPINPI>2.0.CO;2

Miller, N.B., Shupe, M.D., Cox, C.J., Walden, V.P., Turner, D.D., Steffen, K., 2015. Cloud Radiative Forcing at Summit, Greenland. Journal of Climate 28, 6267–6280. https://doi.org/10.1175/JCLI-D-15-0076.1

Mioche, G., Jourdan, O., Delanoë, J., Gourbeyre, C., Febvre, G., Dupuy, R., Monier, M., Szczap, F., Schwarzenboeck, A., Gayet, J.-F., 2017. Vertical distribution of microphysical properties of Arctic springtime low-level mixed-phase clouds over the Greenland and Norwegian seas. Atmospheric Chemistry and Physics 17, 12845–12869. https://doi.org/10.5194/acp-17-12845-2017

Mittermaier, M., 2012. A critical assessment of surface cloud observations and their use for verifying cloud forecasts. Quarterly Journal of the Royal Meteorological Society 138, 1794–1807. https://doi.org/10.1002/qj.1918

Morrison, H., and J. O. Pinto., 2005. Mesoscale modeling of springtime Arctic mixed-phase stratiform clouds using a new two-moment bulk microphysics scheme. Journal of the atmospheric sciences62.10, 3683-3704.

Morrison, H., Pinto, J.O., 2006. Intercomparison of Bulk Cloud Microphysics Schemes in Mesoscale Simulations of Springtime Arctic Mixed-Phase Stratiform Clouds. Monthly Weather Review 134, 1880–1900. https://doi.org/10.1175/MWR3154.1

Morrison, H., Thompson, G., Tatarskii, V., 2009. Impact of Cloud Microphysics on the Development of Trailing Stratiform Precipitation in a Simulated Squall Line: Comparison of One- and Two-Moment Schemes. Monthly Weather Review 137, 991–1007. https://doi.org/10.1175/2008MWR2556.1

Morrison, H., Zuidema, P., McFarquhar, G.M., Bansemer, A., Heymsfield, A.J., 2011. Snow microphysical observations in shallow mixed-phase and deep frontal Arctic cloud systems. Quarterly Journal of the Royal Meteorological Society 137, 1589–1601. https://doi.org/10.1002/qj.840

Morrison, H., de Boer, G., Feingold, G., Harrington, J., Shupe, M.D., Sulia, K., 2012. Resilience of persistent Arctic mixed-phase clouds. Nature Geosci 5, 11–17. https://doi.org/10.1038/ngeo1332

Morrison, H., Milbrandt, J.A., 2015. Parameterization of Cloud Microphysics Based on the Prediction of Bulk Ice Particle Properties. Part I: Scheme Description and Idealized Tests. Journal of the Atmospheric Sciences 72, 287–311. https://doi.org/10.1175/JAS-D-14-0065.1

Morrison, H., Milbrandt, J.A., Bryan, G.H., Ikeda, K., Tessendorf, S.A., Thompson, G., 2015. Parameterization of Cloud Microphysics Based on the Prediction of Bulk Ice Particle Properties. Part II: Case Study Comparisons with Observations and Other Schemes. Journal of the Atmospheric Sciences 72, 312–339. https://doi.org/10.1175/JAS-D-14-0066.1

NCEP, F., 1999. National Centers for Environmental Prediction/National Weather Service/NOAA/US Department of Commerce. 2000, updated daily.NCEP FNL Operational Model Global Tropospheric Analyses, continuing from July.

Nguyen, C.M., Wolde, M., Battaglia, A., Nichman, L., Bliankinshtein, N., Haimov, S., Bala, K., Schuettemeyer, D., 2022. Coincident in situ and triple-frequency radar airborne observations in the Arctic. Atmospheric Measurement Techniques 15, 775–795. https://doi.org/10.5194/amt-15-775-2022

Nomokonova, T., Ebell, K., Löhnert, U., Maturilli, M., Ritter, C., O'Connor, E., 2019. Statistics on clouds and their relation to thermodynamic conditions at Ny-Ålesund using ground-based sensor synergy. Atmospheric Chemistry and Physics 19, 4105–4126. https://doi.org/10.5194/acp-19-4105-2019

Otkin, J.A., Greenwald, T.J., 2008. Comparison of WRF Model-Simulated and MODIS-Derived Cloud Data. Monthly Weather Review 136, 1957–1970. https://doi.org/10.1175/2007MWR2293.1

Palm, S.P., Strey, S.T., Spinhirne, J., Markus, T., 2010. Influence of Arctic sea ice extent on polar cloud fraction and vertical structure and implications for regional climate. Journal of Geophysical Research: Atmospheres 115. https://doi.org/10.1029/2010JD013900

Park, H.-S., Sohn, B.J., 2010. Recent trends in changes of vegetation over East Asia coupled with temperature and rainfall variations. Journal of Geophysical Research: Atmospheres 115.

https://doi.org/10.1029/2009JD012752

Park, S., Bretherton, C.S., Rasch, P.J., 2014. Integrating Cloud Processes in the Community Atmosphere Model, Version 5. Journal of Climate 27, 6821–6856. https://doi.org/10.1175/JCLI-D-14-00087.1

Pinto, J.O., 1998. Autumnal Mixed-Phase Cloudy Boundary Layers in the Arctic. Journal of the Atmospheric Sciences 55, 2016–2038. https://doi.org/10.1175/1520-0469(1998)055<2016:AMPCBL>2.0.CO;2

Powers, J.G., 2007. Numerical Prediction of an Antarctic Severe Wind Event with the Weather Research and Forecasting (WRF) Model. Monthly Weather Review 135, 3134–3157. https://doi.org/10.1175/MWR3459.1

Prenni, A.J., Harrington, J.Y., Tjernström, M., DeMott, P.J., Avramov, A., Long, C.N., Kreidenweis, S.M., Olsson, P.Q., Verlinde, J., 2007. Can Ice-Nucleating Aerosols Affect Arctic Seasonal Climate? Bulletin of the American Meteorological Society 88, 541–550. https://doi.org/10.1175/BAMS-88-4-541

Pruppacher, Hans R., and James D. Klett, 2012. Microphysics of Clouds and Precipitation: Reprinted 1980. Springer Science & Business Media.

Qiu, S., Dong, X., Xi, B., & Li, J. L., 2015. Characterizing Arctic mixed-phase cloud structure and its relationship with humidity and temperature inversion using ARM NSA observations. Journal of Geophysical Research: Atmospheres, 120(15), 7737-7746.

Rauber, R.M., Tokay, A., 1991. An Explanation for the Existence of Supercooled Water at the Top of Cold Clouds. Journal of the Atmospheric Sciences 48, 1005–1023.

https://doi.org/10.1175/1520-0469(1991)048<1005:AEFTEO>2.0.CO;2

Saud, T., Dey, S., Das, S., Dutta, S., 2016. A satellite-based 13-year climatology of net cloud radiative forcing over the Indian monsoon region. Atmospheric Research 182, 76–86. https://doi.org/10.1016/j.atmosres.2016.07.017

Sedlar, J., Tjernström, M., Rinke, A., Orr, A., Cassano, J., Fettweis, X., Heinemann, G., Seefeldt, M., Solomon, A., Matthes, H., Phillips, T., Webster, S., 2020. Confronting Arctic Troposphere, Clouds, and Surface Energy Budget Representations in Regional Climate Models With Observations. Journal of Geophysical Research: Atmospheres 125, e2019JD031783. https://doi.org/10.1029/2019JD031783

Seiki, T., Roh, W., Satoh, M., 2022. Cloud Microphysics in Global Cloud Resolving Models. Atmosphere-Ocean 60, 477–505. https://doi.org/10.1080/07055900.2022.2075310

Seo, H., Yang, J., 2013. Dynamical response of the Arctic atmospheric boundary layer process to uncertainties in sea-ice concentration. Journal of Geophysical Research: Atmospheres 118, 12,383-12,402. https://doi.org/10.1002/2013JD020312

Seo, M., Kim, H.-C., Seong, N.-H., Sim, S., Han, K.-S., 2023. Variability of Surface Radiation Budget over Arctic during Two Recent Decades from Perspective of CERES and ERA5 Data. Remote Sensing 15, 829. https://doi.org/10.3390/rs15030829

Serreze, M.C., Barry, R.G., 2011. Processes and impacts of Arctic amplification: A research synthesis. Global and Planetary Change 77, 85–96. https://doi.org/10.1016/j.gloplacha.2011.03.004

Shafer, C.M., Mercer, A.E., Doswell, C.A., Richman, M.B., Leslie, L.M., 2009. Evaluation of WRF Forecasts of Tornadic and Nontornadic Outbreaks When Initialized with Synoptic-Scale Input. Monthly Weather Review 137, 1250–1271. https://doi.org/10.1175/2008MWR2597.1

Shaw, J., McGraw, Z., Bruno, O., Storelvmo, T., Hofer, S., 2022. Using Satellite Observations to Evaluate Model Microphysical Representation of Arctic Mixed-Phase Clouds. Geophysical Research Letters 49, e2021GL096191. https://doi.org/10.1029/2021GL096191

Shupe, M.D., Intrieri, J.M., 2004. Cloud Radiative Forcing of the Arctic Surface: The Influence of Cloud Properties, Surface Albedo, and Solar Zenith Angle. Journal of Climate 17, 616–628. https://doi.org/10.1175/1520-0442(2004)017<0616:CRFOTA>2.0.CO;2

Shupe, M.D., Matrosov, S.Y., Uttal, T., 2006. Arctic Mixed-Phase Cloud Properties Derived from Surface-Based Sensors at SHEBA. Journal of the Atmospheric Sciences 63, 697–711. https://doi.org/10.1175/JAS3659.1

Shupe, M.D., Daniel, J.S., Boer, G. de, Eloranta, E.W., Kollias, P., Long, C.N., Luke, E.P., Turner, D.D., Verlinde, J., 2008. A Focus On Mixed-Phase Clouds: The Status of Ground-Based Observational Methods. Bulletin of the American Meteorological Society 89, 1549–1562. https://doi.org/10.1175/2008BAMS2378.1

Shupe, M.D., Kollias, P., Persson, P.O.G., McFarquhar, G.M., 2008. Vertical Motions in Arctic Mixed-Phase Stratiform Clouds. Journal of the Atmospheric Sciences 65, 1304–1322. https://doi.org/10.1175/2007JAS2479.1

Shupe, M.D., 2011. Clouds at Arctic Atmospheric Observatories. Part II: Thermodynamic Phase Characteristics. Journal of Applied

Meteorology and Climatology 50, 645–661. https://doi.org/10.1175/2010JAMC2468.1

Shupe, M.D., Turner, D.D., Walden, V.P., Bennartz, R., Cadeddu, M.P., Castellani, B.B., Cox, C.J., Hudak, D.R., Kulie, M.S., Miller, N.B., Neely, R.R., Neff, W.D., Rowe, P.M., 2013. High and Dry: New Observations of Tropospheric and Cloud Properties above the Greenland Ice Sheet. Bulletin of the American Meteorological Society 94, 169–186. https://doi.org/10.1175/Bmixed-phase cloud-D-11-00249.1

Shupe, M.D., Turner, D.D., Zwink, A., Thieman, M.M., Mlawer, E.J., Shippert, T., 2015. Deriving Arctic Cloud Microphysics at Barrow, Alaska: Algorithms, Results, and Radiative Closure. Journal of Applied Meteorology and Climatology 54, 1675–1689. https://doi.org/10.1175/JAMC-D-15-0054.1

Silber, I., Verlinde, J., Eloranta, E.W., Flynn, C.J., Flynn, D.M., 2018. Polar Liquid Cloud Base Detection Algorithms for High Spectral Resolution or Micropulse Lidar Data. Journal of Geophysical Research: Atmospheres 123, 4310–4322. https://doi.org/10.1029/2017JD027840

Solomon, A., Shupe, M.D., Persson, P.O.G., Morrison, H., 2011. Moisture and dynamical interactions maintaining decoupled Arctic mixed-phase stratocumulus in the presence of a humidity inversion. Atmospheric Chemistry and Physics 11, 10127–10148. https://doi.org/10.5194/acp-11-10127-2011

Solomon, A., Shupe, M.D., Persson, O., Morrison, H., Yamaguchi, T., Caldwell, P.M., Boer, G. de, 2014. The Sensitivity of Springtime Arctic Mixed-Phase Stratocumulus Clouds to Surface-Layer and Cloud-Top Inversion-Layer Moisture Sources. Journal of the Atmospheric Sciences 71, 574–595. https://doi.org/10.1175/JAS-D-13-0179.1

Sotiropoulou, G., Vignon, É., Young, G., Morrison, H., O'Shea, S.J., Lachlan-Cope, T., Berne, A., Nenes, A., 2021. Secondary ice production in summer clouds over the Antarctic coast: an underappreciated process in atmospheric models. Atmospheric Chemistry and Physics 21, 755–771. https://doi.org/10.5194/acp-21-755-2021

Stephens, G.L., 2005. Cloud Feedbacks in the Climate System: A Critical Review. Journal of Climate 18, 237–273. https://doi.org/10.1175/JCLI-3243.1

Sun, Z., Shine, K.P., 1994. Studies of the radiative properties of ice and mixed-phase clouds. Quarterly Journal of the Royal Meteorological Society 120, 111–137. https://doi.org/10.1002/qj.49712051508

Tjernström, M., Leck, C., Birch, C.E., Bottenheim, J.W., Brooks, B.J., Brooks, I.M., Bäcklin, L., Chang, R.Y.-W., de Leeuw, G., Di Liberto, L., de la Rosa, S., Granath, E., Graus, M., Hansel, A., Heintzenberg, J., Held, A., Hind, A., Johnston, P., Knulst, J., Martin, M., Matrai, P.A., Mauritsen, T., Müller, M., Norris, S.J., Orellana, M.V., Orsini, D.A., Paatero, J., Persson, P.O.G., Gao, Q., Rauschenberg, C., Ristovski, Z., Sedlar, J., Shupe, M.D., Sierau, B., Sirevaag, A., Sjogren, S., Stetzer, O., Swietlicki, E., Szczodrak, M., Vaattovaara, P., Wahlberg, N., Westberg, M., Wheeler, C.R., 2014. The Arctic Summer Cloud Ocean Study (ASCOS): overview and experimental design. Atmospheric Chemistry and Physics 14, 2823–2869. https://doi.org/10.5194/acp-14-2823-2014

Turner, J., Colwell, S.R., Marshall, G.J., Lachlan-Cope, T.A., Carleton, A.M., Jones, P.D., Lagun, V., Reid, P.A., Iagovkina, S., 2005. Antarctic climate change during the last 50 years. International Journal of Climatology 25, 279–294. https://doi.org/10.1002/joc.1130

Twomey, S., 1974. : Pollution and the planetary albedo, Atmos. Environ., 8, 1251–1256, doi: 10.1016/0004-6981(74)90004-3, 1974.

Urrego-Blanco, J.R., Hunke, E.C., Urban, N., 2019. Emergent Relationships Among Sea Ice, Longwave Radiation, and the Beaufort High Circulation Exposed Through Parameter Uncertainty Analysis. Journal of Geophysical Research: Oceans 124, 9572–9589. https://doi.org/10.1029/2019JC014979

Vavrus, S., Waliser, D., Schweiger, A., Francis, J., 2008. Simulations of 20th and 21st century Arctic cloud amount in the global climate models assessed in the IPCC AR4. Clim Dyn 33, 1099. https://doi.org/10.1007/s00382-008-0475-6

Verlinde, J., Harrington, J.Y., McFarquhar, G.M., Yannuzzi, V.T., Avramov, A., Greenberg, S., Johnson, N., Zhang, G., Poellot, M.R., Mather, J.H., Turner, D.D., Eloranta, E.W., Zak, B.D., Prenni, A.J., Daniel, J.S., Kok, G.L., Tobin, D.C., Holz, R., Sassen, K., Spangenberg, D., Minnis, P., Tooman, T.P., Ivey, M.D., Richardson, S.J., Bahrmann, C.P., Shupe, M., DeMott, P.J., Heymsfield, A.J., Schofield, R., 2007. The Mixed-Phase Arctic Cloud Experiment. Bulletin of the American Meteorological Society 88, 205–222. https://doi.org/10.1175/BAMS-88-2-205

Vignon, É., Alexander, S.P., DeMott, P.J., Sotiropoulou, G., Gerber, F., Hill, T.C.J., Marchand, R., Nenes, A., Berne, A., 2021. Challenging and Improving the Simulation of Mid-Level Mixed-Phase Clouds Over the High-Latitude Southern Ocean. Journal of Geophysical Research: Atmospheres 126, e2020JD033490. https://doi.org/10.1029/2020JD033490

Voigt, A., Albern, N., Papavasileiou, G., 2019. The Atmospheric Pathway of the Cloud-Radiative Impact on the Circulation Response to Global Warming: Important and Uncertain. Journal of Climate 32, 3051–3067. https://doi.org/10.1175/JCLI-D-18-0810.1

Walsh, J.E., Kattsov, V.M., Chapman, W.L., Govorkova, V., Pavlova, T., 2002. Comparison of Arctic Climate Simulations by Uncoupled and Coupled Global Models. Journal of Climate 15, 1429–1446.

https://doi.org/10.1175/1520-
0442(2002)015<1429:COACSB>2.0.CO;2

Wendisch, M., Keil, A., Korolev, A.V., 1996. FSSP Characterization with Monodisperse Water Droplets. Journal of Atmospheric and Oceanic Technology 13, 1152–1165. https://doi.org/10.1175/1520-
0426(1996)013<1152:FCWMWD>2.0.CO;2

Wendisch, M., Macke, A., Ehrlich, A., Lüpkes, C., Mech, M., Chechin, D., Dethloff, K., Velasco, C.B., Bozem, H., Brückner, M., Clemen, H.-C., Crewell, S., Donth, T., Dupuy, R., Ebell, K., Egerer, U., Engelmann, R., Engler, C., Eppers, O., Gehrmann, M., Gong, X., Gottschalk, M., Gourbeyre, C., Griesche, H., Hartmann, J., Hartmann, M., Heinold, B., Herber, A., Herrmann, H., Heygster, G., Hoor, P., Jafariserajehlou, S., Jäkel, E., Järvinen, E., Jourdan, O., Kästner, U., Kecorius, S., Knudsen, E.M., Köllner, F., Kretzschmar, J., Lelli, L., Leroy, D., Maturilli, M., Mei, L., Mertes, S., Mioche, G., Neuber, R., Nicolaus, M., Nomokonova, T., Notholt, J., Palm, M., Pinxteren, M. van, Quaas, J., Richter, P., Ruiz-Donoso, E., Schäfer, M., Schmieder, K., Schnaiter, M., Schneider, J., Schwarzenböck, A., Seifert, P., Shupe, M.D., Siebert, H., Spreen, G., Stapf, J., Stratmann, F., Vogl, T., Welti, A., Wex, H., Wiedensohler, A., Zanatta, M., Zeppenfeld, S., 2019. The Arctic Cloud Puzzle: Using ACLOUD/PASCAL Multiplatform Observations to Unravel the Role of Clouds and Aerosol Particles in Arctic Amplification. Bulletin of the American Meteorological Society 100, 841–871. https://doi.org/10.1175/Bmixed-phase cloud-D-18-0072.1

Wesslén, C., Tjernström, M., Bromwich, D.H., de Boer, G., Ekman, A.M.L., Bai, L.-S., Wang, S.-H., 2014. The Arctic summer atmosphere: an evaluation of reanalyses using ASCOS data. Atmospheric Chemistry and Physics 14, 2605–2624. https://doi.org/10.5194/acp-14-2605-2014

Wilson, A.B., Bromwich, D.H., Hines, K.M., 2011. Evaluation of Polar WRF forecasts on the Arctic System Reanalysis domain: Surface and upper air analysis. Journal of Geophysical Research: Atmospheres 116. https://doi.org/10.1029/2010JD015013

Wilson, A.B., Bromwich, D.H., Hines, K.M., 2012. Evaluation of Polar WRF forecasts on the Arctic System Reanalysis Domain: 2. Atmospheric hydrologic cycle. Journal of Geophysical Research: Atmospheres 117. https://doi.org/10.1029/2011JD016765

WMO/WWRP, W.M.O.: W.M.O.W.R.P., 2012. Recommended methods for evaluating cloud and related parameters World Weather Research Programme (WWRP)/Working Group on Numerical Experimentation (WGNE) Joint Working Group on Forecast Verification Research (JWGFVR).

Wyser, K., Jones, C.G., Du, P., Girard, E., Willén, U., Cassano, J., Christensen, J.H., Curry, J.A., Dethloff, K., Haugen, J.-E., Jacob, D., Køltzow, M., Laprise, R., Lynch, A., Pfeifer, S., Rinke, A., Serreze, M., Shaw, M.J., Tjernström, M., Zagar, M., 2008. An evaluation of Arctic cloud and radiation processes during the SHEBA year: simulation results from eight Arctic regional climate models. Clim Dyn 30, 203–223. https://doi.org/10.1007/s00382-007-0286-1

Xie, S., Liu, X., Zhao, C., Zhang, Y., 2013. Sensitivity of CAM5-Simulated Arctic Clouds and Radiation to Ice Nucleation Parameterization. Journal of Climate 26, 5981–5999. https://doi.org/10.1175/JCLI-D-12-00517.1

Yang, C.A., Diao, M., Gettelman, A., Zhang, K., Sun, J., McFarquhar, G., Wu, W., 2021. Ice and Supercooled Liquid Water Distributions Over the Southern Ocean Based on In Situ Observations and Climate Model Simulations. Journal of Geophysical Research: Atmospheres 126, e2021JD036045. https://doi.org/10.1029/2021JD036045

Yeo, H., Kim, M.-H., Son, S.-W., Jeong, J.-H., Yoon, J.-H., Kim, B.-M., Kim, S.-W., 2022. Arctic cloud properties and associated radiative effects in the three newer reanalysis datasets (ERA5, MERRA-2, JRA-55): Discrepancies and possible causes. Atmospheric Research 270, 106080. https://doi.org/10.1016/j.atmosres.2022.106080

Yoshida, Y., Asano, S., 2005. Effects of the Vertical Profiles of Cloud Droplets and Ice Particles on the Visible and Near-Infrared Radiative Properties of Mixed-Phase Stratocumulus Clouds. 気象集誌. 第 2 輯 83, 471–480. https://doi.org/10.2151/jmsj.83.471

Zhang, M., Xie, S., Liu, X., Lin, W., Zhang, K., Ma, H.-Y., Zheng, X., Zhang, Y., 2020. Toward Understanding the Simulated Phase Partitioning of Arctic Single layer Mixed-Phase Clouds in E3SM. Earth and Space Science 7, e2020EA001125. https://doi.org/10.1029/2020EA001125

Zhou, L., Harris, L., Chen, J.-H., Gao, K., Guo, H., Xiang, B., Tong, M., Huff, J.J., Morin, M., 2022. Improving Global Weather Prediction in GFDL SHiELD Through an Upgraded GFDL Cloud Microphysics Scheme. Journal of Advances in Modeling Earth Systems 14, e2021MS002971. https://doi.org/10.1029/2021MS002971

Zuidema, P., Baker, B., Han, Y., Intrieri, J., Key, J., Lawson, P., Matrosov, S., Shupe, M., Stone, R., Uttal, T., 2005. An Arctic Springtime Mixed-Phase Cloudy Boundary Layer Observed during SHEBA. Journal of the Atmospheric Sciences 62, 160–176. https://doi.org/10.1175/JAS-3368.1

국문 초록

북극 증폭에 대한 구름의 영향은 구름의 특성뿐만 아니라 구름이 북극 기후의 구성 요소(수증기, 해양, 해빙, 알베도, 표면 온도 등)와 밀접하게 관련되어 있기 때문에 불확실하다. 이 논문에서는 북극에서 구름의 역할을 더 잘 이해하기 위해 Cloudnet의 스발바드 니알슨 지상 관측 자료를 바탕으로 구름의 거시적 및 미시적 특성을 분석하였다. 2017년 2월부터 2023년 2월까지 구름의 총 발생률은 약 77.6%로 나타났다. 가장 우세한 구름 유형은 다층 구름으로 발생 빈도는 39.1%, 단층 구름은 ~37.2%이다. 단층 얼음, 액체, 혼합상 구름의 총 발생 빈도는 각각 19%, 4.4%, 14.9%이다. 또한, 니알슨 관측소의 Baseline Surface Radiation Network (BSRN) 복사 자료를 활용하여 상하 단파 및 장파 복사에 대한 측정값을 분석하였다. 얼음과 혼합상 구름에 대한 장파 상향 및 장파 하향 플럭스의 상대적으로 낮은 값은 위상별 구름 최고 온도와 높은 상관관계를 보였다.

본 연구를 통해 얻은 구름 특성 데이터베이스와 분류 방법은 기상 예측 모델 평가에 사용되었다. 극지에 최적화된 Polar-optimized Weather Research and Forecasting (PWRF) 모델에 구현된 4가지 구름 미세물리 매개변수화 방식(Morrison, WDM6, NSSL, P3)을 활용하여 시뮬레이션한 저층 북극 혼합 구름의 미시물리적 특성을 평가하였다.

이 분석은 2017년 5월부터 6월까지 스발바드 인근에서 진행된 Arctic Cloud Observations Using Airborne Measurements during the Polar Day (ACLOUD) 캠페인 데이터와의 비교를 기반으로 한다. 이 캠페인 기간 동안 상당수의 혼합 구름이 관측되었는데, 이는 주로 해빙과 해양 전이대를 통과하는 동안 기단이 가열(4° C)되는 단열 운동과 현열/잠열 플럭스로 인해 발생했다. Morrison 및 WDM6 구름 모수화 방식은 구름 발생 예측에서 높은 로그 확률(0.50, 0.48)과 함께 1에 가까운 빈도 편향 값(1.07, 1.13)을 나타내며 구름이 발생한 지역 및 높이와 잘 일치하는 것으로 나타나 전반적으로 가장 우수한 성능을 나타냈다. NSSL 와 P3 모수화 스킴은 낮은 로그 확률 비율(0.17, 0.16)과 함께 높은 빈도 편향 값(1.30, 1.56)을 보여 구름 발생을 과대평가하는 것으로 나타났다. 반대로 WDM6 모수화 스킴은 Morrison 및 NSSL 방식에 비해 더 높은 얼음 혼합 비율을 생성한 반면, 후자의 두 방식은 더 많은 눈과 싸락눈을 생성하는 경향이 있었다.

모든 방식은 일반적으로 액체와 얼음 수분의 함량을 모두 과소평가했다. 뿐만 아니라, 혼합 구름의 복사율 분석을 통해 구름 타입에 따른 장파와 단파의 상대적 중요도를 평가하고, 구름의 미세물리적 특성에 대한 의존성을 분석하였다. 장파 하강 복사율은 대기 온도와 습도에 따라 달라지며, 모델에서 과소평가된 장파 하강 복사율은 각 구름 모수화 스킴에서 모의된 구름 수분 함량 편향과 높은 상관관계를 보였다. 이 연구는 급격한 북극 온난화 조건에서 구름이 북극 기후에 미치는 영향을 보

다 정확하게 추정하기 위해 북극 구름의 타입구분이 중요하며, 북극의 구름 매개 변수화에 대한 관측 기반 개발이 시급히 필요하다.

주요어: 북극 구름, 혼합 구름, ACLOUD 캠페인, Cloudnet, PWRF, 미세 물리 모수화 스킴

학번: 2015-30984